The influence of asymmetric line profiles on the reliability of the search for varying fundamental constants

Dissertation zur Erlangung des Doktorgrades
an der Fakultät für Mathematik, Informatik und Naturwissenschaften
Fachbereich Physik

der Universität Hamburg

vorgelegt von Nils Prause

Hamburg, 2014

Veröffentlichungen:
Prause, N., Reimers, D., Fechner, C., & Janknecht,
E. 2007, A&A, 470, 67
Prause, N., & Reimers, D. 2013, A&A 431, 1167

Gutachter der Dissertation:
Prof. Dr. Dieter Reimers
Prof. Dr. Lutz Wisotzki

Gutachter der Disputation:
Prof. Dr. Peter Hauschildt
Prof. Dr. Robi Banerjee

Termin der Disputation:
17.09.2014

Zusammenfassung

Optische Quasarspektren können benutzt werden um Variationen der Feinstrukturkonstanten α zu bestimmen. In den letzten Jahren wurden in diesem Bereich widersprüchliche Ergebnisse veröffentlicht, die eine Unterschätzung systematischer Fehlerquellen nahelegen. Neben Problemen mit der Wellenlängenkalibration können auch Fehler durch eine ungenaue Dekomposition der Absorptionssysteme entstehen. Das Ziel dieser Arbeit ist es, den Einfluss von fehlerhafter Dekomposition aufgrund asymmetrischer Linienprofile auf die Präzision von Positionsfits abzuschätzen. Methoden werden entwickelt um zwischen Ursachen für Positionsverschiebungen zwischen Absorptionslinien von verschiedenen Übergangen zu unterscheiden und damit systematische Fehler in kommenden Analysen zu minimieren.

Asymmetrische Linienprofile wurden mit zwei verschiedenen Methoden simuliert. Einmal wurden die Profile als unaufgelöster blend von schmalen Linien erstellt. Darüber hinaus wurde ein makroskopisches Geschwindigkeitsfeld des absorbierenden Mediums simuliert. Die entsprechenden Spektren wurden mit gängigen Methoden gefittet um nach scheinbaren Verschiebungen von Absorptionslinien zu suchen, die eine Variation von Naturkonstanten vortäuschen könnten. Unterschiede zwischen Positionsverschiebungen durch eine fehlerhafte Dekomposition und α Variation wurden untersucht. Dafür wurden neue Methoden entwickelt oder aus anderen Bereichen für diese Analyse übernommen. Darüber hinaus wurde die Verformung von Linienprofilen durch sich ändernde Isotopenverhältnisse simuliert und die Möglichkeiten diese zu messen untersucht. Die Resultate wurden dann auf echte Daten angewandt.

Scheinbare relative Positionsverschiebungen von einigen hundert Metern pro Sekunde wurden in simulierten Spektren mit asymmetrischen Linienprofilen gemessen. Um die Resultate der simulierten Spektren mit echten Daten zu vergelichen wurden 17 Fe II Systeme in acht Quasarspektren analysiert. Mit den hier entwickelten Methoden wurden mehrere Systeme entdeckt in denen Positionsverschiebungen zwischen unterschiedlichen Fe II Übergängen durch fehlerhafte Dekomposition erzeugt wurden. Mit den übrigen Systemen wurde keine relevante Variation der Feinstrukturkonstante gemessen. Wir folgern dass fehlerhafte Dekompositionen von Absorptionslinien zum Teil für die widersprüchlichen Resultate verantwortlich sein können, die bisher veröffentlicht wurden.

Abstract

Optical quasar spectra can be used to trace variations of the fine-structure constant α. Controversial results that have been published in last years suggest a presence of systematical error sources. In addition to wavelength calibration problems, errors might arise because of deficient line decompositions. The aim of this work is to estimate the influence of incorrect line decompositions in fitting procedures due to asymmetric line profiles on the precision of line position fits. Methods are developed to distinguish between different sources of position shifts between absorption lines of different transitions and thus to minimise systematical errors in future analyses.

To simulate asymmetric line profiles, two different methods were used. On the one hand the profiles were created as an unresolved blend of narrow lines and on the other hand a macroscopic velocity field of the absorbing medium was simulated. The simulated spectra were analysed with standard methods to search for apparent shifts of line positions that would mimic a variation of fundamental constants. Differences between position shifts due to an incorrect line decomposition and a real variation of constants were probed using methods that have been newly developed or adapted for this kind of analysis. Furthermore the distortion of line shapes by changing isotope abundances was simulated and the possibility to measure theses in real data was studied. The results were then applied to real data.

Apparent relative velocity shifts of several hundred metres per second were found in the analysis of simulated spectra with asymmetric line profiles. To compare the results of from simulated spectra with real data, a set of 17 Fe II systems in eight quasar spectra was analysed. With the methods that were developed in this work several systems were identified that show position shifts between different Fe II transitions that were created by incorrect line decomposition. Using only the remaining systems, no variation of the fine-structure constant α was found within the error limits. We thus conclude that incorrect line decompositions can be partly responsible for the conflicting results published so far.

Contents

Chapter 1

Introduction

Unification theories with extra dimensions (e.g. string theories) inspire a search for varying fundamental constants. As dimensionless constants, in addition to the proton to electron mass ratio $\mu = m_\mathrm{P}/m_\mathrm{e}$, the fine-structure constant $\alpha = e^2/(\hbar c)$ is of special interest for this research field. A wide range of complementary methods have been used to study a possible variability of α, based in most cases upon an analysis of atomic or molecular spectra or a measurement of element abundances. High precision laboratory experiments are able to constrain a variation of α to $\frac{\delta \ln \alpha}{\delta t} < 10^{-17}\,\mathrm{yr}^{-1}$ at $z = 0$ (Rosenband et al. 2008; Leefer et al. 2013). Analyses of geological samples can constrain α to $|\Delta\alpha/\alpha| < 10^{-7}$ at $z = 0.14$ (Olive et al. 2002; Petrov et al. 2006; Gould et al. 2006). Measurements of primordial element abundances and an analysis of the CMB power spectrum allow a constraint of $|\Delta\alpha/\alpha| < 10^{-2}$ in the early universe (Cyburt et al. 2005; Landau & Scóccola 2010; O'Bryan et al. 2013). The intermediate range up to $z \sim 4$ ($\sim 90\%$ of the age of the universe) can be traced by quasar absorption line spectra. Assuming a linear variation with time, the methods are competitive in accuracy.

The analysis of optical quasar spectra at high redshifts is the only method where indications of a time variation of the fine-structure constant have been reported repeatedly in the literature. These results were, at least in part, conflicting, ranging from $\Delta\alpha/\alpha = (-5.4 \pm 1.2) \cdot 10^{-6}$ (Murphy et al. 2003), over $\Delta\alpha/\alpha = (-0.4 \pm 3.3) \cdot 10^{-6}$(Quast et al. 2004), up to $\Delta\alpha/\alpha = (5.4 \pm 2.5) \cdot 10^{-6}$ (Levshakov et al. 2007). The reasons for these discrepancies are not yet fully understood. In addition to wavelength calibration difficulties (Griest et al. 2010), problems with methodology might be the cause. One of the problems is insufficient spectral resolution in present quasar spectra. It is known from very high resolution spectra ($R = 10^6 \mathrel{\hat{=}} 0.3\,\mathrm{km\,s^{-1}}$) of galactic interstellar Na I and Ca II absorption lines that the typical separation of subcomponents of interstellar lines is about $1.2\,\mathrm{km\,s^{-1}}$ so that even at a very high resolutions, only a fraction of the individual subcomponents are detected (Welty et al. 1994, 1996; Welty 1998). This means that even in the highest quality quasar spectra ($R \approx 80\,000 \mathrel{\hat{=}} 4\,\mathrm{km\,s^{-1}}$), apparently single Doppler profiles may have many narrow, even saturated subcomponents that can be distinguished only by line asymmetries. Murphy et al. (2001b) have simulated the influence of blends with single unidentified lines. Since they were mainly interested in effects that are statistically relevant for a high number of systems, they focussed on possible weak transitions that lie close to those used in their analysis. Chand et al. (2004) have probed the possibility of apparent position shifts due to unresolved line blends by simulating systems consisting of two closely blended components. They found that in these cases significant problems can arise for this kind of analysis and they restricted their work to systems with simple profiles.

Small-scale velocity splittings become particularly important for quasar absorption systems formed in galactic discs. Even if more systems are formed in halos because of their larger cross sections, as argued by Murphy et al. (2003), each individual absorption system has to be examined to detect possible sources of line position shifts that could mimic an α variation. As long as lines of the same ion with similar transition strength $f\lambda_0$ are compared (e.g. the Fe II transition at 1608 Å (hereafter: Fe II 1608) with Fe II 2374), the influence of

this error source on α variation measurements is expected to be small. However, this was rarely the case in existing studies.

In this work, possible apparent line position shifts that could be mimicked when using absorption lines with asymmetric profiles are discussed. While in previous works simulations have been done for simple blends of two components (Murphy et al. 2001b; Chand et al. 2004), in this work the line profiles are assumed to be more complex and are therefore a better representation of real data. Simulated quasar spectra were created to determine the influence of asymmetric line shapes on the results of the methods used to trace variations of the fine-structure constant α (chap. 3). Furthermore the possibility to measure isotope abundances by analysing the shapes of absorption lines is discussed. The methods developed in the simulations are then applied to real data taken with the UVES spectrograph at the VLT (Dekker et al. 2000) (chap. 4). In chap. 5 the results are discussed. Though this work concentrates on methods to detect possible variations of the fine-structure constant α, most of the findings are also relevant for related tasks. Sections 3.1, 3.4.1, 3.4.2, 3.4.4, 3.4.5, 4.2, and parts of chaps. 1 and 5 have previously been published in Prause & Reimers (2013).

Chapter 2

Background

2.1 Motivation - Extra dimensional theories

The possibility for fundamental constants to vary is inherent in all theories that use extra dimensions, as is the case for all major theories that try to unify gravity with the other forces. The first recognised approach into this direction was made by Kaluza (1921). He discovered that it is possible to describe Einstein's equations of gravity and the Maxwell equations with a single model if a fourth space dimension is introduced. Klein (1926) extended this model by proposing the fifth dimension to be a circle with a small radius R (compactification). The limit of a very small radius $R \to 0$ approximates our observed four dimensional space-time.

The idea got greater attention with the introduction of string theory, which is a quantum field theory in two dimensions with certain constraints, given by the geometry of the strings. First introduced as a possibility to explain scattering amplitudes of pions (Veneziano 1968; Nambu 1970), it soon turned out to be a good candidate for a unified theory of forces (Scherk & Schwarz 1974). A string theory without unphysical solutions is only possible in a space-time with at least ten dimensions. Such a ten dimensional string theory is invariant under a supersymmetric transformation (Green & Schwarz 1981).

The standard model of particle physics knows 22 fundamental constants, i.e. constants whose value cannot be derived from fundamental principles (see e.g. Uzan 2011). The idea in theories with extra dimensions is that the values that are measured for these constants are just projections of a more fundamental value into our four dimensional space-time. When the radii of the compact dimensions change with time, so will the projected value of constants (Weinberg 1983; Marciano 1984). Measuring a variation of constants in experiment or observation would be a strong support for multi dimensional theories.

2.2 The fine-structure constant and quasar spectra

A change of the fine-structure-constant α would affect energy levels and thus transition frequencies in ions and atoms. In quasar spectra this can be observed as wavelength shifts of absorption lines. Relativistic corrections of electronic transitions, which contribute to the fine structure splitting, scale with α^2 and have different sensitivities, depending on the electron configuration. A comparison of line positions of transitions from the ground state to different fine structure levels thus allows to constrain or measure a possible variation of α.

The measured transition frequencies can be written as

$$\omega = \omega_0 + q_1 \left((\alpha/\alpha_0)^2 - 1\right) + q_2 \left((\alpha/\alpha_0)^4 - 1\right), \quad (2.1)$$

where ω_0 is the laboratory frequency, α and α_0 the fine-structure constant in the observed systems and in the laboratory, respectively, and q_1 and q_2 are sensitivity coefficients (Dzuba et al. 1999). Since the α variation is expected to be small ($\Delta\alpha/\alpha \ll 1$), the frequency shift is mainly dominated by q_1. In a linear approximation this can be rewritten in terms of the measured redshift z.

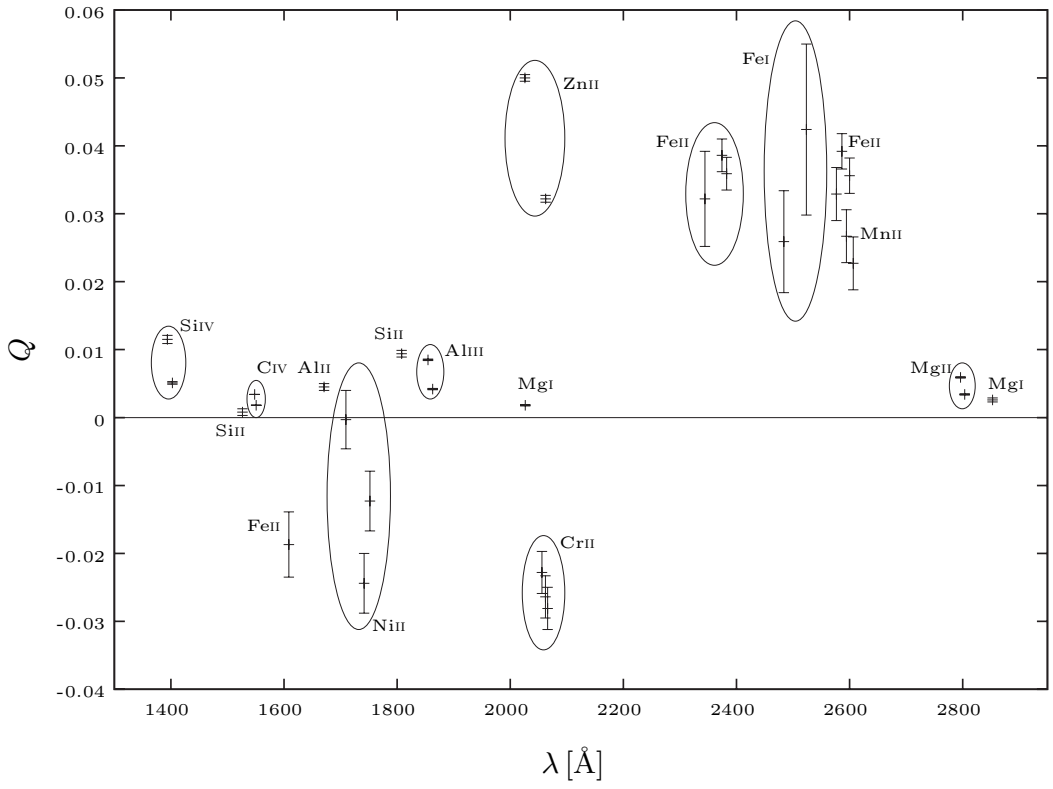

Figure 2.1: Dimensionless sensitivity coefficients and laboratory wavelengths of ions that are typically abundant in quasar absorption spectra (See Table 2.1).

$$z = z_0 + \kappa_\alpha \, Q, \tag{2.2}$$

with the slope parameter

$$\kappa_\alpha = -2\,(1 + z_0)\frac{\Delta\alpha}{\alpha}. \tag{2.3}$$

$Q = q/\omega_0$ is the dimensionless sensitivity coefficient (Levshakov 2004). Figure 2.1 shows the sensitivity coefficients for ions which are abundant in quasar spectra. Transitions with low sensitivities as in Mg II and Si II can be used as anchor lines for a comparison with high sensitivity transitions, assuming that the lines originate from the same gas phase. Heavier ions like Fe II, Ni II or Zn II have high sensitivities. Fe II has transitions with positive and negative sensitivities and is quite abundant in quasar spectra.

When several transitions with different sensitivities are present, the slope parameter κ_α, and thus the α variation, can be found with a regression analysis of Eq. 2.2. In many cases the fitted line positions are not compatible with the regression model. It is thus important to investigate all effects that can cause shifts in line positions.

Table 2.1 shows the laboratory wavelength λ_0, oscillator strengths f, and sensitivity coefficients Q used in this work. The factor $f\lambda_0$ is a measure of the strength of the transition (see Eq. 3.3).

Fe II 1608 is opposite in sensitivity to the other Fe II transitions; therefore, it constitutes an ideal candidate for the search for a varying fine-structure constant α by comparing only other Fe II lines with Fe II 1608. While this method has the disadvantage that there are basically just two different sensitivities available, $Q \approx -0.02$ for Fe II 1608 and $Q \approx 0.03 - 0.04$ for the other Fe II transitions, the

,
Table 2.1: Laboratory wavelength λ_0, oscillator strength f, transition strength $f\lambda_0$, and sensitivity coefficients Q for abundant metal lines in quasar spectra

Transition	λ_0 [Å]	f [3]	$f\lambda_0$ [Å]	Q
C IV 1548	1548.2040[3]	0.1897	293.8	0.003[4]
C IV 1551	1550.7810[3]	0.0947	146.9	0.002[4]
Mg I 2026	2026.4768[2]	0.1130	229.1	0.002[4]
Mg I 2853	2852.9631[2]	1.8311	5224.0	0.003[4]
Mg II 2796	2796.3540[2]	0.615	1719.8	0.006[4]
Mg II 2804	2803.5311[2]	0.306	857.9	0.003[4]
Al II 1671	1670.7886[3]	1.7381	2904.0	0.005[4]
Al III 1855	1854.7184[3]	0.5594	1037.5	0.008[4]
Al III 1863	1862.7910[3]	0.2779	517.6	0.004[4]
Si II 1527	1526.7070[3]	0.1328	202.8	0.001[6]
Si II 1808	1808.0129[3]	0.0021	3.8	0.009[6]
Cr II 2056	2056.2569[3]	0.1030	211.8	-0.023[6]
Cr II 2062	2062.2361[3]	0.0758	156.3	-0.026[6]
Mn II 2577	2576.8770[3]	0.3613	931.1	0.033[7]
Mn II 2594	2594.4990[3]	0.2792	724.4	0.027[7]
Mn II 2606	2606.4620[3]	0.1977	515.2	0.023[7]
Fe I 2484	2484.0209[3]	0.5443	1352.1	0.026[8]
Fe I 2524	2523.6083[3]	0.2032	512.8	0.042[8]
Fe II 1608	1608.4508[1]	0.0577	92.8	-0.019*
Fe II 2344	2344.2127[1]	0.114	267.2	0.032*
Fe II 2374	2374.4601[1]	0.0313	74.3	0.039*
Fe II 2383	2382.7639[1]	0.320	762.5	0.036*
Fe II 2587	2586.6493[1]	0.0691	178.7	0.039*
Fe II 2600	2600.1722[1]	0.239	621.4	0.036*
Ni II 1710	1709.6042[3]	0.0324	55.3	-0.003[6]
Ni II 1742	1741.5531[3]	0.0427	74.3	-0.024[6]
Ni II 1752	1751.9157[3]	0.0277	48.5	-0.012[6]
Zn II 2026	2026.1370[3]	0.5016	1016.2	0.050[4]
Zn II 2063	2062.6604[3]	0.2462	508.2	0.032[4]

[1] Nave & Sansonetti (2011)
[2] Aldenius (2009)
[3] Morton (2003)
[4] Savukov & Dzuba (2008)
[5] Berengut et al. (2005)
[6] Dzuba et al. (2002)
[7] Berengut et al. (2004)
[8] Dzuba & Flambaum (2008)
* Average of independent calculations by Dzuba et al. (2002) and Porsev et al. (2007)

observed line positions of transitions with comparable sensitivities provide a test on the accuracy of the wavelength calibration. When the positions of transitions with similar sensitivities are not coherent, the reasons for the discrepancies have to be investigated. In our simulations the only source for line position shifts are assumed to be unresolved blends or a velocity substructure. These are small when comparing transitions with similar strength, e.g. Fe II 1608 and Fe II 2374. In this case the parameter κ_α (Eq. 2.3) is simply the slope of a line through two points. Because these transitions have a low strength, the statistical error of position fits will be higher than for the stronger transitions. In the following analysis the α variation calculations were done using a full regression analysis as well as a simple comparison of Fe II 1608 to the transition that differs least in strength to quantify the difference of these methods.

The uncertainty of the sensitivity coefficient calculations is about 20% for Fe II 1608 and Fe II 2344 and about 10% for the other Fe II transitions (see references in Table 2.1). This leads to an uncertainty of the $\Delta\alpha/\alpha$ calculations of 20%-25%. Uncertainties of the line position measurements are dominant because they give a total and not just a relative error. The precision of the laboratory wavelength measurements is very high. When the values given in the literature are correct, they would contribute with $\sigma_{\Delta\alpha/\alpha} = 0.4 \cdot 10^{-6}$. This is about an order of magnitude lower than the precision of the most accurate α variation measurements with this method that have been reported in the literature (see sect. 2.3.2).

2.3 History of the search for a varying fine-structure constant

The idea of varying fundamental constants was first formulated by Dirac (1937) as part of his "Large Number Hypothesis". He specifically conjectured that the gravitational constant G could change with the evolution of the universe as $G \sim t^{-1}$. Already Kothari (1938) proposed to measure a variation of constants in astrophysical observations. In most cases the search for varying constants was limited to dimensionless constants like the proton-to-electron mass ratio μ or the fine-structure constant α. A change in fundamental constants would also change the value of units and in many cases an independent method to gauge the units would be necessary. This procedure would introduce at least an additional error source.

2.3.1 Fine-structure constant variation in other research fields

Nucleosynthesis

A comparison of observed primordial element abundances with theoretical nucleosynthesis calculations allows a constraint of the value of the fine-structure constant α during the first minutes of the universe. The abundances of all primordial elements depend mainly on the freeze-out temperature T_f, which on its part depends on the Fermi constant G_F, the gravitational constant G, the proton to neutron mass difference Δ_m and over the binding energies B_A on the coupling constants α_EM, α_W, α_S, α_G and the mass of the quarks (Reeves 1994).

Kolb et al. (1986) were the first to set constraints on variations of fundamental constants by studying element abundances. They found that the primordial ^{4}He abundance is primarily dependent on the proton to neutron mass difference Δ_m. Dividing Δ_m into an electromagnetic component $\Delta_{\mathrm{m}/\alpha}$ and all other contributions $\Delta_{\mathrm{m/r}}$, they deduced that under the assumption that everything else stays constant a change in α is limited to

$$|\Delta\alpha/\alpha| < 10^{-2}.$$

Similar results were reported by Bergström et al. (1999); Nollett & Lopez (2002); Cyburt et al. (2005).

A more stringent constraint is only possible when interdependence between the variation of different constants is considered. To do this a particular theoretical model has to be used. Depending on the model, a constraint of up to

$$|\Delta\alpha/\alpha| \lesssim 10^{-4}$$

can be achieved (Ichikawa & Kawasaki 2002; Coc et al. 2007).

Because of the dependence of the primordial element abundances on all coupling constants, it is either necessary to assume the other constants to be fixed or to apply a theoretical model for their interdependence. It is, in conclusion, not possible to get model independent estimation with this approach. It is, however, the only known possibility to constrain the fine-structure constant during the first moments of the universe.

A similar approach was made by Ekström et al. (2010). They calculated the influence a variation of fundamental constants would have on the nucleosynthesis in Pop III stars and the effects on stellar evolution. By coupling the fine-structure constant to other fundamental constants, using a model inspired by grand unification theories, they constrained α to

$$|\Delta\alpha/\alpha| < 10^{-5}$$

at $z \sim 15 - 20$.

Cosmic Microwave Background

Kaplinghat et al. (1999) were the first to calculate the influence a change of α would have on the CMB power spectrum. They found that mainly the redshift of recombination varies due to the changed binding energy in hydrogen. They predicted that with upcoming WMAP (Bennett et al. 1997) and PLANCK (Tauber et al. 2010) experiments a constraint of

$$|\Delta\alpha/\alpha| \sim 10^{-2} - 10^{-3}$$

should be possible. In the first results, based on data from the balloon missions BOOMERANG (Lange et al. 1995) and MAXIMA (Lee et al. 1999) it was reported that a 10% smaller value of α would be preferred by the data (Avelino et al. 2000; Battye et al. 2001). The method is, however, strongly dependent on priors for the values of cosmological parameters like the Hubble constant H_0 and the baryon density Ω_b. Including data from the COBE mission (Mather 1993) a restriction of

$$|\Delta\alpha/\alpha| \lesssim 10^{-1}$$

was reported (Avelino et al. 2001; Landau et al. 2001).

With the launch of the WMAP satellite in June 2001 an increase in precision of the α variation measurements by a factor of ten was possible (Martins et al. 2004; Ichikawa et al. 2006; Scóccola et al. 2008; Landau & Scóccola 2010). The first results from the PLANCK mission did not increase the bound on α (O'Bryan et al. 2013).

Though the power spectrum of the CMB can be used to set a constraint on a variation of the fine-structure constant, it is also sensitive to many other

parameters like the baryon density Ω_b and the Hubble constant H_0. As long as there are no stronger bounds to these, a more precise estimate of α will not be possible.

Geological methods

The Oklo natural reactor was a natural fission reactor, active about $1.8{\cdot}10^9$ years ago ($z \approx 0.14$) at the present-day Oklo uranium mine in Gabon. To gain information about the reaction processes, the ratio of two samarium isotopes $^{149}\mathrm{Sm}/^{147}\mathrm{Sm} \approx 0.02$ at the reaction site is compared to the natural ratio $^{149}\mathrm{Sm}/^{147}\mathrm{Sm} \approx 0.9$. The depletion of ^{149}Sm is dependent on the neutron capture rate which is dominated by a resonance energy E_r due to a near cancellation of the electromagnetic and nuclear forces. A variation of the fine-structure constant α would change the resonance energy, and thus the neutron capture rate. The constraint reached with this method is about

$$|\Delta\alpha/\alpha| < 10^{-7} - 10^{-8}$$

(Shlyakhter 1976; Damour & Dyson 1996; Fujii et al. 2000; Olive et al. 2002; Petrov et al. 2006; Gould et al. 2006).

Assuming a model for interdependence of various constants allow to constrain α to

$$|\Delta\alpha/\alpha| < 10^{-9} - 10^{-10}$$

(Olive et al. 2002).

Though the properties of the Oklo reactor allow a strong bound on an α variation, the system has the disadvantage that it is unique and thus prone to systematical errors. Independent geological methods use α and β decay rates and spontaneous fission reactions by measuring abundances of long lived isotopes A time scale covering the age of the solar system can be traced with this method ($z \approx 0.43$).

The first result was published by Wilkinson (1958), who compared different dating methods and abundances of ^{238}U, ^{235}U, and ^{232}Th. They were able to constrain α to

$$|\Delta\alpha/\alpha| < 8 \cdot 10^{-3}$$

.

In later studies, including abundance data of ^{187}Re, ^{187}Os, ^{206}Pb, ^{207}Pb, and ^{147}Sm from geological samples and meteorite data, the constraint could be increased to

$$|\Delta\alpha/\alpha| < 10^{-4} - 10^{-5}$$

(Dyson 1967; Gold 1968; Dyson 1972; Lindner et al. 1986; Olive et al. 2002)

It is possible to further push the limit to

$$|\Delta\alpha/\alpha| < 10^{-7}$$

by assuming a theoretical model of interdependence of constants (Olive et al. 2002; Olive et al. 2004).

Laboratory experiments

In laboratory experiments a variation of fundamental constants can be traced by comparing transition frequencies in atomic or nuclear spectra. The first approach was made by Turneaure & Stein (1976) by comparing a ^{133}Cs atomic clock with microwave cavities oscillators. Both instruments depend on fundamental constants, the clock frequency on a hyperfine transition ($\sim g_\mathrm{p}\mu\alpha^2$, with the proton g-factor g_p) and the cavity on the Bohr radius of the atom ($\sim \alpha^{-1}$). so that a combination of $g_\mathrm{p}\mu\alpha^3$ could be traced. They got an upper limit of

$$\frac{d}{dt}\ln(g_\mathrm{p}\mu\alpha^3) < 4 \cdot 10^{-12}\,\mathrm{yr}^{-1}.$$

.

In the last years several experiments were done in which hyperfine transitions of different atoms were compared to ^{133}Cs, including atomic hydrogen, ^{87}Rb, ^{87}Sr, $^{171}\mathrm{Yb}^+$, and $^{199}\mathrm{Hg}^+$. These experiments allowed a constraint of

$$\left|\frac{\nu}{\nu_\mathrm{Cs}}\right| \lesssim 10^{-16},$$

where ν and ν_Cs are the transition frequencies of the test atom and of the ^{133}Cs standard, respectively. These frequency ratios depend on a variety of different constants. An independent α variation test was not possible (Sortais et al. 2001; Bize et al. 2003; Marion et al. 2003; Fischer et al. 2004; Peik et al. 2004; Bize et al. 2005; Peik et al. 2006; Blatt et al. 2008).

A comparison of the $^1S_0 - ^3P_0$ transition of $^{27}\mathrm{Al}^+$ to the $^2S_{1/2} - ^2D_{5/2}$ transition of $^{199}\mathrm{Hg}^+$ allows a direct constraint on the variation of α. Rosenband et al. (2008) reported an accurate measurement of

$$\Delta\alpha/\alpha = (-1.6 \pm 2.3) \cdot 10^{-17}\,\mathrm{yr}^{-1}$$

after one year of data acquisition.

Dzuba et al. (2003) pointed out that the electronic dipole transition between two opposite parity states in Dy would allow a completely model independent α variation measurement. Nguyen et al. (2004) predicted that an accuracy of $\sim 10^{-18}$ should be possible with this method. After two years of taking data Leefer et al. (2013) reported a precision of

$$\Delta\alpha/\alpha = (-5.8 \pm 6.9) \cdot 10^{-17}\,\mathrm{yr}^{-1},$$

on a 1σ confidence level using ^{162}Dy and ^{164}Dy independently.

Though the precision of laboratory measurements is matchless, many of the early results were strongly parameter dependent. To get a constraint on the fine-structure constant, it was necessary to assume other constants to be stable. An approach to avoid this necessity was to compare results from different clocks at different laboratories to benefit from different sensitivities of different constants in each experiment and thus get a model independent estimate. The difficulty with this approach is that different laboratories work under different conditions, increasing the danger of unforeseen systematics.

Just the recent works, using radio frequencies of ^{162}Dy and ^{163}Dy or optical transitions in $^{27}Al^{+}$ and $^{199}Hg^{+}$ are able to get a really parameter independent constraint on a variation of α. Recently Dzuba et al. (2012) proposed to use highly charged ions like Nd^{13+} and Sm^{15+}. They predict that an accuracy of $\Delta\alpha/\alpha \sim 10^{-20}\,\mathrm{yr}^{-1}$ should be possible with this method.

2.3.2 Quasar absorption line spectroscopy

Radio and far infrared spectra

By comparing line positions of the H I 21 cm transition in radio spectra and electronic hyper-fine transitions of heavier ions in optical or UV spectra it is possible to constrain the value $x := \alpha^2 g_p/\mu$. The first approaches to this method were already able to set a constraint of the order $\sim 10^{-2} - 10^{-4}$ (Savedoff 1956; Wolfe et al. 1976; Wolfe 1980).

An increase of accuracy was possible with modern high resolution spectroscopy. Comparing positions of the H I 21 cm line with C I fine structure transitions, Cowie & Songaila (1995) got

$$\Delta x/x = (1.1 \pm 0.7) \cdot 10^{-5}$$

at $z = 1.8$.

Tzanavaris et al. (2007) used nine systems in the lines of sight of nine quasars to compare the positions of the H I 21 cm line with several UV and optical transitions. They were able to get a constraint of

$$\Delta x/x = (0.6 \pm 1.0) \cdot 10^{-5},$$

at $0.2 < z < 2.4$.

Srianand et al. (2010) used a single high redshift system ($z = 3.2$) and got an even more stringent bound of

$$\Delta x/x = (1.7 \pm 1.7) \cdot 10^{-6}.$$

Though a quite stringent bound on the variation of a combination of constants seems to be possible, the results have to be taken with care. A comparison of line positions that were taken with different instruments is very susceptible to systematic errors. Furthermore for this approach it is necessary to assume that the H I 21 cm line is originated in the same gas phase as the fine structure transition lines

Another possibility is to compare the position of the H I 21 cm line with molecular rotational transitions. With this method it is possible to trace the combination of constants $y := g_p\alpha^2$. Murphy et al. (2001a) used this method for two systems at $z_1 = 0.2$ and $z_2 = 0.7$. They got a constraint of

$$|\Delta y/y| < 5 \cdot 10^{-5},$$

using different rotational transitions of CO.

A similar analysis is possible by comparing fine structure transitions of C with rotational transitions of CO. A combination $F := \alpha^2\mu$ can be traced with this method. Curran et al. (2011) compared line positions of C I with rotational transitions of CO for 8 systems in $2.3 < z < 4.1$. They could constrain F to

$$|\Delta F/F| < 8 \cdot 10^{-5}.$$

To circumvent the problem of different molecules or ions originating in different gas phases, it is necessary to restrict the analysis to a single ion or molecule. This is possible with the 18 cm lines of

the ground state of OH. This state is split into four lines by Λ doubling and by hyper-fine splitting. Comparing line positions of these four transitions allows to set a constraint on a combination of constants $F = g_{\rm p}(\alpha^2\mu)^{1.57}$ (Chengalur & Kanekar 2003; Darling 2003). Assuming that the other constants are fixed Darling (2004) was able to constrain F to

$$|\Delta\alpha/\alpha| < 10^{-5}$$

at $z = 0.2$.

The possibility of constraining variations of fundamental constants with the use of a single molecule is very attractive, since it removes a significant error source. The main problem with this method is that only a small number of usable systems have been detected so far. Furthermore it is only possible to measure a combination of different constants. A possibility to constrain the fine-structure constant alone in high redshift systems is given by optical quasar spectra.

Optical spectra

The first approach to measure changes of the fine-structure constant α with astrophysical observations was made by Savedoff (1956). They used optical measurements of line positions of N II and Ne III fine structure doublets (Alkali Doublet Method) in the spectrum of Cygnus A, resulting in

$$\Delta\alpha/\alpha = (1.8 \pm 1.6) \cdot 10^{-3}$$

at $z = 0.06$.

Bahcall & Schmidt (1967) used a pair of O III emission lines in the spectrum of the Seyfert 1 Galaxy PKS0133+207 at $z \approx 0.2$. They reported a comparable accuracy of

$$\Delta\alpha/\alpha = (1 \pm 2) \cdot 10^{-3}.$$

In a further analysis they looked for position shift between Si II and Si IV fine structure transition lines in the spectrum of the quasar PKS0802+103. They found

$$\Delta\alpha/\alpha = (-2 \pm 5) \cdot 10^{-2},$$

at $z = 1.95$ (Bahcall et al. 1967).

Levshakov (1992) used catalogue data of 500 systems of doublets of alkali like ions in the spectra of 159 quasars spread over a wide redshift range $z \lesssim 4$ and obtained

$$\Delta\alpha/\alpha/dz = 2 \pm 2 \cdot 10^{-4}.$$

Potekhin & Varshalovich (1994) used catalogue data of 1441 pairs of lines of C IV, N V, O VI, Mg II, Al III and Si IV at a similar redshift range $0.2 < z < 3.7$. They obtained a similar result of

$$\Delta\alpha/\alpha/dz = (-0.6 \pm 2.8) \cdot 10^{-4}.$$

Levshakov (1994) made a detailed analysis of 5 Mg II systems at $z \sim 0.5$ in the spectrum of the Seyfert 1 galaxies PKS0454-22 and PKS2128-123. They pointed out the uncertainties that can arise from unresolved blends and a velocity substructure. They were able to get a weak constraint of

$$|\Delta\alpha/\alpha| < 0.5 \cdot 10^{-2}.$$

Varshalovich et al. (1996) got a more stringent result of

$$\Delta\alpha/\alpha = 2 \pm 7 \cdot 10^{-5},$$

using only the Si IV doublet for a in the lines of sight of 3 quasars at redshifts $2.8 \lesssim z \lesssim 3.1$.

Ivanchik et al. (1999) extended this work by analysing 20 absorption systems at $2 < z < 3.2$ in the lines of sight of 9 quasars using mainly Si IV lines. They obtained

$$\Delta\alpha/\alpha = (-3.3 \pm 6.5_{\rm stat} \pm 8_{\rm sys}) \cdot 10^{-5}.$$

Using the same method, Murphy et al. (2001c) decreased the limit to

$$\Delta\alpha/\alpha = (-0.5 \pm 1.3) \cdot 10^{-5},$$

using 21 Si IV systems in the lines of sight of 8 quasars.

The Alkali Doublet Method has the advantage that only transitions of a single ion are compared. Furthermore the distance between the lines is small, reducing problems with wavelength calibration. However, the accuracy of this method is limited by small sensitivities to an α variation.

Webb et al. (1999) compared line positions of Mg II transitions with Fe II transitions, using 30 systems in the lines of sight of 17 quasar spectra and obtained

$$\Delta\alpha/\alpha = (-1.1 \pm 0.4) \cdot 10^{-5}$$

at $0.6 < z < 1.8$. The data were obtained with the HIRES spectrograph at the KECK telescope (Vogt et al. 1994). In this approach line positions of different ions were compared (Many Multiplet (MM) Method). While this has the advantage that a higher difference in sensitivities was reached, it adds further systematic error sources if the ions do not trace exactly the same gas phase.

Using transitions of all available ions, namely Mg I, Mg II, Al II, Al III, Si II, Cr II, Fe II, Ni II and Zn II, Murphy et al. (2001b) found

$$\Delta\alpha/\alpha = (-0.72 \pm 0.18) \cdot 10^{-5}$$

at a redshift $0.5 < z < 3.2$. They analysed 49 absorption systems in 28 quasar spectra. The result remains constant with different transitions used. The Fe II and Mg II sample gave $\Delta\alpha/\alpha = (-0.7 \pm 0.23) \cdot 10^{-5}$ for $0.5 < z < 1.8$, comparing positions of Ni II, Cr II and Zn II gave $\Delta\alpha/\alpha = (-0.76 \pm 0.28) \cdot 10^{-5}$ for $1.8 < z < 3.5$, while Si IV gave $\Delta\alpha/\alpha = (-0.5 \pm 1.3) \cdot 10^{-5}$ for $2 < z < 3$ (Webb et al. 2001). With an additional independent sample of 78 absorption systems Murphy et al. (2003) extended their previous result to

$$\Delta\alpha/\alpha = (-0.57 \pm 0.10) \cdot 10^{-5},$$

at a redshift of $0.2 < z < 3.7$.

Using data taken with the UVES spectrograph at the VLT, Chand et al. (2004) analysed 23 Mg II and Fe II systems at a redshift of $0.4 < z < 2.3$. In contrast to the results by Murphy et al. (2003), they found

$$\Delta\alpha/\alpha = (-0.06 \pm 0.06) \cdot 10^{-5}.$$

Bahcall et al. (2004) pointed out the difficulties involved in comparing transitions of different ions. To circumvent this problem, Quast et al. (2004) introduced the Single Ion Differential α Measurement (SIDAM) method, which makes use of different signs in the sensitivities of Fe II transitions. Using just a single system in a high quality UVES spectrum of the quasar HE0515-4414 at a redshift $z = 1.15$, they obtained

$$\Delta\alpha/\alpha = (-0.4 \pm 1.9 \pm 2.7_{\mathrm{sys}}) \cdot 10^{-6}.$$

Levshakov et al. (2005) analysed the Fe II transitions of a single system at $z = 1.84$ toward the quasar Q1101-264 gave

$$\Delta\alpha/\alpha = (2.4 \pm 3.8_{\mathrm{stat}}) \cdot 10^{-6}.$$

A reanalysis of the $z = 1.15$ system towards HE0515-4414 gave

$$\Delta\alpha/\alpha = (0.4 \pm 1.5_{\mathrm{stat}}) \cdot 10^{-6}.$$

In a new analysis of the $z = 1.84$ system in the line of sight of the quasar Q1101-264, Levshakov et al. (2007) found a high position offset between the different Fe II transitions, that would correspond to an α variation of

$$\Delta\alpha/\alpha = (5.4 \pm 2.5) \cdot 10^{-6}.$$

Murphy et al. (2008) pointed out that the analysis by Chand et al. (2004) might be flawed, due to discontinuous χ^2 curves. A reanalysis by them gave a value similar to that obtained by the KECK/HIRES sample of

$$\Delta\alpha/\alpha = (-0.64 \pm 0.36) \cdot 10^{-6}.$$

The conflicting results led to an increased search for unregarded systematics. The wavelength calibration accuracy soon came into focus. Molaro et al. (2008b) used the UVES spectrograph to observe a reflected solar spectrum on the asteroids Iris and Juno. The positions of the reflected asteroid spectrum were compared with solar line positions. Radial velocity drifts of the order $10-50\,\mathrm{m\,s^{-1}}$ were found. These were, however, not systematically correlated with wavelength. Neither was a drift between the two arms of the spectrograph found.

Griest et al. (2010) compared the wavelength calibration of the KECK/HIRES data pipeline using Th-Arg lines, with calibrated data using an iodine cell. They found drifts between the two calibration methods of up to $3000\,\mathrm{m\,s^{-1}}$. Trying to calibrate the spectra as best as they could, they analysed a DLA system at $z = 2.31$. They were able to produce significant results with either sign depending on the set of lines and the fitting method used, concluding that the conflicting results are created by an underestimation of systematic errors.

With a combination of the previous KECK/HIRES data with a new calibration of a UVES sample of 153 systems, Webb et al. (2010) reported a 4σ signal of a spatial variation of the fine-structure constant along a dipole axis towards the equatorial coordinates $(17.3 \pm 0.6)\,\mathrm{hr}$ right ascension and $(-61 \pm 9)^\circ$ declination. In this analysis, the authors assumed that the main

systematic effects will average to zero in a large data sample and can thus be treated as statistics.

The approach by Webb et al. (2010) with the resulting 4σ signal of a spatial variation are an attempt to explain the apparent discrepancies between data sets. Results with a negative $\Delta\alpha/\alpha$ come exclusively from data that was taken with HIRES/KECK in the northern hemisphere, while the positive and zero results come from data taken with UVES/VLT in the southern hemisphere. Systematical problems in one of the instruments is a likely cause for this apparent variation.

Using a new high quality spectrum of the quasar HE0001-2340 Agafonova et al. (2011) got a result of

$$\Delta\alpha/\alpha = (-1.5 \pm 2.6) \cdot 10^{-6}$$

by comparing line positions of Si II with Fe II at $z = 1.58$.

In the UVES Large Program for testing fundamental physics a large set of observations was done with the UVES spectrograph at the ESO VLT telescope. As a first result an α variation was constrained to

$$\Delta\alpha/\alpha = (1.3 \pm 2.4_{\mathrm{stat}} \pm 1.0_{\mathrm{syst}}) \cdot 10^{-6}$$

by comparing line positions of Al II to Fe II transition at $z = 1.69$ in the line of sight of the quasar HE2217-2818 (Molaro et al. 2013).

The results of the analysis of optical quasar spectra are highly sensitive to observational procedures, data reduction, and methods of data analysis. However, when all systematics are thoroughly explored, the result will be completely model independent.

Chapter 3

Simulated data

3.1 Line profiles

Asymmetric line profiles can be formed by various mechanisms that generally cannot be distinguished in real data. Usually they are treated as a simple blend of two or more Doppler profiles. If the real composition of the system is more complex, line position fits can be erroneous. The aim of this chapter is to show that this error source cannot be neglected when searching for varying fundamental constants and other related analyses where a very high precision in line position measurements is required. During fitting procedures, Doppler or Voigt profiles are usually used to simulate the line. In this work we use only Doppler profiles because the damping wings of the observed lines are negligible at low column densities.

The derivation of the formulae we used to simulate our data follows Aller (1963). The intensity I_0 of the light of a distant source is reduced by absorption of an intermediate gas with the optical depth τ by

$$I = I_0 \cdot \exp(-\tau). \tag{3.1}$$

The optical depth is the integral of the opacity κ times the number density n over the spatial extension s of the absorber,

$$\tau_\lambda = \int \kappa n(s) \phi(\lambda, s) \mathrm{d}s, \tag{3.2}$$

with $\kappa = \frac{\pi e^2}{m_e c^2} \cdot f\lambda_0$. f and λ_0 are the oscillator strength and the laboratory wavelength of a specific transition, respectively, and ϕ is the profile function. When we consider thermal broadening as the dominant mechanism a Doppler profile is used, giving

$$\tau_\lambda = \frac{\sqrt{\pi} e^2}{m_\mathrm{e} c^2} f\lambda_0 \cdot \int \frac{n(s)}{b(s)} \exp\left(- \left(c \frac{\lambda - \lambda_c}{b(s)\lambda_c} \right)^2 \right) \mathrm{d}s, \tag{3.3}$$

where $\lambda_\mathrm{c} = (1+z)(1+v(s)/c) \cdot \lambda_0$ is the observed central wavelength of the line, z the redshift, and $v(s)$ the macroscopic velocity of the absorbing medium. The Doppler parameter b is a measure of the line width, usually simplified as a combination of thermal broadening and turbulent velocity $b = \sqrt{b_\mathrm{th}^2 + b_\mathrm{turb}^2}$, with $b_\mathrm{th} = \sqrt{\frac{2kT}{m}}$, and m the mass of the ion. Since the temperature, density distribution and turbulence of the absorbing system are not known, eq. 3.3 cannot be solved analytically. Under the assumption of a constant temperature and turbulence, and no changes in the velocity field throughout the absorber, the optical depth can be written as

$$\tau_\lambda = \frac{\sqrt{\pi} e^2}{m_\mathrm{e} c^2} \frac{f\lambda_0 N_\mathrm{c}}{b} \cdot \exp\left(- \left(c \frac{\Delta\lambda^2}{b^2} \right) \right), \tag{3.4}$$

where $\Delta\lambda$ is the wavelength distance from the redshifted line centre $\Delta\lambda = \frac{\lambda - \lambda_\mathrm{c}}{\lambda_\mathrm{c}}$ and N_c is the column density, defined as the integral of the density over the length of the absorber $N_\mathrm{c} = \int n(s)\mathrm{d}s$. In the following the notation $N := \log \frac{N_\mathrm{c}}{\mathrm{cm}^{-2}}$ will be used. This profile is generally accepted and will be used in sect. 3.4.1. In sect. 3.4.2 the necessary assumptions for this profile are abandoned to create more realistic line shapes.

The instrument measures the flux $F_\lambda = \int I_\lambda \cos\vartheta \mathrm{d}\Omega$, which is the intensity integrated over the solid angle of the source. Since quasars are

point sources, the behaviour of the flux and of the intensity are the same.

The flux is finally convoluted with the spectrograph point spread function P,

$$F_\lambda = F_0 \cdot \exp(-\tau) \otimes P_\lambda, \tag{3.5}$$

where P is assumed to be a Gaussian with the width $\sigma_\lambda = \frac{\lambda}{2\sqrt{2ln2}R}$. The resolving power $R = \lambda/\Delta\lambda$ is defined as the smallest distance $\Delta\lambda$ at which two features can be separated.

To create a distortion of the original line profiles, noise was added to the resulting spectra. For our purposes it proved sufficient to add a Poisson distributed noise, though a combination of Poisson noise and Gaussian noise would be a more realistic data simulation. In most cases the simulations were done with a high data quality that reproduces the quality of recent, current, or possible future observations.

3.2 The fit code

3.2.1 A combined position measurement of complex systems

The simulated spectra were fitted in the same way as real data to allow a direct comparison of the results. The code used to fit the data was developed by Quast et al. (2005). Instead of the usual deterministic approach it uses an evolution strategy Hansen & Ostermeier (2001), which is a randomised way of fitting the data. This procedure has the advantage of a higher independence from start parameters at the cost of a higher computation time.

Redshift z, column density N, and Doppler parameter b should be identical for different transitions of the same ion and are thus fitted simultaneously. A common approach is to include the α variation as a fourth fit parameter. This method gives the value for $\Delta\alpha/\alpha$ that fits the data best, regardless of the cause of position shifts between the transitions. In this work a different approach was used. The position of each line was measured and subsequently the cause for eventual position shifts investigated.

Absorption system usually consist of several lines and each line of several components. For the α variation measurements we used relative positions of whole systems, rather than directly comparing positions of single components, i.e. in the fitting procedure the Doppler parameters b, column densities N, and distance between the components were assumed to be the same for all transitions, while the position of each system was fitted individually. We defined a system as an accumulation of close lines with no clear continuum between them.

The original code by Quast et al. (2005) was modified allowing to fit the distance between neighbouring components simultaneously. The number of free parameters for this method of data fitting is $p = 3n_c - 1 + n_t$, where n_c is the number of components and n_t the number of simultaneously fitted transitions. The Doppler parameters b and the column densities N are fitted for each component and thus give $2n_c$ free parameters, while the distance between two components give $n_c - 1$ free parameters. The position of the whole system for each transition add another n_t parameters.

To test the enhanced code, a set of simulations was done. A blend of two lines was simulated with different line parameters. The velocity distance of the fitted line centres of the stronger component between Fe II 1608 and Fe II 2600 was measured. A comparison of the results of both versions of the code is shown in Figs. 3.1 and 3.2. Each row shows a different line composition. The first two columns show the simulated spectra while the position shifts are plotted as histograms in the third column for the original code (RQ-EDFIT) and in the fourth column for the modified code (NP-EDFIT). The histograms were created from fits of 100 instances with random noise. The curves show Gaussian curves centred at 0 with the width equal to the average statistical error of the line position fit. The lines have Doppler parameters of $b_1 = 2\,\mathrm{km\,s^{-1}}$ and $b_2 = 4\,\mathrm{km\,s^{-1}}$, respectively, in every set-up. The column densities are given in the plots. The distance between the two components is $\Delta v = 4\,\mathrm{km\,s^{-1}}$. The simulations were done with a resolving power of $R = 53\,000$ and a signal to noise ratio of $S/N = 100$. In Table 3.1 the average position offsets between Fe II 1608 and Fe II 2600 are given for the different line compositions. The error given is the average statistical line position fit error. In all cases the new code produces better or similar results. The highest offsets occur for strong lines because of saturated line profiles in the stronger transitions. The saturation in theses cases is unre-

Table 3.1: Position shifts between Fe II 1608 and Fe II 2600 for the original (Δv_{Rq}) and the modified (Δv_{Np}) code.

N_1	N_2	Δv_{Rq} [km s^{-1}]	Δv_{Np} [km s^{-1}]
12.5	12.5	0.01 ± 0.26	0.02 ± 0.22
12.5	13.0	0.01 ± 0.27	0.00 ± 0.25
12.5	13.5	0.05 ± 0.18	0.02 ± 0.15
13.0	12.5	0.01 ± 0.09	0.02 ± 0.08
13.0	13.0	-0.02 ± 0.09	0.01 ± 0.08
13.0	13.5	0.07 ± 0.14	0.00 ± 0.10
13.5	12.5	-0.00 ± 0.04	0.01 ± 0.04
13.5	13.0	-0.03 ± 0.04	-0.00 ± 0.04
13.5	13.5	-0.11 ± 0.06	0.03 ± 0.04

The first two columns show the column densities of the the blended lines. The corresponding Doppler parameters are $b_1 = 2\,\mathrm{km\,s^{-1}}$ and $b_2 = 4\,\mathrm{km\,s^{-1}}$, respectively.

solved, that after convolution with the instrument profile there is no part of the line with zero flux. For the strongest systems the new code also produces position shifts of $\Delta v \approx 30\,\mathrm{m\,s^{-1}}$ because of unresolved saturation. These are, however, reduced by a factor of three in comparison the original code and within 1σ of the statistical position fit error.

Though in most cases the position shifts are smaller than the fitting errors, for future observations with a higher data quality they can be of importance. This method is not necessary when the α variation in used as another fit parameter, because in that approach the line positions, and thus the distances between the components, are fitted simultaneously.

3.2.2 Narrow lines

For fitting lines that are narrow in comparison to the pixel resolution of the data, the original code is too simple and produces erroneous results. The flux value is calculated at each pixel and thereafter the convolution with the instrument profile is done. The convolution conserves the area under the profile, but the original profile is just an approximation of the real line profile. The higher the pixel resolution is, the better is the approximation. In Fig. 3.3 the profiles of two narrow artificial lines, with $b = 1\,\mathrm{km\,s^{-1}}$, are calculated with a low pixel resolution ($\Delta\lambda = 0.035\,$Å). One line has its centre directly at a pixel, the second directly between two pixels. The solid lines show the line profile before and after the convolution with the instrument profile. The positions of the pixels are indicated by the crosses. As a comparison the lines are shown for a ten times higher pixel resolution in grey. Though the calculated points of the original profile are correct, after convolution with the instrument profile, the result differs significantly from the higher pixel resolution lines. The shape is strongly dependent on the position of the line in respect to the pixels. This effect produces wrong fitting results for narrow lines, especially in low resolution spectra.

The fit code was modified to allow a more realistic simulation of the instrument profile. For narrow lines the resolution for the flux value calculations is increased by a factor ten. After the convolution with the instrument profile the resolution is contracted by averaging over an interval around each original pixel. To test this procedure a set of artificial spectra was created with this expansion method. A single line with increasing Doppler parameters beginning from $b = 1\,\mathrm{km\,s^{-1}}$ was simulated. A column density of $N = 13.5$ was used. An oscillator strength of $f = 0.0577$ was used, representing Fe II 1608. This gives strong, unsaturated line profiles for all simulated instances. The pixel resolution was the same as in Fig. 3.3. Fig. 3.4 shows corresponding position fits with the classical method (NP-EDFIT) and the expansion method (NP-EXP). The error bars represent the spread of the results of 100 realisations with random noise. The plot shows the limits of the classical fitting procedure. At Doppler parameters $b \gtrsim 4\,\mathrm{km\,s^{-1}}$ both methods give the same results. For higher pixel resolutions, also narrower lines can be fitted correctly with the classical method. Though the effect is even stronger for Doppler parameter b and column density N fits, position shifts up to a few hundred $\mathrm{m\,s^{-1}}$ can occur for very narrow lines, depending on the position of the line in respect to the pixel.

To determine the smallest Doppler parameters b that can be fitted with the original code, another set of simulations was done. For different pixel resolutions in steps of 0.005 Å, unsaturated artificial lines ($N = 13.5$, $f = 0.0577$) were created with Doppler parameters ranging from $b = 0.25\,\mathrm{km\,s^{-1}}$ to $b = 5.00\,\mathrm{km\,s^{-1}}$ in steps of $\Delta b = 0.25\,\mathrm{km\,s^{-1}}$.

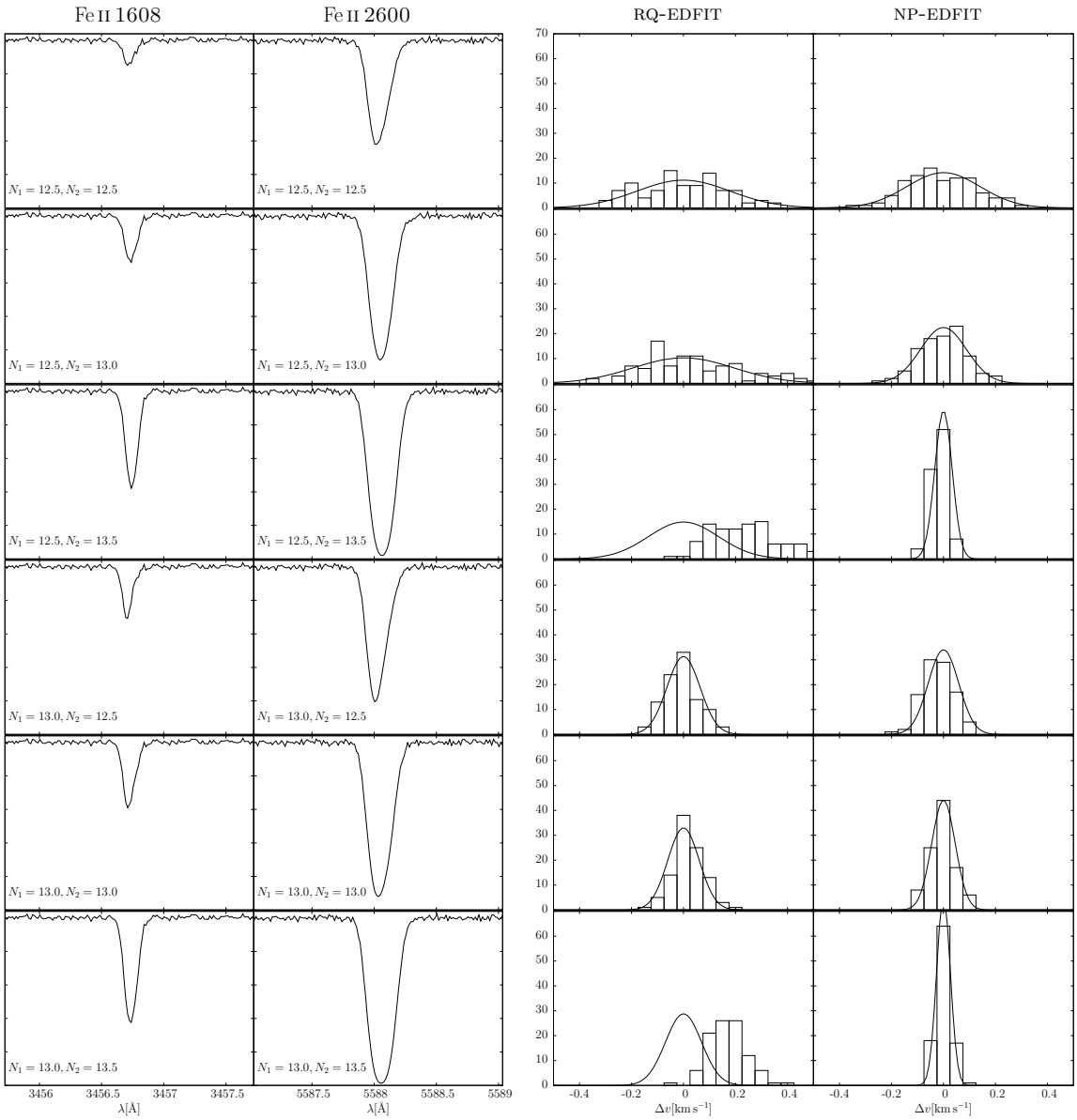

Figure 3.1: Line profiles and position shifts between the first component of blended Fe II 1608 and Fe II 2600 features. RQ-EDFIT is the original fit code and NP-EDFIT the modified code to allow for constant distances between neighbouring components. Lines are simulated as two blended components with $b_1 = 2\,\mathrm{km\,s^{-1}}$ and $b_2 = 4\,\mathrm{km\,s^{-1}}$. The column densities are given in the plots.

For each line 100 realisations with random noise were fitted. Figure 3.5 shows the minimum Doppler parameter b for the corresponding pixel resolution for which the average line position fit difference between the two fitting methods is smaller than $\Delta v = 10\,\mathrm{m\,s^{-1}}$. The precise values depend on the position of the line in respect to the pixels. The line shows a linear regression through the points. The result was adopted as a threshold for the use of the expansion method in the fitting code to avoid unnecessary computation time.

By varying a single fit parameter around its best

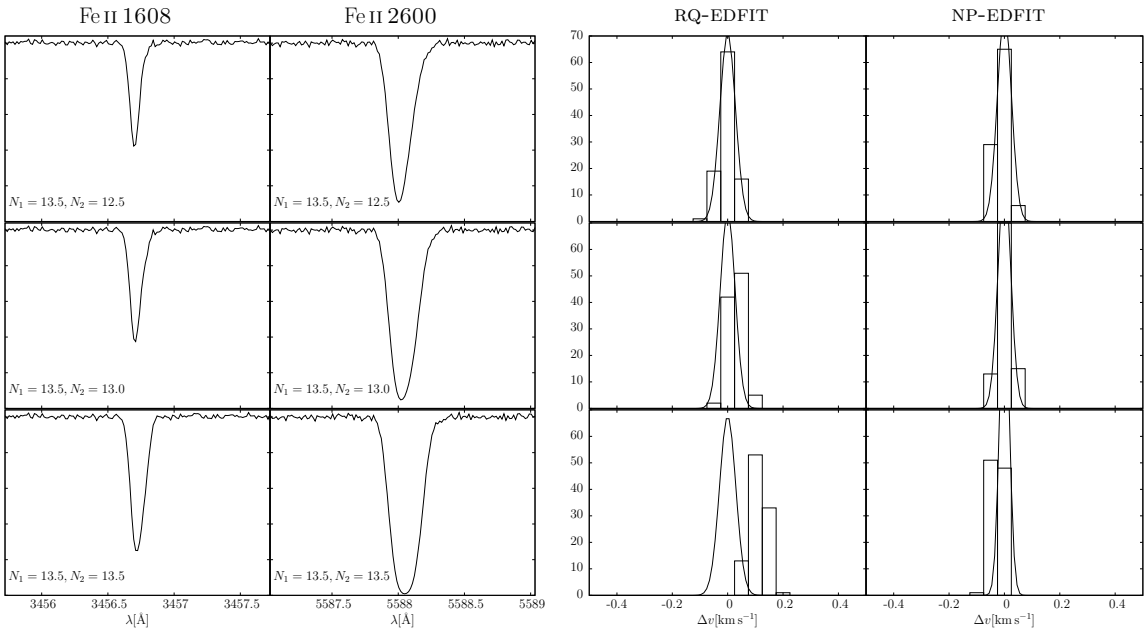

Figure 3.2: Line profiles and position shifts between the first component of blended Fe II 1608 and Fe II 2600 features. RQ-EDFIT is the original fit code and NP-EDFIT the modified code to allow for constant distances between neighbouring components. Lines are simulated as two blended components with $b_1 = 2\,\mathrm{km\,s^{-1}}$ and $b_2 = 4\,\mathrm{km\,s^{-1}}$. The column densities are given in the plots.

fit value, a χ^2 curve can be plotted. The 1σ confidence level is given by the position for which $\chi^2_{1\sigma} = \chi^2_{\mathrm{min}}+1$. The curve is parabolic near its minimum. When plotting χ^2 curves for lines with small Doppler parameters and a low pixel resolution, it is necessary to use the expansion method when calculating the convolution with the instrument profile, else the χ^2 curve is overlaid with an oscillating curve on the scale of the pixel distance because the shape of the simulated line profile varies depending on the position of the line in respect to the position of the pixels. Figure 3.6 shows χ^2 curves for the line position parameter for a line simulated as in the previous simulations with $b = 1\,\mathrm{km\,s^{-1}}$. The left curve shows the result for a direct pixel per pixel calculation, the right curve for the expansion method. In grey the positions of the pixels are shown.

3.3 Symmetric profile

As a first step the whole procedure was simulated using ideal conditions. Because of the different strengths of the Fe II transitions just a small range of parameters give systems with an adequately strong Fe II 1608 transition without saturation in the stronger transitions. For narrow lines ($b \approx 1\,\mathrm{km\,s^{-1}}$) Fe II 2383 is saturated at $N \gtrsim 13$, for broader lines with $b \approx 3\,\mathrm{km\,s^{-1}}$ at $N \gtrsim 13.5$.

A single symmetric strong line ($N = 13.5, b = 2\,\mathrm{km\,s^{-1}}$) was simulated with various data qualities. The resolving power ranges from $R = 50\,000$ to $R = 100\,000$ and the signal to noise ratio from $S/N = 100$ to $S/N = 150$. The six abundant Fe II transitions were simulated 1000 times with random noise. A regression analysis was made to calculate a possible α variation for each single case. Fig. A.1 shows histograms of the measured α variation for different data qualities. The standard deviation of the average of the resulting $\Delta\alpha/\alpha$ values indicates the achievable precision of the α variation calculations for the given data quality. In Fig. 3.7 this accuracy is plotted over the resolving power for three different values for the signal to noise ratio S/N. Under ideal conditions, meaning a single, strong, narrow, and symmetric line an accuracy of $\delta\frac{\Delta\alpha}{\alpha} \sim 2 \cdot 10^{-7} - 7 \cdot 10^{-7}$ (statistical) could be reached. Comparing just the po-

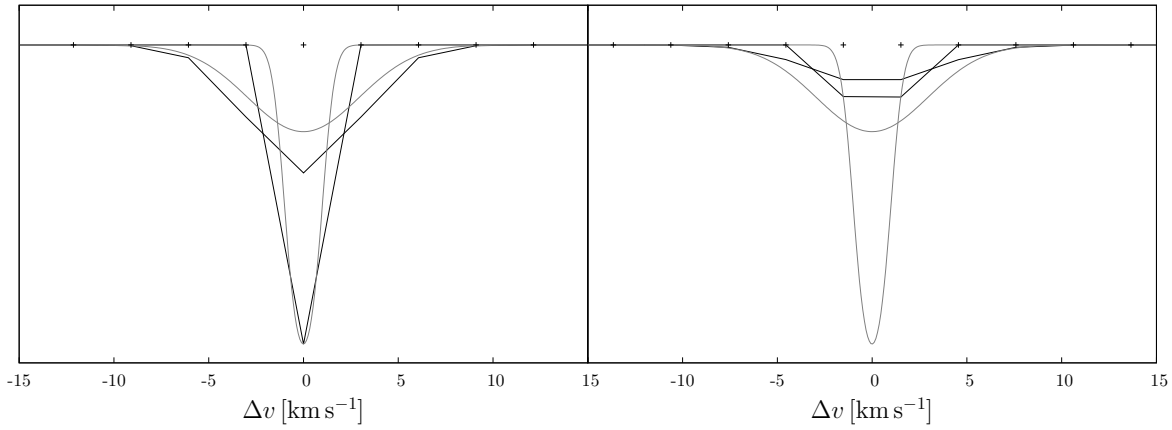

Figure 3.3: Narrow line ($b = 1\,\mathrm{km\,s^{-1}}$) simulated for a low pixel resolution spectrum prior and after convolution with the instrument profile. Left: The line centre is located directly at a pixel. Right: The line centre is located in the middle of two pixels. In grey a simulation with a ten times higher pixel resolution is shown.

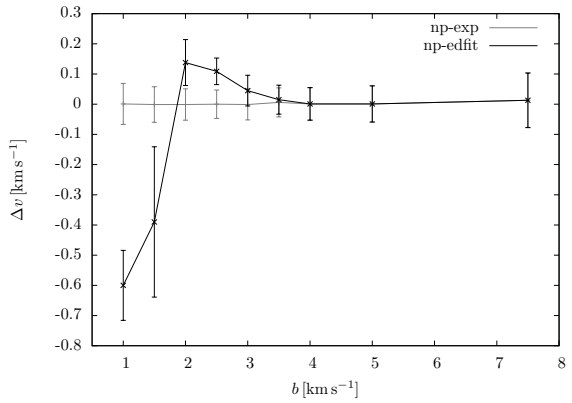

Figure 3.4: Positions fits of artificial spectra with expanded pixel resolution. The black line shows the classical fitting procedure and the light grey line shows the expanded fitting procedure. Velocity shifts Δv between fitted and original line centre are plotted over the Doppler parameter b of the line.

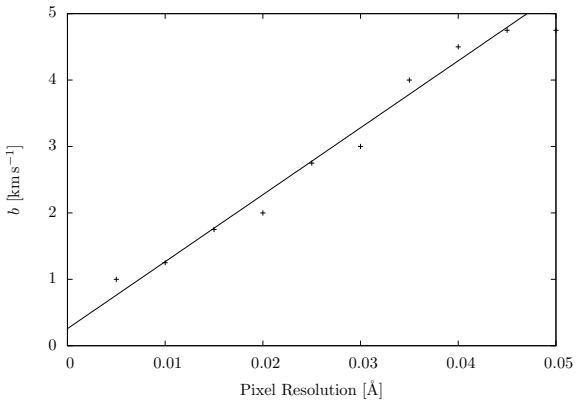

Figure 3.5: Minimum Doppler parameter b for which the position fit difference of the original code NP-EDFIT and the expansion method NP-EXP is smaller than $\Delta v = 10\mathrm{m\,s^{-1}}$.

sitions of Fe II 1608 with Fe II 2374 decreases the theoretically achievable precision just slightly to $\delta\frac{\Delta\alpha}{\alpha} \sim 3 \cdot 10^{-7} - 1 \cdot 10^{-6}$.

3.4 Asymmetries

In real data a majority of metal absorption lines in quasar spectra are not perfectly symmetric. Usually these lines are handled as a simple blend of two or more components. The true origin of the line shape, however, is unknown. Fit errors represent the uncertainties of the parameter placement for a given model. When the model is wrong in the first place the errors can be underestimated.

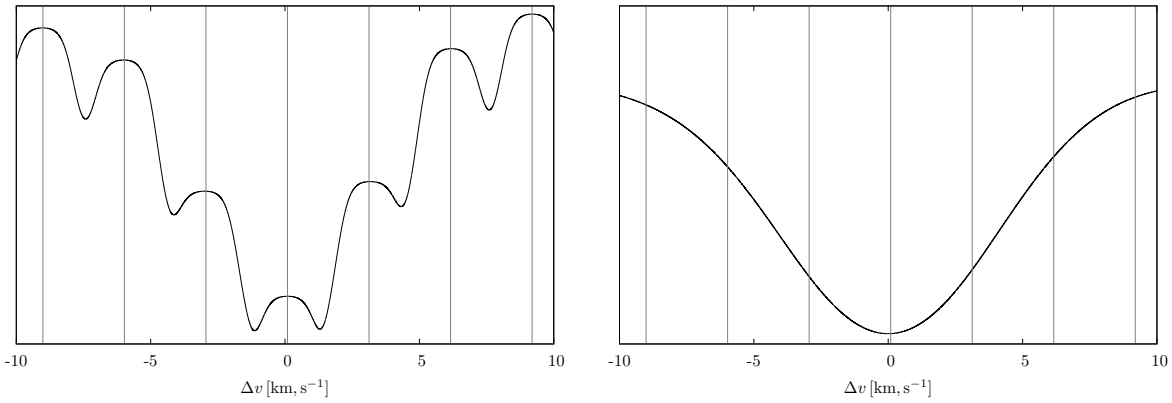

Figure 3.6: χ^2 curve of a narrow line in a low resolution spectrum. The left curve shows a direct per pixel convolution with the instrument profile, the right curve a convolution with the expansion method. In grey the positions of the pixels are shown.

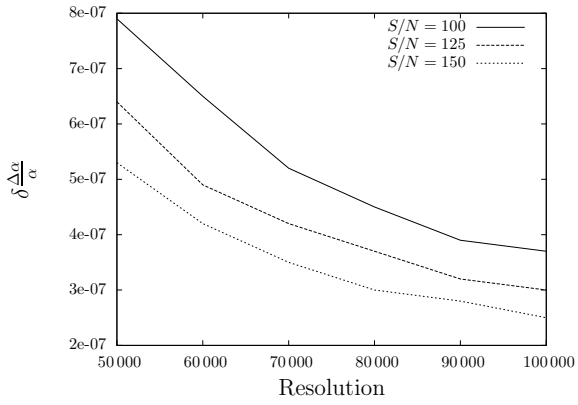

Figure 3.7: Precision of α variation measurement for a single symmetric line profile using the SIDAM method. The three curves represent different signal to noise ratios.

Several simulations were done to create artificial spectra with asymmetric line profiles. In sect. 3.4.1 the lines were created as blends of Doppler Profiles while in sect. 3.4.2 the profile was generalised to simulate realistic absorber conditions.

3.4.1 Unresolved blends

Single ion

At a gas temperature of $100\,\mathrm{K} < T_{\mathrm{kin}} < 10^4\,\mathrm{K}$, as is expected in interstellar clouds, the thermal width of Fe II absorption features is less than $2\,\mathrm{km\,s^{-1}}$. In the Galactic interstellar clouds b-parameters as low as $b \approx 0.5\,\mathrm{km\,s^{-1}}$ have been observed in Ca II and Na I (Welty 1998). Since many observed systems are broader, these are either broadened by turbulence, formed at higher temperatures or are blends of narrow lines.

Two examples for simulated narrow line blends are shown in Figs. 3.8 and 3.9. The first feature is composed of four components with the column densities $N_1 = 13.0$, $N_2 = 13.5$, $N_3 = 13.0$, $N_4 = 12.5$, and the second with $N_1 = 13.5$, $N_2 = 13.0$, $N_3 = 12.5$, $N_4 = 12.0$, respectively. The Doppler parameters for each component are $b = 1\,\mathrm{km\,s^{-1}}$, and the redshift separation between the components is $\Delta z = 2 \cdot 10^{-5}$ ($\Delta v \approx 2.8\,\mathrm{km\,s^{-1}}$). Each of the relevant six Fe II transitions is shown. For the strong transitions it can be seen that though the original lines are highly saturated, the resulting feature no longer shows signs of saturation. The distortion of the line shape by this effect varies with the strength of the transition and the composition of the original spectrum.

The resulting profiles are fitted as a sum of Doppler profiles with an increasing number of components. The Doppler parameters b, column densities N, and separations between individual components of all Fe II transitions were fitted simultaneously, while the position of each transition was fitted individually. This procedure yields relative

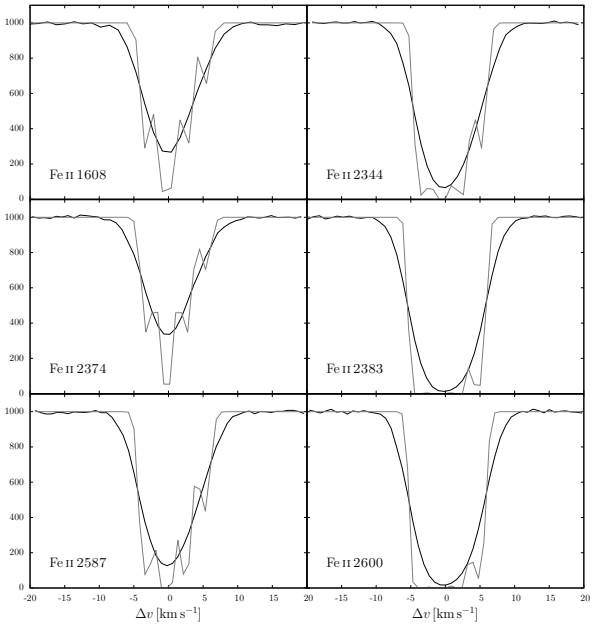

Figure 3.8: Simulated spectra of a line consisting of four blended components with the column densities $N_1 = 13.0,\ N_2 = 13.5,\ N_3 = 13.0,\ N_4 = 12.5$ and the Doppler parameter $b = 1\,\mathrm{km\,s^{-1}}$. The original spectrum, prior to convolution with the instrument profile, is over-plotted by the final spectrum.

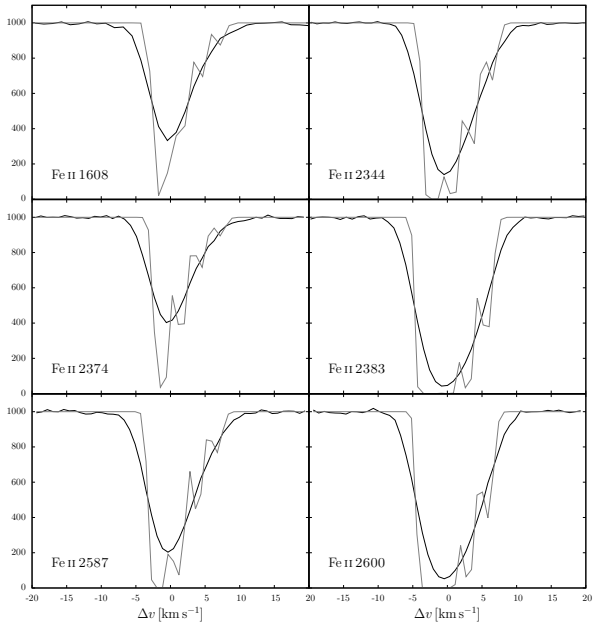

Figure 3.9: Simulated spectra of a line consisting of four blended components with the column densities $N_1 = 13.5,\ N_2 = 13.0,\ N_3 = 12.5,\ N_4 = 12.0$ and the Doppler parameter $b = 1\,\mathrm{km\,s^{-1}}$. The original spectrum, prior to convolution with the instrument profile, is over-plotted by the final spectrum.

positions of all Fe II lines on a velocity or redshift scale.

Figures 3.10 and 3.11 show histograms of the velocity shift between the given transitions and Fe II 1608 for the first set-up with two and three fitted components, respectively. The results for the second set-up is shown in Figs. 3.12 and 3.13. The histograms were created by fitting 100 instances of the simulated spectra with random noise. Results for one, four, and five component fits are shown in Figs. A.2 and A.3.

It is not trivial to determine the optimum number of fit components. While an increase of the number of components decreases the χ^2 value, the scatter of the results increases. When the shape of the line is reasonably well approximated by a certain number of components, noise effects are primarily responsible for the location of further components. In these simulations we have chosen a two-component fit as best solution, though the three-component fits give smaller velocity shifts and have a lower χ^2 value. The scatter of the fit results is lowest for the two-component fit, allowing the best predictability for real data fits. Table 3.2 shows the averaged apparent α variation for both set-ups and an increasing number of components. The error represents the spread of the results. Averaged χ^2 values are given for each number of components. Fitting more than two components increases the spread of the results in both cases (compare Fig. 3.12 and Fig. 3.13).. This shows the main danger when using too many components. Apparently the result becomes less predictable, because the position of the third component is mainly governed by noise. In many cases the fit code could not clearly place a third component. These cases naturally have a higher statistical error in the total position fit since the location of all components are correlated.

The two-component fit of the first set-up gave two separated solutions (see Fig. 3.10). Depending on the transition strength, systematic shifts of up to $\Delta v \approx 400\,\mathrm{m\,s^{-1}}$ can occur. The effect can go in either direction even when the original line compo-

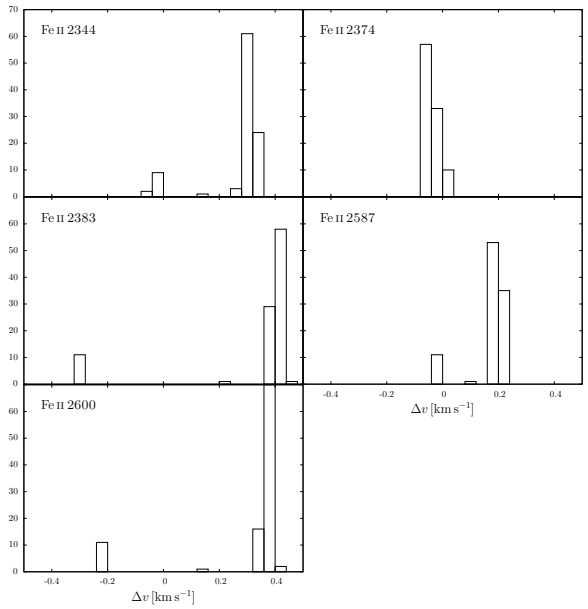

Figure 3.10: Histograms of the apparent velocity shifts relative to Fe II 1608 of close line blends simulated as in Fig. 3.8. Two-component fit for 100 realisations with random noise.

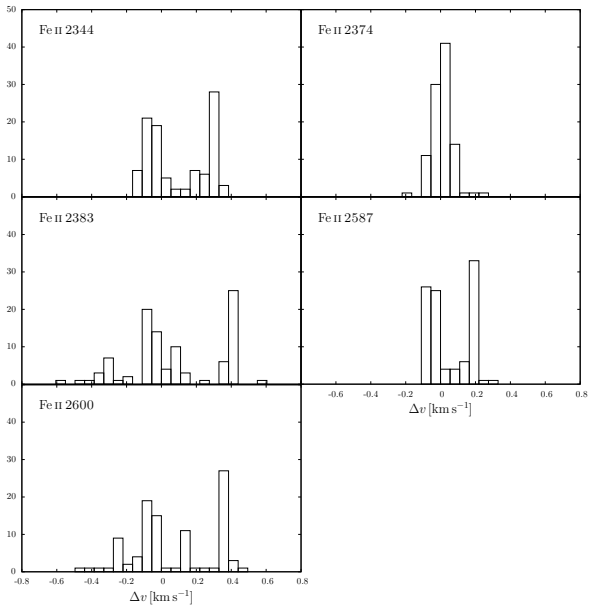

Figure 3.11: As in Fig. 3.10. Histograms of close line blends. Three-component fit for 100 realisations with random noise.

sition is the same, depending on the resulting best fit parameters.

In the first set-up, in 96% of the cases a composition of $N_1 = 13.5, b_1 = 1.6\,\mathrm{km\,s^{-1}}, N_2 = 13.3, b_2 = 3.2\,\mathrm{km\,s^{-1}}$ is favoured by the χ^2 analysis, while in the other cases $N_1 = 13.6, b_1 = 2.6\,\mathrm{km\,s^{-1}}, N_2 = 12.7, b_2 = 0.7\,\mathrm{km\,s^{-1}}$ has the lowest χ^2. The second set-up shows a homogeneous shift to the other direction though the shape of the line is asymmetric in the same direction. The best fit gives a composition of $N_1 = 13.5, b_1 = 1.7\,\mathrm{km\,s^{-1}}, N_2 = 12.8, b_2 = 3.2\,\mathrm{km\,s^{-1}}$. An α variation of $\Delta\alpha/\alpha = (6.0 \pm 1.0) \cdot 10^{-6}/(-3.7 \pm 0.7) \cdot 10^{-6}$ for the first set-up and $\Delta\alpha/\alpha = (-1.8 \pm 0.7) \cdot 10^{-6}$ for the second set-up is mimicked.

The statistical error is quite low because of the high data quality of the simulations. The systematic error introduced by this effect is up to four times higher. The problem involved is created by an incorrect deconvolution of the original spectrum. The narrow lines of the simulated systems are often affected by unresolved saturation while the fitted, broader lines are not. The degree of saturation depends on the transition strength. Thus the effect decreases when two transitions with similar strengths are compared.

Different ions

When comparing line positions of different ions, there is always the possibility of shifts due to a different ionisation stratification and differential dust depletion in the absorber. Usually the general composition of absorption systems look quite similar in Fe II and Mg II, the strength of single components, however, often show differences. Assuming that the lines can be deconvolved correctly this would not be problematic. If they are, however, composed of several unresolved narrow lines, this could produce an error that is generally overlooked. Like in sect. 3.4.1, in this section line profiles are simulated that consist of several narrow blended lines. The relative strength of each component is slightly different for Fe II and Mg II. The top row of Figure 3.14 shows the spectra of Fe II 2383 with $N_1 = 12.5$, $N_2 = 13.0$, $N_3 = 12.5$. $N_4 = 12.0$ and Mg II 2804 with $N_1 = 12.0$, $N_2 = 13.0$, $N_3 = 12.5$. $N_4 = 12.5$, respectively. The right side of Fig. 3.14 shows histograms of line positions of a one component fit of

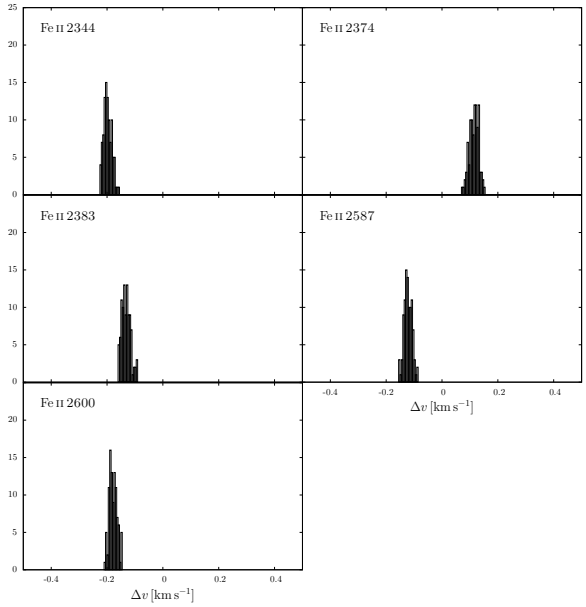

Figure 3.12: Histograms of the apparent velocity shifts relative to Fe II 1608 of close line blends simulated as in Fig. 3.9. Two-component fit for 100 realisations with random noise.

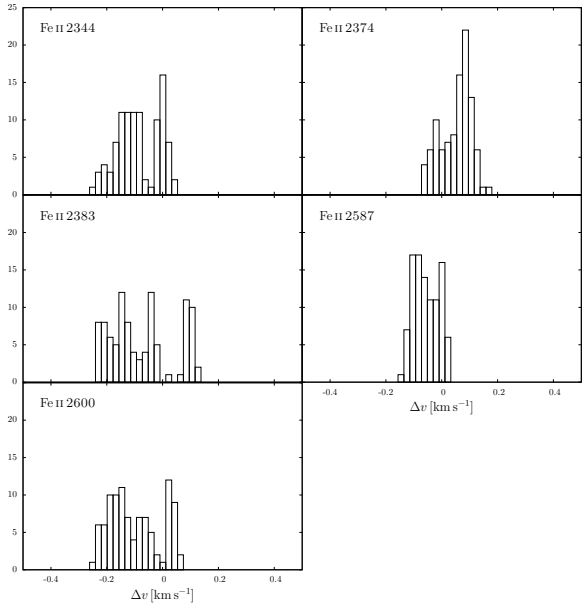

Figure 3.13: As in Fig. 3.12. Histograms of close line blends. Three component fit for 100 realisations with random noise.

both transitions. A shift of $\Delta v \gtrsim 1\,\mathrm{km\,s^{-1}}$ between Fe II 2383 and Mg II 2804 is produced. The statistical error given by the fit code is depicted by the Gaussian. A two component fit gives a similar result. In most cases the effect will be smaller, but harder to detect. In a second set of simulations, shown in Fig. 3.14 (bottom) (Fe II 2383: $N_1 = 12.3$, $N_2 = 13.0$, $N_3 = 12.5$, Mg II 2804: $N_1 = 12.5$, $N_2 = 13.0$, $N_3 = 12.3$) an offset between Fe II 2383 and Mg II 2804 of $\Delta v \approx 380\,\mathrm{m\,s^{-1}}$ is created. Already small differences in strength of neighbouring components can create strong position shifts. In real data it is often seen that close components of the same absorption system have different column densities in Fe II and Mg II. This will be also the case for unresolved components. A possibility to detect these cases in real data is discussed in sect. 3.4.5.

Figure 3.15 shows the distance between the line position fits of the two Mg II transitions for the first set-up (a) and the second set-up (b), respectively. Though they have the same line composition, the unresolved substructure led to position shifts of $\Delta v \approx 60\,\mathrm{m\,s^{-1}}$ because of the different transition strengths $f\lambda_0$. When in future instruments wavelength calibration problems are under control, shifts between two close lying transitions of the same ion with no difference in sensitivity to α variation, can be used as an indicator of unresolved substructure and an underestimation of the fit error.

3.4.2 Velocity fields

When we abandon the assumption of a constant velocity of the absorbing medium, Eq. 3.3 has to be calculated numerically for a given density distribution $n(s)$ and velocity field $v(s)$. Because very little is known about the absorbing medium, the aim of this section is not to create a hydrodynamically correct representation. In that case the density and velocity fields would be connected by the continuity equation. The aim is rather to create a simple realistic model that produces asymmetric line profiles in a single component. Nevertheless, it would be impractical to use it in a fitting procedure since there are too many parameters, which would result in ambiguous solutions.

By exploring several possibilities a wide vari-

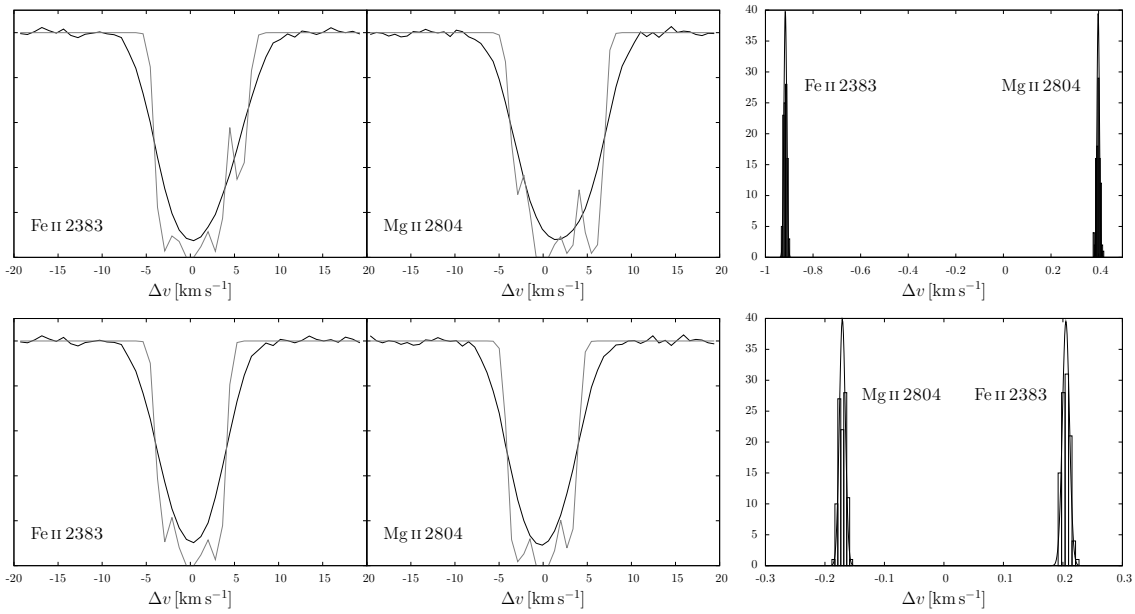

Figure 3.14: Left: Original and convolved flux of narrow line blend of Fe II 2383 and Mg II 2804 for the first (top) and the second (bottom) set-up. Right: Velocity distances between Fe II2383 and Mg II 2804 for 100 realisations with random noise.

Table 3.2: Simulation results of narrow line blends.

	Set-up 1		Set-up 2	
$\#_{\mathrm{comp}}$	$\Delta\alpha/\alpha\,[10^{-6}]$	χ^2	$\Delta\alpha/\alpha\,[10^{-6}]$	χ^2
1	-18.1 ± 2.6	1.9	-44.5 ± 4.5	4.5
2	6.0 ± 1.0 / -3.7 ± 0.7	1.3	-1.8 ± 0.7	1.2
3	1.8 ± 4.4	1.2	-0.8 ± 1.3	1.1
4	3.0 ± 4.6	1.3	-1.1 ± 1.6	1.1
5	1.6 ± 4.1	1.3	-2.3 ± 2.2	1.1

The $\Delta\alpha/\alpha$ values are determined for two different simulation set-ups, fitted with up to five components each. They are averaged over fits of 100 instances with random noise. The error represents the spread of the results. The second column for each set-up shows the averaged χ^2 values of the line profile fits.

ety of line shapes can be produced. As an example a continuous but asymmetric density distribution $n(s) \sim s \cdot \mathrm{e}^{-s}$ and a linear velocity field are used. The size of the absorber is parametrised along the line of sight s. A thermal broadening of $b = 2\,\mathrm{km\,s^{-1}}$ is used to approximate the typical Fe II line width in quasar spectra. The density distribution is adjusted to result in a column density of $N_1 = 13.0$ or $N_2 = 13.5$. In the first case the lines are not saturated, in the second case the strong transitions are saturated. The average gas velocity is $v_m = 0\,\mathrm{km\,s^{-1}}$. Artificial spectra were created, differing in column density and the highest velocity difference v_p in the system. Figure 3.16 shows the density distribution and velocity field for $N = 13.0$ and $v_\mathrm{p} = 10\mathrm{km\,s^{-1}}$. Since the size of the absorption system has no direct influence on the shape of the absorption lines, it is parametrised from 0 to 1. The high number density values given in Fig. 3.16 are a consequence of the parametrisation of the line of sight. A physically small absorber with a high number density gives the same absorption profile as an extended system with a low density. Figures 3.17 and 3.18 show the resulting spectra before and after convolution with the instrument profile for $N_1 = 13.0$ and $N_2 = 13.5$, respectively. The peak velocities are $v_\mathrm{p} = 0\,\mathrm{km\,s^{-1}}$, $v_\mathrm{p} = 10\,\mathrm{km\,s^{-1}}$, and $v_\mathrm{p} = 20\,\mathrm{km\,s^{-1}}$. Broader and therefore more asymmetric profiles are less influenced by the instrument profile, and the problem of unresolved saturation decreases. Small asymmetries, which are not visible by eye, are more prone to errors. The spectra of the other Fe II transitions and of further gas velocities are shown in App. A.3.

When fitting these profiles, the fit code cannot re-

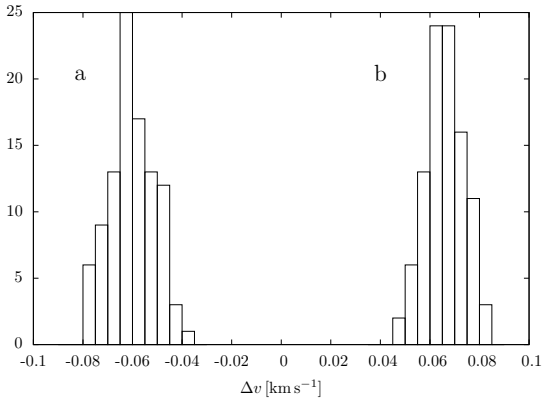

Figure 3.15: Apparent relative velocity shifts between Mg II 2796 and Mg II 2804 for the first set-up (a) and the second setup (b). 100 realisations with random noise.

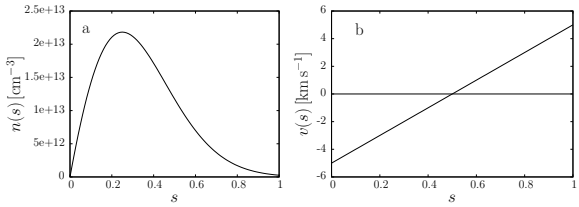

Figure 3.16: Number density (a) and velocity field (b) of absorbing medium used in the simulation of asymmetric line profiles, parametrised along the line of sight s with $N = 13$ and $v_\mathrm{p} = 10\,\mathrm{km\,s^{-1}}$. $n(s)$ is the density distribution and $v(s)$ the velocity field.

cover the original line composition, because the fit is made under the assumption that the line is composed of a finite blend of Doppler profiles. The best possible solution is a good approximation of the real line profile. This is also the case for real data because the properties of the absorbing medium are generally unknown and supposedly complex. The simulate spectra were fitted with an increasing number of components. Histograms were created for gas velocities ranging from $v_\mathrm{p} = 0\,\mathrm{km\,s^{-1}}$ to $v_\mathrm{p} = 20\,\mathrm{km\,s^{-1}}$. As an example, Figs. 3.19 and 3.20 show the histograms of the not saturated version with $v_\mathrm{p} = 10\,\mathrm{km\,s^{-1}}$ for each transition, fitted with one and two components, respectively. Histograms of the fits of further gas velocities and of the saturated versions are shown in A.4.

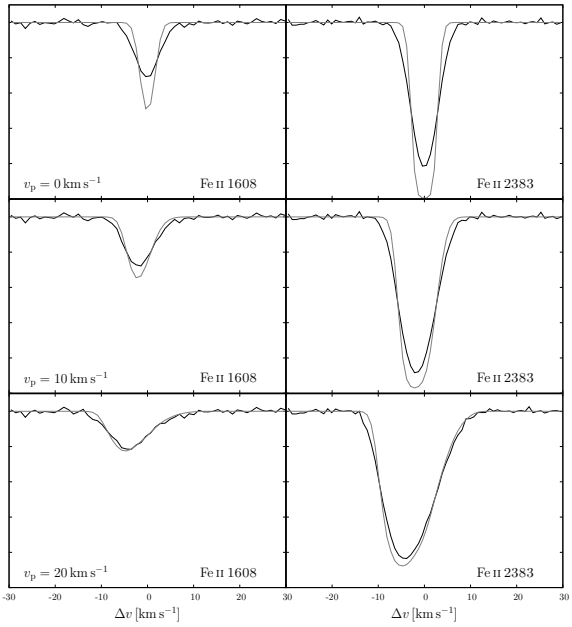

Figure 3.17: Simulated spectra of an absorber with an underlying velocity field according to Fig. 3.16 with $N_1 = 13.0$. The peak velocities are $v_\mathrm{p} = 0\,\mathrm{km\,s^{-1}}$, $v_\mathrm{p} = 10\,\mathrm{km\,s^{-1}}$ and $v_\mathrm{p} = 20\,\mathrm{km\,s^{-1}}$. The different curves show the flux before and after convolution with the instrument profile.

Table 3.3 shows the averaged mimicked α variation for gas velocities from $v_\mathrm{p} = 0\,\mathrm{km\,s^{-1}}$ to $v_\mathrm{p} = 20\,\mathrm{km\,s^{-1}}$. Each is fitted with up to four components. The lowest velocity shifts are in this case achieved by using two or three component fits. There are a few cases where additional components lead to a lower precision in line positioning. This can happen when the additional components fit line distortions of the stronger transitions that are created by noise.

The χ^2 value varies very little with the number of components. For small asymmetries it is not possible to determine the best number of components with this procedure. Better methods are described in Sects. 3.4.4 and 3.4.5. When the asymmetry cannot be seen by eye and adding further components does not decrease the χ^2 value, a one component fit would naturally be used. The corresponding velocity shifts between Fe II 1608 and the other transitions are shown in Table 3.4.

For the smallest simulated peak velocity $v_\mathrm{p} = 5\,\mathrm{km\,s^{-1}}$ the best number of fitting components

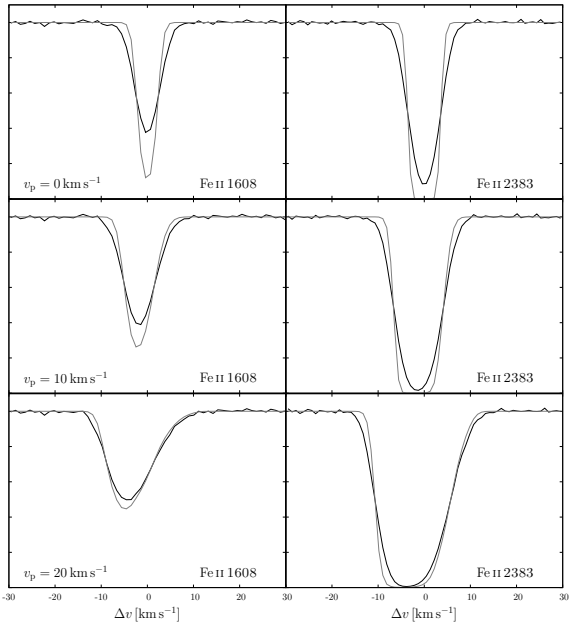

Figure 3.18: Simulated spectra of an absorber with an underlying velocity field according to Fig. 3.16 with $N_2 = 13.5$. The peak velocities are $v_\mathrm{p} = 0\,\mathrm{km\,s^{-1}}$, $v_\mathrm{p} = 10\,\mathrm{km\,s^{-1}}$ and $v_\mathrm{p} = 20\,\mathrm{km\,s^{-1}}$. The different curves show the flux before and after convolution with the instrument profile. The stronger Fe II transitions are unresolved saturated.

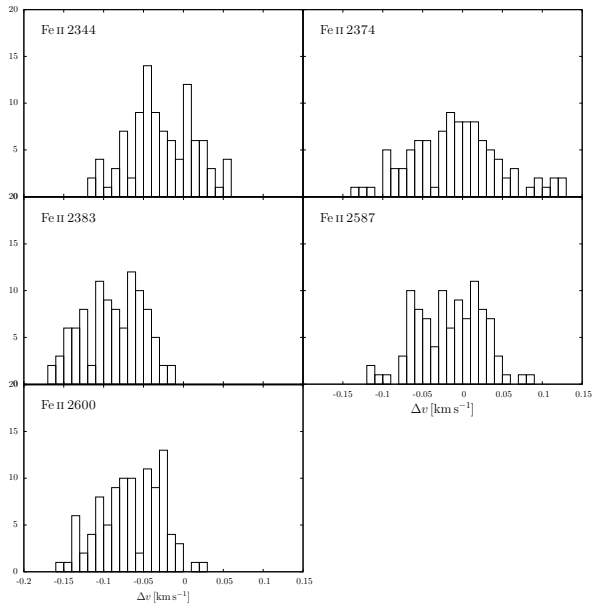

Figure 3.19: Histograms of apparent velocity shifts relative to Fe II 1608 of simulated lines with an underlying velocity field with peak velocity $v_\mathrm{p} = 10\,\mathrm{km\,s^{-1}}$. One-component fit of 100 realisations with random noise.

could not be determined by the χ^2 value alone. Fitting one component results in a shift of $\Delta v \approx 0.1\,\mathrm{km\,s^{-1}}$ between the stronger and the weaker transitions. Using all transitions in a regression analysis an average α variation of $\Delta\alpha/\alpha = (-0.31 \pm 0.17) \cdot 10^{-5}$ is mimicked, comparing the positions of Fe II 1608 and Fe II 2374 gives $\Delta\alpha/\alpha = (-0.03 \pm 0.18) \cdot 10^{-5}$.

3.4.3 Changes of the instrument profile throughout the spectra

If the FWHM of the instrument profile fluctuates over the spectrum, a correct line decomposition is hindered. For symmetric one component lines only the Doppler parameters b and the column densities N should be affected by this. For asymmetric lines, caused by line blends or a velocity substructure, theses values are correlated with the line positions and thus could cause line shifts that might wrongly be interpreted as a variation of constants.

To quantify this effect, artificial spectra were created with different resolving powers. To exclude other potential sources of line position shifts, only a single transition was used in this analysis. A blended feature consisting of two components like in sect. 3.2.1 was simulated with $N_1 = 13.0$, $b_1 = 2\,\mathrm{km\,s^{-1}}$, $N_2 = 12.5$, $b_2 = 4\,\mathrm{km\,s^{-1}}$, and a separation between the components of $\Delta v = 4\,\mathrm{km\,s^{-1}}$. Furthermore a velocity field like in sect. 3.4.2 with $v_p = 10\,\mathrm{km\,s^{-1}}$ was simulated. The latter was fitted as a blend of two components. Each spectrum was simulated with a signal to noise ratio of $S/N = 100$. The same transition was fitted with in spectra with different resolving powers. In each case one transition was simulated with $R = 55\,000$, the second with the resolving power ranging from $R = 45\,000$ to $R = 65\,000$. All fits were done assuming a resolving power of $R = 55\,000$ for both lines. Column densities b, Doppler parameters N, and separation between the components were fitted simultaneously, while the line positions were fitted individually. 100 realisations with random noise were fitted in each case. Figure 3.21 shows the resulting

Table 3.3: Mimicked α variation and χ^2 values for simulated spectra with an underlying velocity field.

	$v_\mathrm{p} = 0\,\mathrm{km\,s^{-1}}$		$v_\mathrm{p} = 5\,\mathrm{km\,s^{-1}}$		$v_\mathrm{p} = 10\,\mathrm{km\,s^{-1}}$		$v_\mathrm{p} = 15\,\mathrm{km\,s^{-1}}$		$v_\mathrm{p} = 20\,\mathrm{km\,s^{-1}}$	
$\#_\mathrm{c}$	$\Delta\alpha/\alpha\,[10^{-6}]$	χ^2	$\Delta\alpha/\alpha\,[10^{-6}]$	χ^2	$\Delta\alpha/\alpha\,[10^{-6}]$	χ^2	$\Delta\alpha/\alpha\,[10^{-6}]$	χ^2	$\Delta\alpha/\alpha\,[10^{-6}]$	χ^2
1	-0.22 ± 1.50	1.0	-3.11 ± 1.93	1.0	-8.62 ± 2.26	1.1	-9.28 ± 3.00	1.4	-8.79 ± 4.42	1.8
2	-0.46 ± 1.29	1.0	-1.93 ± 2.33	1.0	0.05 ± 1.17	1.0	0.20 ± 2.32	1.0	-0.49 ± 3.10	1.0
3	0.14 ± 1.96	1.0	0.19 ± 1.89	1.0	0.49 ± 1.74	1.0	0.04 ± 2.32	1.0	-0.56 ± 2.92	1.0
4	1.19 ± 3.08	1.0	0.36 ± 2.30	1.0	0.52 ± 2.17	1.0	0.05 ± 2.50	1.0	-0.50 ± 2.95	1.0
1	-0.04 ± 0.31	1.0	-2.57 ± 0.42	1.0	-14.26 ± 1.66	1.4	-26.38 ± 2.24	5.6	-26.11 ± 1.98	15.3
2	-0.11 ± 0.33	1.0	-0.49 ± 1.14	1.0	0.31 ± 0.37	1.0	0.54 ± 0.42	1.1	0.31 ± 0.63	1.6
3	0.02 ± 0.63	1.0	-0.13 ± 0.76	1.0	-0.12 ± 01.01	1.0	0.02 ± 0.42	1.0	0.12 ± 0.64	1.0
4	0.05 ± 0.53	1.0	0.06 ± 0.80	1.0	0.00 ± 0.54	1.0	0.02 ± 0.42	1.0	0.10 ± 0.68	1.0

The first four rows show the results for $N_1 = 13.0$ and the last four rows for $N_2 = 13.5$. Simulated spectra with peak gas velocities from $v_\mathrm{p} = 0\mathrm{km\,s^{-1}}$ to $v_\mathrm{p} = 20\mathrm{km\,s^{-1}}$ were fitted with up to four components. Results are averaged over 100 fits with random noise. The errors represent the spread of the values.

Table 3.4: Velocity shifts between transitions for asymmetric lines with an underlying velocity field.

$v_\mathrm{p}\,[\mathrm{km\,s^{-1}}]$	$\Delta v_{2344}\,[\mathrm{km\,s^{-1}}]$	$\Delta v_{2374}\,[\mathrm{km\,s^{-1}}]$	$\Delta v_{2383}\,[\mathrm{km\,s^{-1}}]$	$\Delta v_{2587}\,[\mathrm{km\,s^{-1}}]$	$\Delta v_{2600}\,[\mathrm{km\,s^{-1}}]$
0	0.01 ± 0.04	0.01 ± 0.06	0.01 ± 0.04	0.01 ± 0.05	0.01 ± 0.04
5	0.02 ± 0.05	0.00 ± 0.07	0.05 ± 0.04	0.01 ± 0.05	0.04 ± 0.04
10	0.02 ± 0.06	-0.02 ± 0.08	0.11 ± 0.06	0.01 ± 0.06	0.09 ± 0.06
15	0.03 ± 0.08	0.01 ± 0.11	0.13 ± 0.08	0.02 ± 0.08	0.10 ± 0.08
20	0.06 ± 0.10	0.02 ± 0.15	0.12 ± 0.10	0.03 ± 0.11	0.11 ± 0.10
0	0.00 ± 0.01	0.00 ± 0.02	0.00 ± 0.01	0.00 ± 0.01	0.00 ± 0.01
5	0.03 ± 0.01	-0.01 ± 0.02	0.09 ± 0.01	0.02 ± 0.01	0.08 ± 0.01
10	0.10 ± 0.01	0.01 ± 0.02	0.36 ± 0.01	0.05 ± 0.01	0.30 ± 0.01
15	0.10 ± 0.01	0.01 ± 0.02	0.50 ± 0.01	0.05 ± 0.02	0.33 ± 0.01
20	0.09 ± 0.02	0.01 ± 0.03	0.36 ± 0.10	0.04 ± 0.02	0.28 ± 0.02

The first four rows show the results for $N_1 = 13.0$ and the last four rows for $N_2 = 13.5$. Column 1 shows the peak velocity v_p of the velocity field, Cols. two to six the velocity shifts between the stated transition and Fe II 1608. A one-component fit is used. Results are averaged over 100 fits with random noise. The errors represent the spread of the values.

apparent position shifts between the two lines for the simple line blend version. The error given in the plot represents the spread of the results.

For the simple line blend as well as the velocity field profiles, a velocity shift of up to $|\Delta v| \sim 0.15\,\mathrm{km\,s^{-1}}$ was measured. The value depends strongly on the line composition. A change of the resolving power of about 20% as in these simulations has a strong influence on all fit parameters. For transitions with similar strengths this can be tested by adding the FWHM of the instrument profile as another fit parameter. For transitions with different strengths a possible fluctuation of the instrument profile could not be discerned from other sources of line distortion like unresolved saturation.

3.4.4 Line shift analysis

Wavelength calibration errors and unresolved substructure can cause position shifts between different transitions, that could be misinterpreted as a variation of constants. It is therefore important to determine the cause of measured line position shifts. For this task it is helpful to look for position shifts between all transitions, especially Fe II 2383 and Fe II 2600. Different sources that cause shifts between the lines will be discernible by comparing the shifts to different parameters. Figure 3.22

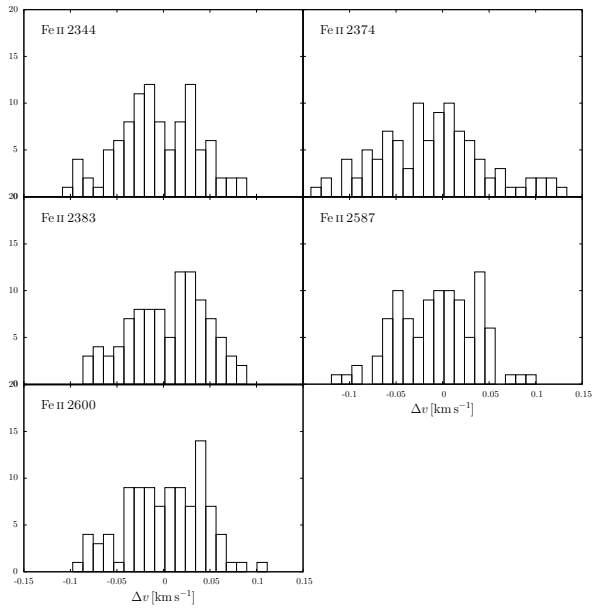

Figure 3.20: As in Fig. 3.19. Histograms of simulated lines with underlying velocity field with $v_\mathrm{p} = 10\,\mathrm{km\,s^{-1}}$. Two-component fit of 100 realisations with random noise.

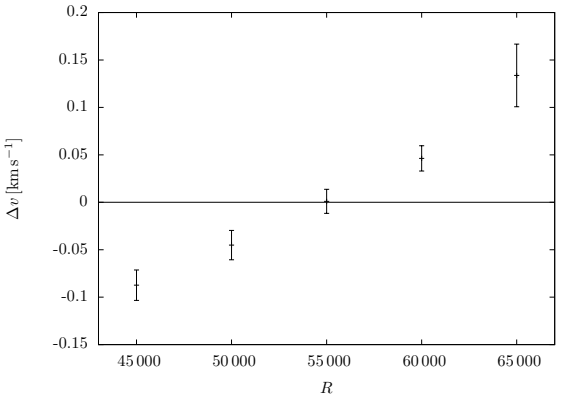

Figure 3.21: Position shifts between two lines with identical parameters, simulated with different resolving powers. One line was always simulated with $R = 55\,000$, the abscissa shows the resolution of the other line.

(top right) shows positions of lines over the transition strength $f\lambda_0$ for simulated spectra created as in 3.4.2 with a peak velocity of $v_p = 10\,\mathrm{km\,s^{-1}}$. The nearly linear correlation of line position and transition strength indicates a problem with decomposition. As a comparison, in Fig. 3.22 (middle right) the same information is shown for a symmetric feature with an artificial α variation of $\Delta\alpha/\alpha = 0.5 \cdot 10^{-5}$. A combination of both effects is shown in Fig. 3.22 (bottom right). Analysing this setting with a regression analysis would result in an apparent α variation of $\Delta\alpha/\alpha = (0.23 \pm 0.17) \cdot 10^{-5}$.

In the left column of Fig. 3.22 the same line positions are plotted over the sensitivity coefficient Q. Since the strong transitions (Fe II 2383 and Fe II 2600) have the same sensitivities, position shifts between these two lines cannot be created by an α variation. In principle, the difference between shifts caused by an α variation and those created by an incorrect line decomposition can thus be distinguished. Assuming a linear correlation between redshift z and transition strength $f\lambda_0$, the strong lines can be used to correct the positions of the other transitions by shifting them according to a straight line fitted through the positions of Fe II 2383 and Fe II 2600 (see Fig. 3.22 (top)). Applying the correction to the setting shown in 3.22 (bottom) would result in $\Delta\alpha/\alpha = (0.41 \pm 0.17) \cdot 10^{-5}$ using all transitions in a regression analysis and $\Delta\alpha/\alpha = (0.46 \pm 0.17) \cdot 10^{-5}$ when line positions of Fe II 1608 and Fe II 2374 are compared. Generally, the $z - f\lambda_0$ relation will not be exactly linear. With the data quality available, this procedure will bring no significant improvement. Simply using the weak transitions, without the correction, gives in this case $\Delta\alpha/\alpha = (0.45 \pm 0.17) \cdot 10^{-5}$. If Fe II 2374 or Fe II 2587 are not available or not usable for other reasons, the systematic error introduced by an $z - f\lambda_0$ dependence can be reduced significantly with this method. For a successful analysis of the system, it is necessary to identify the cause of all measured position shifts. When the position of a transition can not be explained by an α variation or line decomposition problems, e.g. for transitions with similar strengths, the most probable explanation would be wavelength calibration errors.

3.4.5 Bisector analysis

By directly measuring the symmetry of a line, it is possible to look for unresolved line structure. There are several ways to create a measure of the asym-

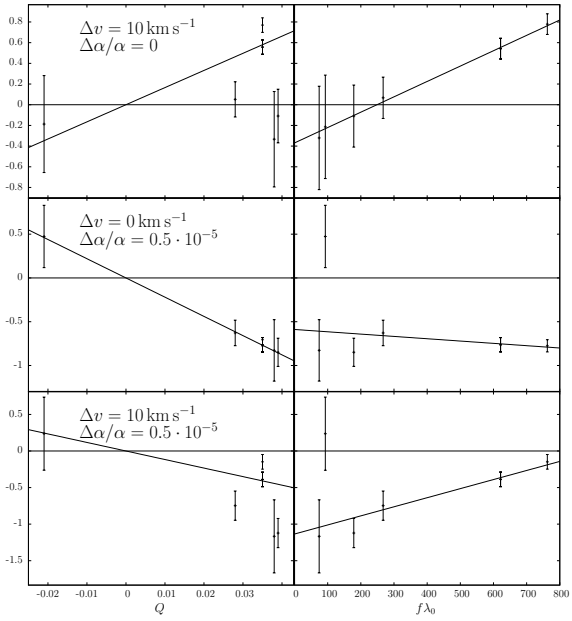

Figure 3.22: Redshift z over sensitivity coefficient Q and transition strength $f\lambda_0$ for an asymmetric line with underlying velocity field with peak velocity $v_\mathrm{p} = 10\,\mathrm{km\,s^{-1}}$ (top), a symmetric line with artificial α variation of $\Delta\alpha/\alpha = 0.5 \cdot 10^{-5}$ (middle), and an asymmetric line with $v_\mathrm{p} = 10\,\mathrm{km\,s^{-1}}$ and $\Delta\alpha/\alpha = 0.5 \cdot 10^{-5}$ (bottom).

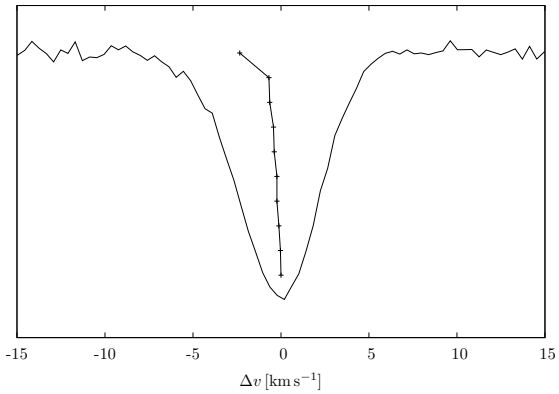

Figure 3.23: Example of bisector of a slightly asymmetric line with noise.

metry of an absorption line. The bisector method, originally developed in solar physics for detecting velocity fields in the atmospheres of late-type stars (e.g. Dravins (1982)), has the advantage that it can identify not only the magnitude of the asymmetry but also its general shape. Figure 3.23 shows an example of a bisector calculation for a slightly asymmetric line with noise. For a given flux F, the central wavelength $\lambda_\mathrm{c} = (\lambda_2 - \lambda_1)/2$ between the two flanks of the line profile is calculated. The bisector is a curve crossing the points $(\lambda_{\mathrm{c,i}},F_\mathrm{i})$. For a perfectly symmetric line, the bisector is a vertical straight line at the position of the line centre from the lowest flux of the line up to the continuum.

The bisectors are parametrised from the minimum of the profile to the continuum. Hereafter the lowest flux value of the lines is referred to as $0f$, while the continuum is referred to as $1f$. For the lowest value ($0f$) the determination of the bisector value is strongly affected by noise, especially for weak or saturated lines. Therefore the bisector value at $0.1f$ is used as a basis for a comparison of different transitions. Fig. 3.24 shows bisectors of simulated line profiles with an underlying velocity field as in sect. 3.4.2. From left to right the plot shows bisectors of lines with gas velocities of $v_p = 5\,\mathrm{km\,s^{-1}}$ to $v_p = 20\,\mathrm{km\,s^{-1}}$. For each velocity the six abundant Fe II transitions were simulated. The bisector of each transition is slightly different. The bisectors of the weakest transitions (Fe II 2374) are the steepest on the left side of each velocity setup while the strongest transition Fe II 2382 is the flattest on the right side.

The results of line position fits depend on a correct decomposition of the line profile. As was shown in sect. 3.4.2, the χ^2 method can be insufficient to determine the best number of fit components. The bisector can be used to compare the symmetry of the involved lines and thus reveal potential decomposition problems and other error sources. Differences of bisectors of different transitions are small, so that they are, in nearly all cases, blurred by noise. Finding considerable differences between bisectors of different transitions of the same ion would usually mean that some of the lines are distorted by other sources and should not be used. There is another way the bisector method can be used in this case. Even when a line looks symmetric and a one-component fit is favoured, there can be a measurable deviation from a truly symmetric line. By studying the bisector, these deviations can be detected and the potential error can be estimated.

Figure 3.25 shows position shifts over the total

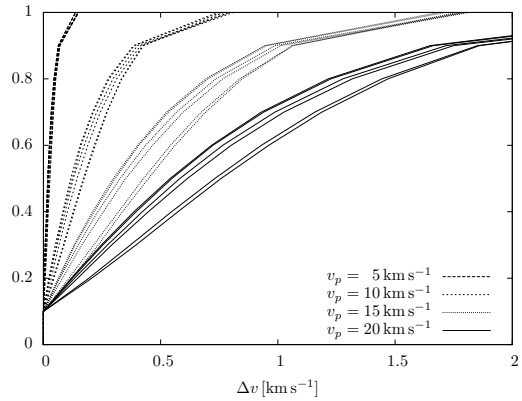

Figure 3.24: Bisectors of Fe II 1608, Fe II 2344, Fe II 2374, Fe II 2383, Fe II 2587, and Fe II 2600. Macroscopic velocities of $v_\mathrm{p} = 5\,\mathrm{km\,s^{-1}}$, $10\,\mathrm{km\,s^{-1}}$, $15\,\mathrm{km\,s^{-1}}$, and $20\,\mathrm{km\,s^{-1}}$ are plotted.

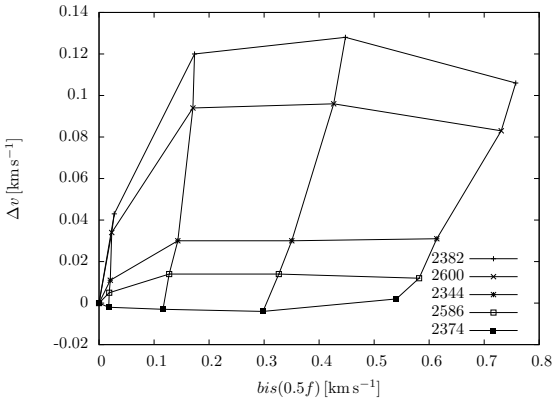

Figure 3.25: Velocity shifts over bisector at half maximum for different Fe II transitions. The vertical lines show from left to right gas velocities of $v_\mathrm{p} = 5\,\mathrm{km\,s^{-1}}$, $v_\mathrm{p} = 10\,\mathrm{km\,s^{-1}}$, $v_\mathrm{p} = 15\,\mathrm{km\,s^{-1}}$, and $v_\mathrm{p} = 20\,\mathrm{km\,s^{-1}}$.

bisector at half maximum, plotted for Fe II 2344, Fe II 2374, Fe II 2383, Fe II 2587, and Fe II 2600 in comparison to Fe II 1608. The line profiles were simulated as in sect. 3.4.2. Each vertical line represents a model with gas velocities of $v_p = 5\,\mathrm{km\,s^{-1}}$, $10\,\mathrm{km\,s^{-1}}$, $15\,\mathrm{km\,s^{-1}}$, and $v_p = 20\,\mathrm{km\,s^{-1}}$, seen from left to right. The main increase of position offsets comes at small asymmetries of $\Delta v \lesssim 0.2\,\mathrm{km\,s^{-1}}$ at $0.5f$. The possibility of finding asymmetries on this scale with the bisector method depends on the data quality. Figure 3.26 shows the accuracy of bisector measurements at $0.5f$ for different resolutions R and signal to noise ratios S/N. σ is the spread of bisector measurements of 100 realisations with noise for the given data quality. Though total bisectors with $\mathrm{bis}(0.5f) \sim 0.2\,\mathrm{km\,s^{-1}}$ would be detectable with the data quality currently available, differences between bisectors in different transitions that indicate unresolved saturation would need very high quality data with $R \gtrsim 80\,000$ and $S/N \gtrsim 140$. Upcoming instruments could reach a data quality that allow a detection of differential bisectors.

Figure 3.27 shows the bisectors of Fe II 2383 and Mg II 2804 of the spectra shown in Fig. 3.14 (bottom) for different combinations of resolution and signal to noise ratio. In light grey the 1σ statistical error is given. The resolving power has a strong influence on the detectability of differences in line shapes. Just the highest data quality version ($R = 65\,000$, $S/N = 100$) allows a clear discrimination between the line shapes.

The highest data quality available today would be required to detect deviations from symmetry as a possible source of position shifts of up to a few hundred meters per second. The assumption that these effects will average to zero when a sufficiently large sample is used, is only valid if no systematic effects exist that bias the ionisation stratification of the interstellar medium. In any case, it has to be taken into account that the systematical error in each system is up to 10 times higher than the statistical error when calculating the total uncertainty.

.

3.4.6 Isotope abundances

Mg II has three stable isotopes, with laboratory wavelengths $\lambda_0(^{26}\mathrm{Mg\,II}) = 2796.3470\,\text{Å}$, $\lambda_0(^{25}\mathrm{Mg\,II}) = 2796.3491\,\text{Å}$, and $\lambda_0(^{24}\mathrm{Mg\,II}) = 2796.3551\,\text{Å}$(Morton 2003). The combined Mg II laboratory wavelength used in this work (Table 2.1) was measured with a solar ratio of isotope abundances (^{24}Mg II $\sim 78.99\%$, ^{25}Mg II $\sim 10.00\%$, ^{26}Mg II $\sim 11.01\%$). A relative change in abundances of the different isotopes would cause the total laboratory wavelength to shift. Thus a variation of constants could be mimicked by an isotope abun-

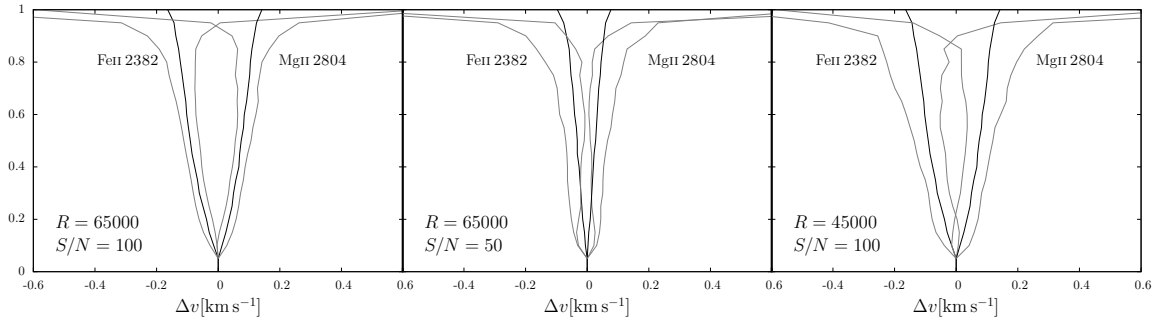

Figure 3.27: Bisector of Fe II 2383 and Mg II 2804 for lines from Fig. 3.14 (bottom). The grey lines show the corresponding statistical error. Resolution ans signal to noise ratio of the simulated line profiles are indicated in the plot.

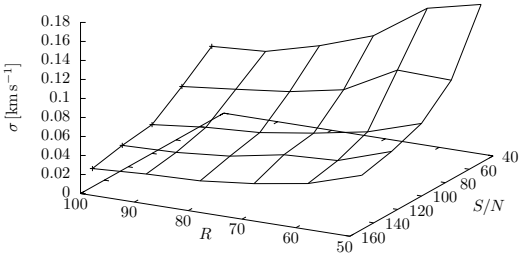

Figure 3.26: Accuracy σ of bisector measurements at half maximum over resolution R and signal to noise ratio S/N.

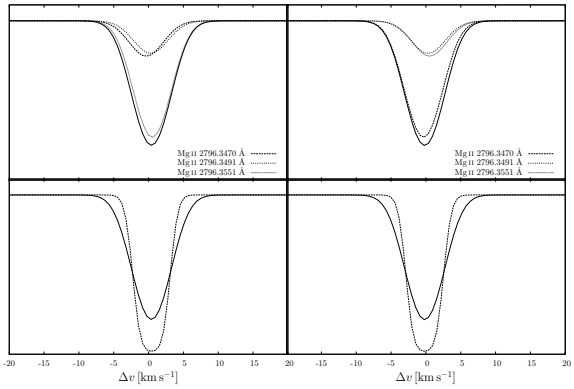

Figure 3.28: Simulated spectra of Mg II 2796 for solar (l) and changed (r) abundances. The solid curves show the final lines. The top row shows the contribution of the single isotopes to the lines, the bottom row shows the line before and after convolution with the instrument profile.

dance ratio change over space or time when Mg II is used as anchor line. We note that a position shift of the Mg II lines due to isotope abundances is expected to be on a much smaller scale ($\sim 50\,\mathrm{m\,s^{-1}}$) than position shifts due to other sources like an ionisation stratification or unresolved substructure.

Assuming symmetric one-component lines, a change in isotope abundances could be measured by studying the line shape with the bisector method. Figure 3.28 shows simulated spectra of Mg II 2797 for solar and changed abundances. The changed abundances were chosen to have the strongest measurable effect on a bisector analysis by interchanging the abundances of the ^{24}Mg II and the ^{26}Mg II isotope (^{24}Mg II $\sim$ 11.01%, ^{25}Mg II $\sim$ 10.00%, ^{26}Mg II $\sim$ 78.99%). The figure shows the contribution of the single isotopes to the final line (top) and the line before and after convolution with the instrument profile (bottom).

Figure 3.29 shows the corresponding bisectors (a: solar, b: changed) for different resolving powers $R_1 = 50\,000$, $R_2 = 75\,000$, and $R_3 = 100\,000$. The grey curves show the bisectors of the flux prior to convolution with the instrument profile. Though the distance between the ^{24}Mg II and the ^{26}Mg II is $\Delta v \approx 870\,\mathrm{m\,s^{-1}}$, the distortion of the line shape is on a much smaller scale; the total shape is just a small correction to the shape of the

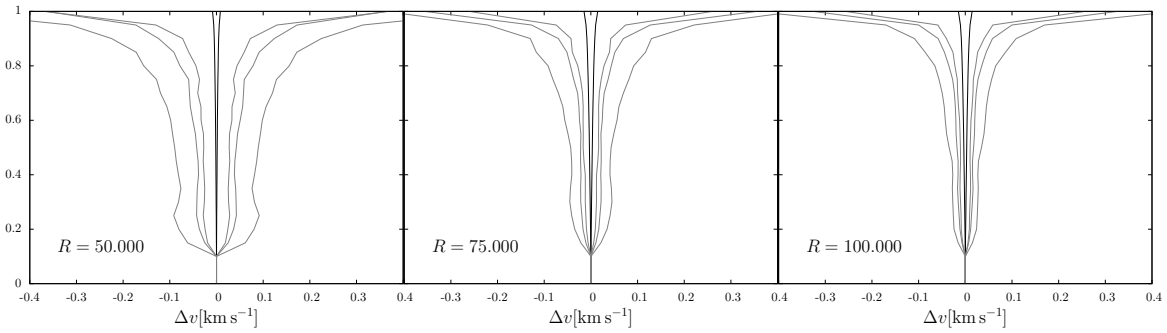

Figure 3.30: Bisectors of simulated spectra of Mg II 2796 for solar and changed abundances for different values of resolving power R. The light grey curves show the 1σ spread of a sample of 100 simulated lines with random noise with different values of signal to noise ratio $S/N_1 = 50$, $S/N_2 = 100$, and $S/N_3 = 150$.

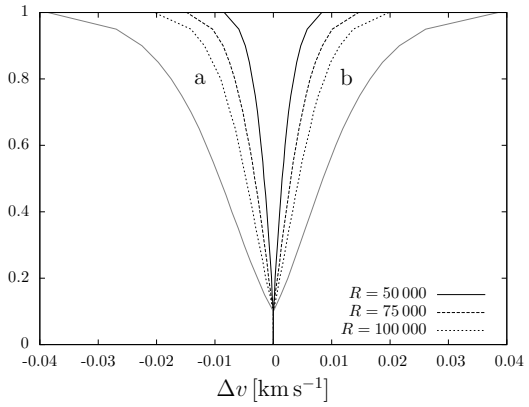

Figure 3.29: Bisectors of Mg II 2796 for solar (a) and changed (b) isotope abundances for resolutions of $R = 50\,000$, $R = 75\,000$, and $R = 100\,000$. The solid grey lines show the corresponding bisectors calculated prior convolution with the instrument profile.

strongest isotope. Furthermore the shape of the line is smoothed by the instrument profile. With increasing resolving power of the instrument the effect of changed isotope abundances on the bisector increases.

The shape of the bisector can only give an indication of the real isotope abundances. Figure A.11 shows a grid of bisectors for every possible combination of isotope abundances of Mg II 2796 in steps of 10%. The lines were simulated with a combined column density of $N = 12.5$ and a Doppler parameter for each isotope of $b = 2\,\mathrm{km\,s^{-1}}$ without noise. The resolving power in this calculation was $R = 45\,000$, corresponding to the quality of a data used in sect. 4.6.2. Many combinations of isotope abundances give very similar bisectors. A strong reduction of the highly abundant ^{24}Mg II should be detectable nevertheless, provided that the data quality is high enough.

To test the possibility to find the isotope abundance ratio observationally, a set of simulation was done with different values of resolving power $R_1 = 50\,000$, $R_2 = 75\,000$, and $R_3 = 100\,000$ and signal to noise ratio $S/N_1 = 50$, $S/N_2 = 100$, and $S/N_3 = 150$. The combined column density of all three isotopes was $N = 12.5$ and the Doppler parameter was $b = 1.5\,\mathrm{km\,s^{-1}}$. This configuration gives strong unsaturated line profiles for Mg II 2796. Figure 3.30 shows the bisectors for solar and changed abundances. In grey the standard deviation from the average of the bisector calculation of 100 realisations with random noise is shown. Even with a very high data quality ($R = 100\,000$, $S/N = 150$) the isotope ratio could not be determined with the bisector method in a single measurement. The only possibility is to use many systems in a statistical analysis. If a similar data quality is assumed for all systems and the spread is approximately normal distributed, the variance of the weighted mean simplifies to $\bar{\sigma}^2 = \sigma_0^2/n$, where σ_0 is the measurement uncertainty and n is the number of measurements. Table 3.5 shows the number of ideal systems that would be necessary for the given data quality to get a 1σ detection of a change in isotope abundances as given in Fig. 3.28 when the standard variation from the previous simulations is used as the measurement error. The number is cal-

Table 3.5: Number of systems required to get a 1σ detection of isotope abundances with the bisector method under ideal conditions for different data qualities.

R	Number of systems		
	$S/N = 50$	$S/N = 100$	$S/N = 150$
50 000	1719	370	138
75 000	164	30	12
100 000	55	10	5

culated so that the accuracy of the weighted mean of all bisectors is smaller than the bisector of the simulated solar isotope abundance line. The numbers in table 3.5 are for bisectors in the upper region of the line profile (between $0.6f$ and $0.8f$). In this region the bisector differences are strongest without being too much affected by noise. While the number of required systems is high for the data quality available today, the next generation of telescopes will bring a significant improvement.

In this section only statistical aspects have been considered. When the line shapes are distorted by unresolved blends or a velocity substructure, the number of required systems could increase considerably or the method might not be applicable at all. For further analysis the method was used on real data to make a comparison of simulated predictions and real data measurements (see sect. 4.6.2).

Chapter 4

Data analysis

The number of systems used for the SIDAM method is quite limited and so each single system demands a detailed analysis to exclude systematical errors. The quality of the data is in most cases lower than that in the simulations, resulting in a lower accuracy. The bisector analysis will only be possible in special cases.

Each system was studied carefully to detect potential sources for position shifts that could mimic an α variation. To detect possible decomposition problems, for each system a $z - f\lambda_0$ diagram is plotted. Additionally, for single isolated lines, bisectors are plotted. The minimising algorithm based on an evolution strategy (Quast et al. 2005) used for fitting the data reduces the danger of finding only local χ^2 minima. Each system was fitted several times with an increasing number of components until the minimum χ^2 value change was less than 10%. In all cases the difference between the resulting α variation calculations for the favoured number of components and the next higher number was within the 1σ error limit. In the following sections only the results for the favoured number of fit components is given. Instead of calculating an error of the placement of each single component, the 1σ confidence limit was calculated for the whole system with the χ^2 method. To account for possible fluctuations of the instrument profile throughout the spectra, the resolving power was fitted for transitions with similar strengths. If significant differences to the assumed resolution was measured, an α variation calculation with the fitted resolution was made. In all cases the resulting $\Delta\alpha/\alpha$ values did not differ more than 1σ from each other.

When calculating the apparent α variation, different methods were used. Since line shifts due to wavelength calibration errors are hard to detect, the selection of suitable lines is mainly done by studying the bisector (Sect 3.4.5) and the $z - f\lambda_0$ diagram (sect. 3.4.4). For comparison, the results of using all available transitions in a regression analysis and just two line positions of transitions with similar strengths, are given separately in each case.

4.1 HE0515-4414 - A detailed analysis

The bright quasar HE0515-4414, at an emission redshift of $z_{\rm em} = 1.71$, has a strong DLA system at $z = 1.15$. This system has received much attention in different fields and was also used for α variation analyses in the past (Quast et al. 2004; Levshakov et al. 2005). We re-analysed the system with special attention towards line profiles and the precision of line position measurements. The data was taken in 2000/2001 with the UVES spectrograph at the VLT. Table C.1 shows the best fit parameters for all observable metal lines of this system. For this table the line positions of each transition were fitted simultaneously for each ion. Components that could be associated in different ions ($\Delta v \lesssim 5{\rm km\,s^{-1}}$) are labelled with a number.

4.1.1 SIDAM

The $z = 1.15$ system is quite complex and has many blended and saturated lines. The system was divided into six subsystems by parts of well defined continuum without visible absorption (SS1 to SS6). Table C.1 shows the best fit parameters for a simultaneous 34 component fit. Component 8 and 15

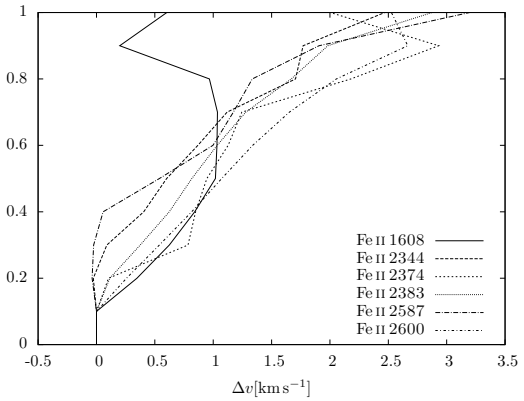

Figure 4.1: Bisector of all visible Fe II transitions of the z=1.1491 system in HE0515-4410.

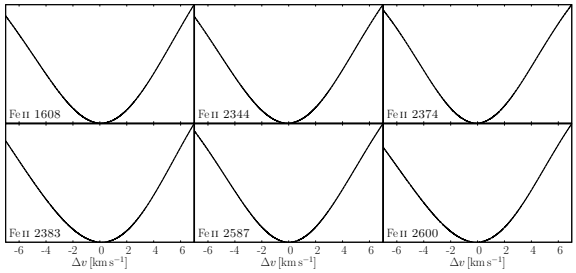

Figure 4.2: χ^2 curves of SS3 of the $z = 1.15$ system in HE0515-4410.

are not used in the further analysis because they are isolated from other components and too weak to be seen in Fe II 1608.

Because there is not one symmetric unblended line in the whole system, the feature at $z = 1.1491$ (SS3) is the most promising. It is not blended with neighbouring lines, not obviously saturated, and strong enough to be seen in the weaker transitions. The asymmetry of this feature was considered to be the result of a narrow blend of two components in past analyses. The statistical error for the fit is only valid if the deconvolution is correct. Since the true origin of the line shape cannot be determined indubitably, it may well be that at least the error is significantly underestimated. Assuming the shape of the line is created by a blend of two blended Doppler profiles there can still be problems when unresolved saturation is present in the stronger transitions. Carefully studying the position of each line and the corresponding bisector is necessary to identify possible error sources. Even though it is safer just to use transitions of similar strength, a detailed analysis of the whole system can be instructing. Table 4.1 shows the fit parameters for this system for a two-component fit of all available transitions, a two-component fit of just the weak Fe II 1608 and Fe II 2374 transitions, and finally a three-component fit of all transitions. When doing a simultaneous fit of all transitions, the result is mainly influenced by the shape of the stronger components because of their higher influence on the total χ^2. Table 4.1 shows that the fit parameters are similar when fitting just the weak transitions, indicating no strong alteration of the line shape of the stronger transitions.

Fig. 4.2 shows the χ^2 curves for all transitions of this subsystem. The central position at $\Delta v = 0\,\mathrm{km\,s^{-1}}$ corresponds to the average position of all six transitions. For the 1σ positioning error the value at $\chi^2_{\mathrm{min}} \pm 1$ was used. According to the χ^2 distribution, the curve is parabolic near its minimum. For all data fits in this work the χ^2 curves were inspected to check for problems with the fit (see e.g. sect. 3.2.2).

Fig. 4.1 shows the bisectors of all detectable Fe II transitions. The deviation of Fe II 1608 from the bisectors of the other Fe II transitions in the upper part can be explained by noise (see Fig. B.1). Figure 4.3 shows the line shift analysis for this feature. The positions of the strong Fe II 2383 and Fe II 2600 are separated by $\Delta v = 0.23\,\mathrm{km\,s^{-1}}$ ($\sim 5\sigma$), indicating an underestimation of the positioning error. No strong correlation of line position and transition strength can be seen. Possible explanations for this discrepancy could be wavelength calibration problems or unresolved saturation of Fe II 2383. Using all transitions in a regression analysis gives an α variation of $\Delta\alpha/\alpha = (0.0 \pm 1.0) \cdot 10^{-5}$, comparing line positions of Fe II 1608 with Fe II 2374 gives $\Delta\alpha/\alpha = (0.3 \pm 1.0) \cdot 10^{-5}$. The error is the confidence interval of the regression analysis. The usage of all transitions does not increase the accuracy of the result due to the larger scatter of line positions, in this case primarily created by the offset between Fe II 2383 and Fe II 2600. Using a three component fit gives nearly the same result of $\Delta\alpha/\alpha = (0.1 \pm 1.0) \cdot 10^{-5}$ for all transitions and $\Delta\alpha/\alpha = (0.3 \pm 1.0) \cdot 10^{-5}$ for Fe II 1608 and Fe II 2374.

Table 4.1: Fit parameters of the $z = 1.1491$ feature for a two-component fit of all transitions, a two-component fit of just Fe II 1608 and Fe II 2374 and a three-component fit of all transitions.

#	z	N	b [km s^{-1}]
20	1.14909	12.60 ± 0.04	1.8 ± 0.2
21	1.14912	12.43 ± 0.06	4.8 ± 0.3
20	1.14908	12.48 ± 0.36	1.0 ± 1.9
21	1.14911	12.52 ± 0.37	4.4 ± 4.2
20	1.14908	12.12 ± 0.45	0.9 ± 0.4
	1.14909	12.40 ± 0.24	1.5 ± 0.5
21	1.14912	12.45 ± 0.04	5.0 ± 0.3

The redshift z is the average of all fitted transitions.

For this part of the system a quite consistent zero result for the α variation could be confirmed. There was no indication of decomposition problems. The offset between Fe II 2383 and Fe II 2600 of $\Delta v = 0.23\,\mathrm{km\,s^{-1}}$. can be used as a measure for the uncertainty of wavelength calibration or of other unaccounted error sources. In this case an accuracy limit of $\Delta\alpha/\alpha \sim 0.7 \cdot 10^{-5}$ can be set for the α variation measurement of a single system in this data set. This is of the same order of magnitude as the statistical error for this system.

The first part of the $z = 1.15$ system (SS1) consists of at least seven components ranging from $z = 1.1469$ to $z = 1.1474$. The line shift analysis shows that all transitions are in good alignment. There is also no significant correlation of line position and transition strength (Fig. 4.3). Using all transitions would give an α variation of $\Delta\alpha/\alpha = (0.2 \pm 2.0) \cdot 10^{-5}$. Just Fe II 2374 in comparison with Fe II 1608 gives $\Delta\alpha/\alpha = (-1.2 \pm 2.0) \cdot 10^{-5}$. This result is compatible with the result from SS3.

SS2 consists of at least five components, ranging from $z = 1.1478$ to $z = 1.1481$. The line shift analysis shows a small slope of the regression line, which is mainly influenced by the small offset between Fe II 2344 and the stronger transitions. There is no strong correlation of position and transition strength (Fig. 4.3). Using all transitions is a regression analysis would give $\Delta\alpha/\alpha = (-1.5 \pm 3.6) \cdot 10^{-5}$ while just Fe II 2374 in comparison with Fe II 1608 gives $\Delta\alpha/\alpha = (-2.1 \pm 4.0) \cdot 10^{-5}$. This result is again compatible with the result of SS1 and SS3.

SS4 is a blend of two resolved components at $z = 1.1495$. It shows a distinctive shift between Fe II 1608 and all other transitions. There is no strong correlation of position shift and transition strength (Fig. 4.3). Using all transition would give a 1.2σ signal of $\Delta\alpha/\alpha = (4.4 \pm 3.6) \cdot 10^{-5}$. Using just Fe II 2374 reduces this value to $\Delta\alpha/\alpha = (4.0 \pm 4.4) \cdot 10^{-5}$. The position of Fe II 1608 is within 1σ of the positions of all other transitions. The signal in the regression analysis comes mainly from the low errors in position fits of the stronger components. This shows a conceptional problem when using the regression analysis. Position shifts between Fe II 2344 with $Q = 0.032$ and the stronger transitions with $Q = 0.036$ can have a big influence on the regression analysis, especially since these transitions will usually have the lowest position fit errors. When all position shifts are exclusively created by an α variation the regression method will give the best results. Since we know that many other effects can create real or apparent position shifts, the results of this approach have to be regarded with care. To circumvent this problem and nevertheless using all transitions, it is possible to use Fe II 1608 in comparison with a weighted mean of all other line positions with an average sensitivity coefficient of $\bar{Q} = 0.0364$. In this case this method would result in $\Delta\alpha/\alpha = (3.2 \pm 3.9) \cdot 10^{-5}$. Nevertheless, using transitions with similar strength is still preferable because of the reduced danger of apparent shifts due to incorrect line decomposition.

SS5 at $z = 1.1498$ is similar in most aspect to SS4. It shows a shift between Fe II 1608 and Fe II 2374 on the one hand and the other transitions on the other hand. A clear correlation of line position and transition strength is not visible (Fig. 4.3). Though the system does not suggest problems due to unresolved saturation, the alignment of Fe II 1608 and Fe II 2374 transitions suggests rather incorrect line decomposition than α variation. A regression of all available transitions would give a 1.3σ signal of $\Delta\alpha/\alpha = (-5.4 \pm 4.1) \cdot 10^{-5}$ while using just the weak transitions gives $\Delta\alpha/\alpha = (-2.5 \pm 4.5) \cdot 10^{-5}$.

The final subsystem (SS6) is composed of at least 14 strongly blended components, ranging from $z = 1.1505$ to $z = 1.1518$, some of which are highly saturated in the stronger transitions. This subsystem shows a 9σ position offset of $\Delta v \sim 0.2$ km s^{-1}

between Fe II 2600 and the other transitions. This value is not higher than the position shifts in the other subsystems and at the level of the general wavelength accuracy estimated in SS3. Nevertheless, using all transitions in a regression analysis would give $\Delta\alpha/\alpha = (0.3 \pm 0.2) \cdot 10^{-5}$ while just the weak transitions give $\Delta\alpha/\alpha = (-0.3 \pm 0.2) \cdot 10^{-5}$.

Additional fits were done to get a combined measure of the whole system. First SS1 to SS5 where combined to a singe entity, including the two isolated weak components 8 and 14. This part of the system shows no apparent saturation. The line shift analysis (Fig. 4.3) shows no strong position shifts, apart from an offset between the strong Fe II 2383 and Fe II 2600 ($\Delta v = 0.19 \mathrm{km\,s^{-1}}$). Using all transitions in a regression analysis gives $\Delta\alpha/\alpha = (-0.1 \pm 0.8) \cdot 10^{-5}$ while using just the weak transitions gives $\Delta\alpha/\alpha = (0.1 \pm 0.9) \cdot 10^{-5}$. In this case using all transitions does not change the result significantly and the decrease in error is also marginal. Calculating a weighted mean of the results of the individual subsystem SS1 to SS5 gives very similar results of $\Delta\alpha/\alpha = (0.0 \pm 0.8) \cdot 10^{-5}$ for the regression analysis and $\Delta\alpha/\alpha = (0.0 \pm 0.9) \cdot 10^{-5}$ for the weak transitions, respectively.

Finally all 34 components were treated as a single system. The line positions are very similar to those of SS6 (Fig. 4.3). Accordingly the resulting α variation calculations give nearly the same results of $\Delta\alpha/\alpha = (0.3 \pm 0.2) \cdot 10^{-5}$ for the regression analysis and $\Delta\alpha/\alpha = (-0.3 \pm 0.2) \cdot 10^{-5}$ using the weak transitions, respectively. The weighted mean of the results of subsystems SS1 to SS6 gives the same numbers. This shows that the total position fit is dominated by the strongest lines. If these lines are also saturated, the danger of an underestimation of the error is high. It is therefore safer to take a more conservative approach and exclude this subsystem.

Table 4.2 shows an overview of the results of this section. We found that the α variation in the $z = 1.15$ system in the quasar HE0515-4410 can be constrained to $|\Delta\alpha/\alpha| < 9\,\mathrm{ppm}$ on a 1σ confidence level. This value is based on the analysis of the combined subsystems SS1 to SS5. Previous analyses of the same data give a more stringent constraint. Quast et al. (2004) used the SIDAM method on the not saturated part of the system. This corresponds to our combined sample of subsystems SS1 to SS5. They set a constraint for a variation of α to $|\Delta\alpha/\alpha| < 2\,\mathrm{ppm}$. Even with a regression analysis of all transitions we could not reproduce this accuracy. A reanalysis of the system by Chand et al. (2006) gave a similar result. Since they used the whole system, including the saturated part, the low statistical error of the result is reproduced in our analysis of the combination of all subsystems (SS1-SS6). They also made a simultaneous fit of the UVES data with higher resolution data obtained with the HARPS spectrograph (Pepe et al. 2002) to compare the line decomposition. Though they found that the higher resolution data requires more components to be added to the system, both decomposition models gave nearly the same α variation measurement results. This indicates that, at least for this system, the simpler line decomposition was as good an approximation of the real line shape as the composition with more components.

Table 4.2: Results of α variation calculations for different parts of the HE0515-4414 $z = 1.15$ system.

System	#	$\Delta\alpha/\alpha_{all}[10^{-5}]$	$\Delta\alpha/\alpha_{weak}[10^{-5}]$
SS1	7	0.2 ± 2.0	-1.2 ± 2.2
SS2	5	-1.5 ± 3.6	-2.1 ± 4.0
SS3	2	0.0 ± 1.0	0.3 ± 1.1
SS4	2	4.4 ± 3.6	4.0 ± 4.4
SS5	2	-5.4 ± 4.1	-2.5 ± 4.5
SS6	14	0.3 ± 0.2	-0.3 ± 0.2
SS1-SS5	20	-0.1 ± 0.8	0.1 ± 0.9
SS1-SS6	34	0.2 ± 0.2	-0.3 ± 0.2

The first column shows the subsystem, the second column shows the number of fitted components, while the third and fourth columns show the resulting α variation for a regression analysis using all transitions and a direct comparison of Fe II 2374 and Fe II 1608, respectively.

4.1.2 Other ions

Next to Fe II, the system has detectable absorption of C IV, Mg I, Mg II, Al II, Al III, Si II, Cr II, Mn II, Fe I, Ni II, and Zn II outside of the Lyman α forest. The two C IV transitions are blended with each other, with Fe II 2600 of a system at $z = 0.28$, and some Lyman α absorption lines, associated with the quasar itself. The position determination is thus very unreliable. The stronger transitions

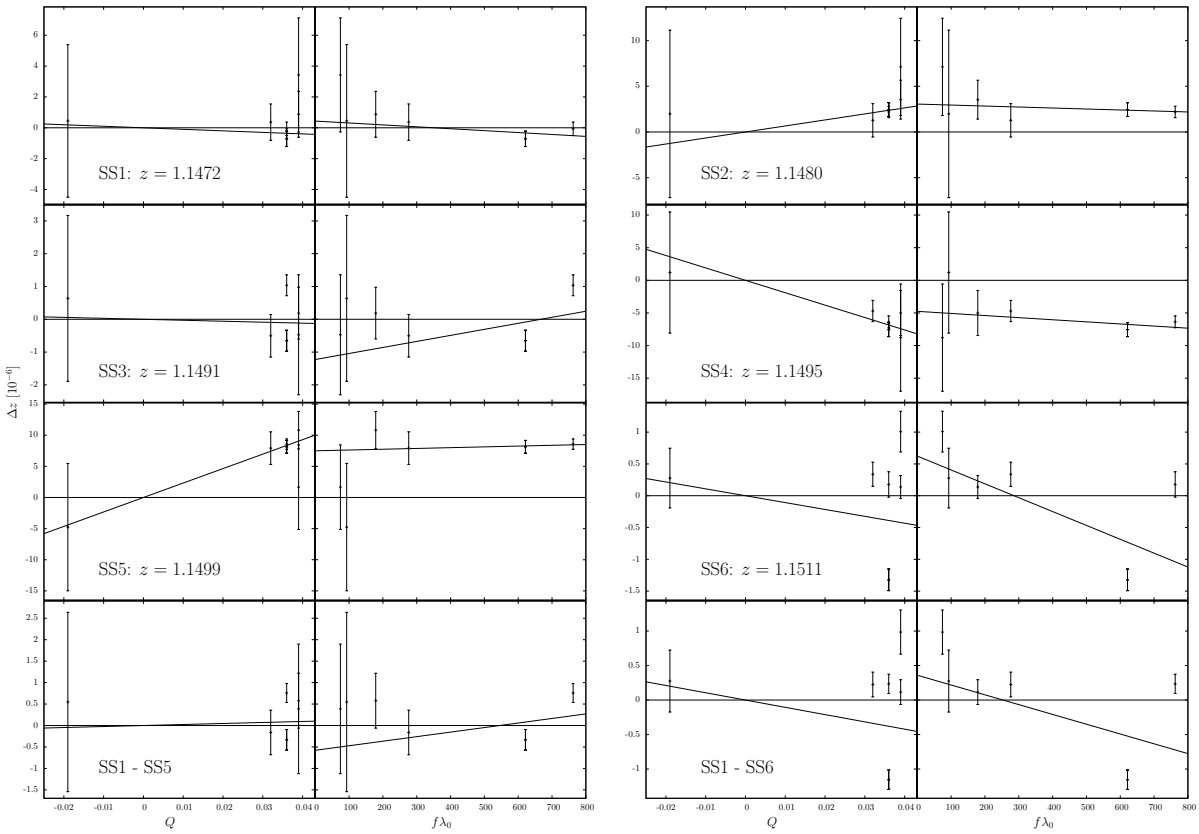

Figure 4.3: Line shift analysis of several parts of the $z = 1.15$ system. Line positions are plotted over sensitivity coefficients Q and transition strengths $f\lambda_0$.

of Si II are all located within the Lyman α forest. Si II 1527 seems to be relatively unaffected by line blends though and has been used together with the weak Si II 1808, the only detectable Si II transitions that is found outside the Lyman α forest, for the line parameter fit in table C.1. Both visible Zn II transitions are blended with other ions of the same absorption system, namely with Mg I 2026 and Cr II 2062. Part of Al III 1863 is blended with Mg II 2804 from a system at $z = 0.43$.

Position shifts between different ions are most likely attributed to the ionisation substructure of the absorbing medium. It is nevertheless instructive to measure the magnitude of such shifts. By comparing line position fits of transitions with the same sensitivity to an α variation, it is possible to trace different error sources. Line positions of transitions of different ions are a measure of a combination of ionisation substructure shifts and error sources like wavelength calibration uncertainties and unresolved substructure. Using only transitions of a single ion circumvents problems with ionisation substructure. When also the transition strength $f\lambda_0$ is similar, the effects of an inaccurate line decomposition or unresolved saturation become small and the only significant error source that is left is wavelength calibration or other unregarded error sources.

Though Fe II lines are far the best choice for the SIDAM method in terms of abundance, sensitivity and typical line strengths, other ions can also be used. The results will generally have a lower precision, depending on sensitivities and line strengths. The biggest sensitivity difference between transitions of the same ion after Fe II ($\Delta Q = 0.055$) has Ni II with $\Delta Q = 0.021$.

The Ni II lines are weak, however all three transitions have a similar strength (see Table 2.1). The

Table 4.3: Redshift z, number of components #, and $\Delta\alpha/\alpha$ for different ions of the HE0515-4414 $z = 1.15$ system.

ion	z	#	$\Delta\alpha/\alpha\,[10^{-5}]$
Fe I	1.1508	2	0.5 ± 6.0
Ni II	1.1508	3	3.8 ± 7.6
Ni II	1.1512	2	11.2 ± 17.3
Zn II	1.1508	4	0.4 ± 2.9

system can be separated into two distinct features, the first at $z = 1.1508$ with three components and the second at $z = 1.1512$ with two components. Because all three transitions have different sensitivity coefficients, a regression analysis is the best procedure for an α variation measurement. The first part of the system gives $\Delta\alpha/\alpha = 3.8 \pm 7.6 \cdot 10^{-5}$ while the second part gives $\Delta\alpha/\alpha = 11.2 \pm 17.3 \cdot 10^{-5}$.

The Zn II feature with $\Delta Q = 0.017$ is also quite weak and both transitions are blended with lines of other ions of the same system. The result of the line position fit has thus to be regarded with care. The relatively low position offset between the two transitions gives $\Delta\alpha/\alpha = 0.4 \pm 2.9 \cdot 10^{-5}$.

The third ion that has transitions with a a sufficient difference in sensitivities is Fe I with $\Delta Q = 0.016$. The two visible transitions differ in strength, so that decomposition errors can affect the line position measurement accuracy. The system at $z = 1.1508$ consists of two components. There is just a very small position shift of $\Delta v = 0.04\,\mathrm{km\,s^{-1}}$ between the two transitions, resulting in $\Delta\alpha/\alpha = 0.5 \pm 6.0 \cdot 10^{-5}$.

Table 4.3 shows the redshift z, number of components #, and measured α variation of the three above analysed ions. They are all compatible with their 1σ confidence level with the result acquired by the Fe II analysis.

The remaining ions have all transitions with small differences in sensitivity. Although an α variation measurement is not possible, position shifts between these transitions were measured to test the general accuracy of line position fits in complex systems. Table 4.4 shows the velocity shifts between different transitions of the remaining metal system with more than one visible transition. The only ions which show significant shifts between its transitions are Mg I and Mg II. Mg I is highly unfavourable for this analysis because of the high difference in transition strength (see Table 2.1). Furthermore only the strongest part of the system (SS6) is visible in Mg I 2026, and that is blended with Zn II 2026 absorption of the same system. For a more detailed analysis of position shifts between Mg II 2796 and Mg II 2804 see sect. 4.6.1.

Table 4.4: Redshift z, number of components #, sensitivity coefficient differences ΔQ, and position shifts between transitions Δv for different ions of the $z = 1.15$ system in the line of sight of HE0515-4414.

Transitions	z	#	ΔQ	$\Delta v[\mathrm{km\,s^{-1}}]$
Mg I 2853/2026	1.1505	9	0.001	0.88 ± 0.18
Mg II 2804/2796	1.1472	6	-0.003	-0.16 ± 0.04
Mg II 2804/2796	1.1476	4	-0.003	-0.02 ± 0.10
Mg II 2804/2796	1.1481	6	-0.003	0.00 ± 0.20
Mg II 2804/2796	1.1491	2	-0.003	-0.20 ± 0.04
Mg II 2804/2796	1.1495	2	-0.003	0.04 ± 0.13
Mg II 2804/2796	1.1498	2	-0.003	0.04 ± 0.07
Mg II 2804/2796	1.1502	10	-0.003	0.32 ± 0.05
Al III 1863/1855	1.1473	5	-0.004	0.82 ± 1.20
Al III 1863/1855	1.1491	2	-0.004	-0.26 ± 0.64
Al III 1863/1855	1.1498	1	-0.004	-3.16 ± 4.66
Al III 1863/1855	1.1501	7	-0.004	-0.10 ± 0.48
Cr II 2062/2056	1.1508	5	-0.003	0.18 ± 01.11
Mn II 2594/2577	1.1508	5	-0.006	-0.16 ± 0.57
Mn II 2606/2577	1.1508	5	-0.010	-0.95 ± 0.67
Fe I 2524/2484	1.1508	2	0.016	-0.04 ± 0.75
Ni II 1742/1710	1.1508	3	-0.021	-0.19 ± 1.00
Ni II 1752/1710	1.1508	3	-0.009	0.85 ± 1.42
Ni II 1742/1710	1.1512	2	-0.021	-1.22 ± 2.19
Ni II 1752/1710	1.1512	2	-0.009	1.60 ± 2.11
Zn II 2063/2026	1.1508	4	-0.018	0.04 ± 0.41

The Mg II system is complex. Though its structure is similar to the Fe II absorption, there are obvious differences. Figure 4.4 shows the spectra of Fe II 2383 and Mg II 2804. The grey lines show the best fit positions of each component when fitted individually. Especially the strong SS3 shows a significant difference between the ions. If the line decomposition is correct, it is not saturated for both ions. The analysis from sect. 4.1.1 did show no signs of line decomposition problems and excludes the possibility of position shifts due to a strong α variation. To measure the shift between the two ions, a fit was made in which the distance between the components was fitted simultaneously. The column densities N, Doppler parameters b, and positions of the systems were fitted individually. The resulting

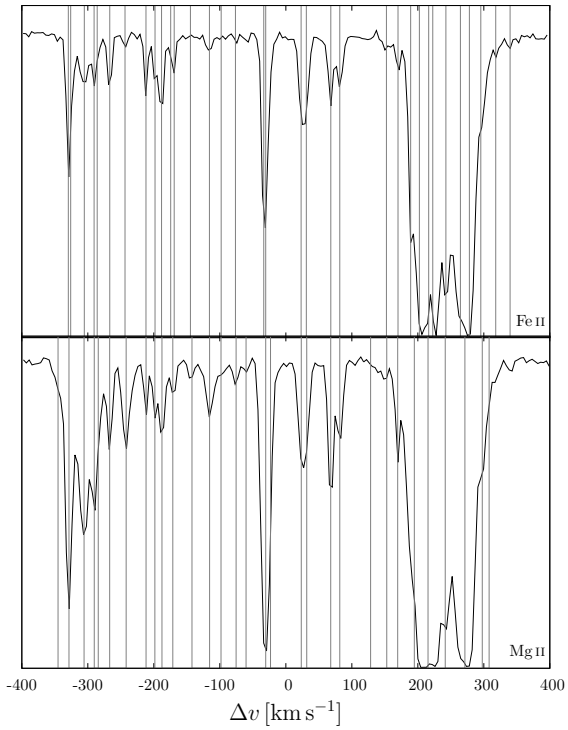

Figure 4.4: Comparison of Fe II 2383 and Mg II 2804 absorption at $z = 1.15$. The fitted line positions are indicated in grey.

distance between the two ions is $\Delta v = 2.5\,\mathrm{km\,s^{-1}}$. We note that a change in isotope abundances could not result in a shift bigger than $\Delta v \sim 50\,\mathrm{m\,s^{-1}}$ (see sect. 3.4.6). Using just this two transitions in a MM analysis would result in a misdetection of $\Delta\alpha/\alpha = (12.8 \pm 0.3) \cdot 10^{-5}$.

Table 4.5 shows the position shifts and according MM analysis results for the six subsystems. Only the results of SS4 and SS5 are compatible with a no variation model, though the results of SS1, SS4, and SS6 are compatible with the results from the SIDAM analysis. The fit error is in all cases very low. The error created by shifts due to the lines not being originated in the same gas phase is about an order of magnitude higher. This result is in agreement with our simulation in chs. 3.4.1 and 3.4.5. A statistical MM analysis is only possible if the distribution of this error is nearly Gaussian. With a large data sample the distribution of position shifts between Fe II and Mg II could be measured. If they are indeed Normal distributed, the spread of this distribution would indicate the real accuracy of the line position fits.

Table 4.5: Number of components #, position shifts between Fe II 2383 and Mg II 2804, and corresponding α variation calculations using the MM method.

System	#	$\Delta v\,[\mathrm{km\,s^{-1}}]$	$\Delta\alpha/\alpha\,[10^{-5}]$
SS1	7	0.29 ± 0.05	-1.5 ± 0.2
SS2	5	-0.58 ± 0.12	2.9 ± 0.5
SS3	2	-2.53 ± 0.05	12.8 ± 0.3
SS4	2	0.03 ± 0.17	-0.2 ± 0.8
SS5	2	0.02 ± 0.14	-0.1 ± 0.7
SS6	14	-0.46 ± 0.04	2.3 ± 0.2

4.2 ESO Large Program 2004

As a larger data sample, spectra of the ESO-VLT Large Program "The Cosmic Evolution of the IGM" were analysed. A set of 19 quasar spectra were taken over a period of two years. The data was reduced by Aracil et al. (2004). The main advantage of this data set is that many different systems are available. We analysed 16 Fe II systems in the spectra of seven quasars. The necessary criterion for the selection of systems was a visible Fe II 1608 absorption outside the Lyman α forest. The only exception was made in sect. 4.2.3 to allow a comparison with a work by Molaro et al. (2008b). For an effective use of the SIDAM method, a detailed analysis of the line positions fits of each system was made, using the line shift analysis and bisector analysis as described in chs. 3.4.4 and 3.4.5. Position shifts between Fe II 1608 and the other transitions for each system analysed in this data set, are shown in Table 4.6. A list of the best fit parameters of all systems that were analysed in this section is given in Table C.2. Original spectra and best fit of all systems are shown in B.4.

4.2.1 HE0001-2340

The bright quasar HE0001-2340 at an emission redshift of $z_{\mathrm{em}} = 2.28$ has several Fe II systems, one of them a strong damped Lyman α (DLA) system. The system at $z = 1.59$, composed of a single visual component, is quite weak, so the important

Fe II 1608 and Fe II 2374 transitions are highly influenced by noise. The line shift analysis (Fig. 4.5) shows a position offset between these two transitions and the stronger transitions. There is, however, no strong correlation of line positions and transition strengths. The regression analysis would give $\Delta\alpha/\alpha = (3.8 \pm 0.6) \cdot 10^{-5}$. Using just a comparison of line positions of Fe II 1608 and Fe II 2374 changes the result to $\Delta\alpha/\alpha = (1.5 \pm 0.8) \cdot 10^{-5}$.

The bisectors of the lines show that the weaker transition, especially Fe II 1608, deviate strongly from a symmetric shape while the strong transitions are symmetric (Fig. 4.6). These lines do not show a velocity shift bigger than 1σ (statistical) to each other. It thus has to be assumed that the position offset between the weak and the strong transitions is created by the deformation of the lines by noise or lien blends.

The $z = 1.59$ system in HE0001-2340 was also analysed by Agafonova et al. (2011) with a new set of data obtained in 2009. They compared Fe II 1608 with Fe II 2383 and found $\Delta\alpha/\alpha = (-0.05 \pm 1.1) \cdot 10^{-5}$.

The DLA system at $z = 2.19$ has two distinct Fe II features at $z_1 = 2.1853$ and $z_2 = 2.1871$. Subsystem 1 is quite weak and only three transitions are available (Fe II 1608, Fe II 2344, and Fe II 2383). The other three transitions are blended with telluric lines. The line shift analysis is highly dominated by the strong Fe II 2383 (Fig. 4.5). Using all three transitions with a one component fit gives an apparent variation of $\Delta\alpha/\alpha = (1.8 \pm 0.9) \cdot 10^{-5}$.

Figure 4.5 shows a stronger correlation of the line positions with transition strength $f\lambda_0$ than with sensitivity coefficient Q, indicating problems with line decomposition. Without Fe II 2600, the influence of this effect on the total position shifts cannot be quantified. Since Fe II 2374 and Fe II 2587 are not available in this system, the best way to proceed would be to compare line positions of Fe II 1608 and Fe II 2344. The bisector of Fe II 1608 shows a slight slope, possibly created by noise, which can account for some unwanted shift. Disregarding Fe II 2383 would give $\Delta\alpha/\alpha = (-0.7 \pm 1.0) \cdot 10^{-5}$.

The second Fe II feature in this sub-DLA system is stronger. Fe II 2383 is shifted by $\Delta v = 0.75\mathrm{km\,s^{-1}}$ (17σ) from the position of the other transitions. The bisector looks similar to that of Fe II 2600. It is possible that a local error in the wavelength calibration is responsible. Since the line position n is not compatible with the line positions of transitions with similar strength and sensitivity, it was not used in the analysis. All remaining transitions would give $\Delta\alpha/\alpha = (1.8 \pm 0.3) \cdot 10^{-5}$, using a two component fit. Using only Fe II 2374 in comparison with Fe II 1608 gives $\Delta\alpha/\alpha = (1.6 \pm 0.4) \cdot 10^{-5}$.

This system was previously analysed by Molaro et al. (2008b). In the first subsystem they only used line positions of Fe II 2383 in comparison with Fe II 1608 and got a result similar to ours of $\Delta\alpha/\alpha = (2.3 \pm 1.0) \cdot 10^{-5}$. For the second subsystem they compared the line position of Fe II 1608 with a combined position of Fe II 2344 and Fe II 2587, getting $\Delta\alpha/\alpha = (2.1 \pm 0.3) \cdot 10^{-5}$. They concluded that the shift was created by wavelength calibration problems. We propose that the effect is mainly based on an unresolved substructure of the lines.

Agafonova et al. (2011) compared the position of Fe II 1608 with that of Fe II 2344 of the combined $z = 2.19$ system. They found a slightly lower value of $\Delta\alpha/\alpha = (0.96 \pm 0.45) \cdot 10^{-5}$. A reanalysis of the data used by Agafonova et al. (2011) is done in sect. 4.3.

4.2.2 HE1341-1020

In the spectrum of HE1341-1020 ($z_{\mathrm{em}} = 2.14$) there is one system with a suitable Fe II 1608 transition at $z_2 = 1.92$. It is composed of at least two resolved components. A significant position offset between Fe II 1608 and the other Fe II transitions was measured. The line positions are stronger correlated with sensitivity Q than with transition strength $f\lambda_0$ (Fig. 4.5). Fe II 2374 is not available because of blends with telluric lines. A comparison of line positions of Fe II 1608 and Fe II 2587 results in $\Delta\alpha/\alpha = (6.4 \pm 1.2) \cdot 10^{-5}$, while all available transitions in a regression analysis give $\Delta\alpha/\alpha = (5.7 \pm 1.2) \cdot 10^{-5}$. The bisector of Fe II 1608 differs slightly from that of the other transitions. The also weak Fe II 2587 shows a line profile similar to the strong transitions. We thus have to assume that the velocity shift here is created by some unknown mechanism, e.g. an unrecognised blend, which distorts the line shape of Fe II 1608.

4.2.3 HE1347-2457

There is a strong and heavily blended Fe II system at $z = 1.44$ in the spectrum of HE1347-2457

Table 4.6: Position shifts of Fe II 2344, Fe II 2374, Fe II 2383, Fe II 2587 and Fe II 2600 in comparison to Fe II 1608 for each system of the 2004 Large program sample.

QSO	z	$\Delta v_{2344}[\mathrm{km\,s^{-1}}]$	$\Delta v_{2374}[\mathrm{km\,s^{-1}}]$	$\Delta v_{2383}[\mathrm{km\,s^{-1}}]$	$\Delta v_{2587}[\mathrm{km\,s^{-1}}]$	$\Delta v_{2600}[\mathrm{km\,s^{-1}}]$
HE0001-2340	1.5864	-1.02 ± 0.23	-0.54 ± 0.31	-1.17 ± 0.22	-1.44 ± 0.27	-1.27 ± 0.22
HE0001-2340	2.1853	0.21 ± 0.32		-0.43 ± 0.30		
HE0001-2340	2.1871	-0.52 ± 0.10	-0.57 ± 0.20	-1.33 ± 0.10	-0.83 ± 0.12	-0.54 ± 0.310
HE1341-1020	1.9153	-1.62 ± 0.42		-1.50 ± 0.41	-2.23 ± 0.43	-1.85 ± 0.42
HE1347-2457	1.4392	0.26 ± 0.05			0.19 ± 0.05	0.91 ± 0.05
HE2217-2818	1.6910	-0.11 ± 0.16	-0.21 ± 0.21	0.05 ± 0.15	0.03 ± 0.18	-0.31 ± 0.15
HE2217-2818	1.6925	-1.22 ± 0.63	-0.03 ± 0.78	-0.52 ± 0.62	-0.45 ± 0.67	-0.73 ± 0.62
PKS0237-23	1.6358	-1.81 ± 0.75		-1.62 ± 0.74	-1.71 ± 0.75	-1.83 ± 0.74
PKS0237-23	1.6369	-2.13 ± 0.38		-1.77 ± 0.38	-1.94 ± 0.39	-1.77 ± 0.37
PKS0237-23	1.6717	-0.68 ± 0.46	0.45 ± 0.61	-0.85 ± 0.45		-0.69 ± 0.45
PKS0237-23	1.6723	0.02 ± 0.03	0.30 ± 0.03	0.00 ± 0.04	0.06 ± 0.03	-0.10 ± 0.03
PKS2126-158	2.7684	-0.02 ± 0.07	-0.41 ± 0.10	0.18 ± 0.06		
Q0002-422	2.1678	-0.39 ± 0.35	-0.05 ± 0.62	-0.34 ± 0.32		
Q0002-422	2.3006	-0.02 ± 0.45	-0.74 ± 0.71	-0.39 ± 0.42		
Q0002-422	2.3008	-1.53 ± 0.61	-1.51 ± 0.97	-1.74 ± 0.57		
Q0002-422	2.3015	-0.14 ± 0.06	-0.51 ± 0.08	-0.16 ± 0.07		

($z_{\mathrm{em}} = 2.6$), which has previously been analysed by Molaro et al. (2008b). The lines of all transitions are saturated which would make the influence of an incorrect decomposition very strong. Fe II 1608 is located in the Lyman α forest, so all results should be regarded with care since an undiscovered blend with a Lyman α line could produce a significant position shift. This system is included here to allow a comparison with Molaro et al. (2008b). Fe II 2374 and Fe II 2383 fall into a data gap and are not available.

Fe II 2600 is shifted by $\Delta v = 0.73\,[\mathrm{km\,s^{-1}}]$ (30σ) in comparison with the other transitions. The combination of line blends and saturation make a correct decomposition unlikely. The correlation of position and transition strength is very strong (Fig. 4.5). The position shifts of Fe II 2344, Fe II 2587, and Fe II 2600 are most likely caused by an incorrect line decomposition. The offset of Fe II 1608 could also be explained by an unrecognised blend with a Lyman α feature.

Assuming that this is not the case, the best approach would be just to use Fe II 1608 and Fe II 2587 to avoid problems with incorrect line decomposition; however, Fe II 2587 is blended with some telluric lines. Comparing the position of these two lines nevertheless, would give an α variation of $\Delta\alpha/\alpha = (-0.5 \pm 0.1) \cdot 10^{-5}$, while all transitions give $\Delta\alpha/\alpha = (-1.7 \pm 0.1) \cdot 10^{-5}$. Since the system is quite strong, the statistical error is low. Molaro et al. (2008b) state a similar result of $\Delta\alpha/\alpha = (-2.1 \pm 0.2_{\mathrm{stat}} \pm 1.1_{\mathrm{sys}}) \cdot 10^{-5}$ using Fe II 1608, Fe II 2344, and Fe II 2587. They have included a systematical error for the wavelength calibration (see chap. 5).

Assuming that the strong linear correlation of line positions and transition strengths (4.5) is created by line decomposition problems, the line positions can be corrected as shown in sect. 3.4.4. Since Fe II 2383 is not available, the best option is to use Fe II 2587 and Fe II 2600 because of their similar sensitivity coefficients. Assuming a linear correlation between line positions and transition strengths, the influence of shifts due to line decomposition problems can be estimated and subtracted from the measured line positions. In this case the resulting α variation calculations give $\Delta\alpha/\alpha = (-0.1 \pm 0.1) \cdot 10^{-5}$ for both, the regression analysis and for a comparison of Fe II 1608 and Fe II 2587 line positions.

4.2.4 HE2217-2818

The quasar HE2217-2818 ($z_{\mathrm{em}} = 2.41$) has several Fe II systems, one of which has a visible Fe II 1608 absorption at $z = 1.69$. The system consists of two parts, at $z_1 = 1.6910$ and $z_2 = 1.6925$, which will be dealt with separately. They consist of at least

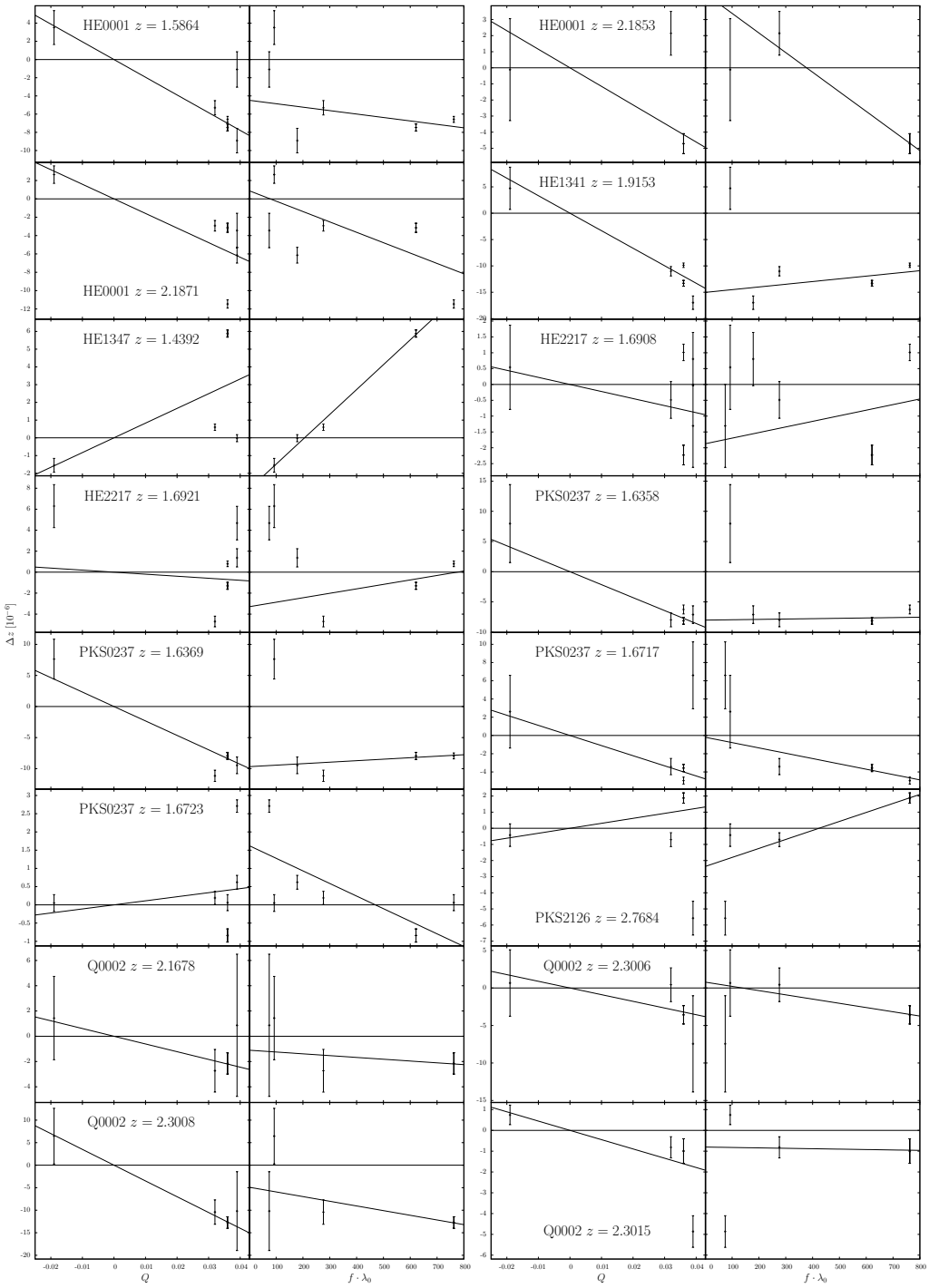

Figure 4.5: Line shift analysis of 16 Fe II systems in eight quasar spectra. The relative position shift is plotted against the sensitivity coefficient Q and the transition strength $f\lambda_0$ for each system.

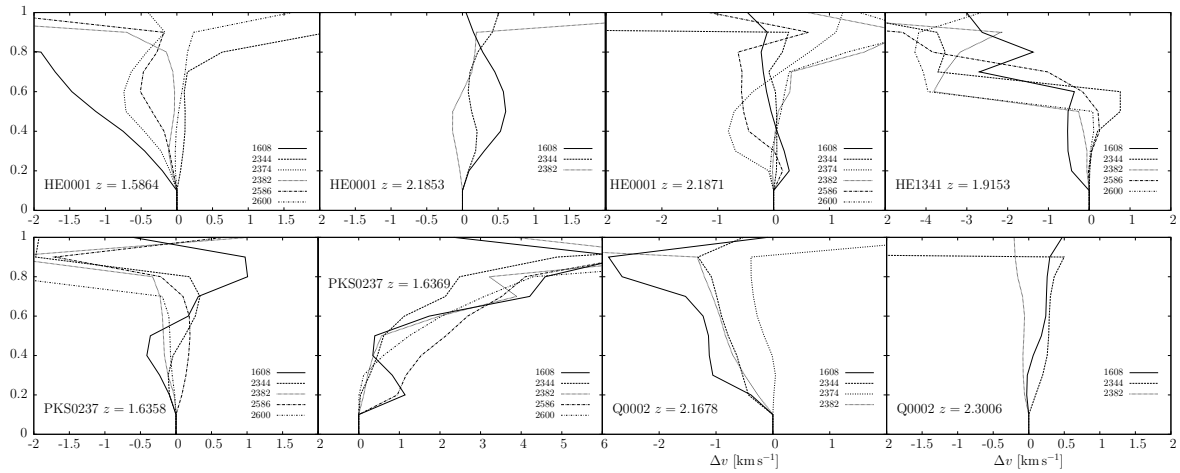

Figure 4.6: Bisectors of isolated Fe II lines of the 2004 ESO Large Program data sample. The lines are parametrised from their centres (0) up to the continuum (1) to allow a comparison between different transitions.

five and seven blended components, respectively.

The first part has a significant shift between the two strong transitions of $\Delta v \sim 0.36\,\mathrm{km\,s^{-1}}$ (10σ), which is a good indication of decomposition problems. There is, however, no strong indication of a correlation between position shift and transition strength (Fig. 4.5). Fe II 2344 and Fe II 2587 are blended with telluric lines and are thus excluded. The reason for the shift of the Fe II 2600 is unknown, possibly an unrecognised blend or wavelength calibration problems. Using just Fe II 2374 in comparison with Fe II 1608 with a five-component fit gives $\Delta\alpha/\alpha = (0.6 \pm 0.5) \cdot 10^{-5}$. All components would have given $\Delta\alpha/\alpha = (0.4 \pm 0.4) \cdot 10^{-5}$.

Fe II 2344 of the second part of the system is also influenced by the blend, explaining the strong position offset. An 7σ offset between the strong transitions of $\Delta v \sim 0.23\,\mathrm{km\,s^{-1}}$ indicates a slight decomposition problem (Fig. 4.5). The blend of Fe II 2587 that affects the first part of the system has no visible influence on the second part. There is however the possibility that the feature causing the blend has more components that also affect the second part of the system. Again using only Fe II 1608 and Fe II 2374 gives $\Delta\alpha/\alpha = (0.5 \pm 0.7) \cdot 10^{-5}$. All transitions, except the obviously blended Fe II 2344, would give a result of $\Delta\alpha/\alpha = (1.9 \pm 0.7) \cdot 10^{-5}$. Recently Molaro et al. (2013) did an analysis of this system with data from a new observation of this quasar. Using all transitions and using the α variation as a fit parameter they obtained $\Delta\alpha/\alpha = (0.1 \pm 0.3 = \cdot 10^{-5}$ for the combined system. We did a reanalysis of this data in sect. 4.4.

4.2.5 PKS0237-23

The quasar PKS0237-23 ($z_{\mathrm{em}} = 2.22$) has several metal systems, including three close Fe II systems at $z_1 = 1.64$, $z_2 = 1.66$ and $z_3 = 1.67$. Fe II 1608 of the $z = 1.66$ system is heavily blended, so that a reliable position estimation is not possible. The remaining two systems are separated into two subsystems each.

In the first part of the $z = 1.64$ system, at $z_1 = 1.6358$, Fe II 1608 shows a high position offset of $\Delta v \approx 1.7\,\mathrm{km\,s^{-1}}$ in comparison with the other transitions. It is, however, slightly blended with an unidentified feature. A blend will in most cases create a shift, because the unknown line will probably not be symmetric itself and cannot be subtracted correctly. The bisector (Fig. 4.6) shows that only Fe II 1608 deviates obviously from a symmetrical shape. Fe II 2374 is blended with the much stronger Fe II 2344 of the $z = 1.67$ system. The position estimation is thus unreliable and it is neglected. The $z - f\lambda_0$ diagram shows no strong signs of correlation (Fig. 4.5). Using all lines with a two-component fit, an α variation of $\Delta\alpha/\alpha = (4.1 \pm 2.0) \cdot 10^{-5}$ would be measured. Using just Fe II 2587 would

give $\Delta\alpha/\alpha = (4.9 \pm 2.1) \cdot 10^{-5}$.

The second part of the system, at $z_2 = 1.6369$, is an asymmetric feature consisting of at least five heavily blended components. Fe II 1608 also shows a strong position offset of $\Delta v \approx 1.9\,\mathrm{km\,s^{-1}}$ in comparison to the other transitions (Fig. 4.5). Fe II 2374 is not used for the same reason as in the first part of the system. Using all the remaining transitions would give $\Delta\alpha/\alpha = (4.4 \pm 1.0) \cdot 10^{-5}$, using just Fe II 2587 gives $\Delta\alpha/\alpha = (5.6 \pm 1.1) \cdot 10^{-5}$. Although no obvious blend is seen in this case, the position of the strong Fe II 2344 is at a 3σ distance from the regression line. No correlation of position shift and transition strength can be seen (Fig. 4.5). The bisector again shows a difference in line shape between the weak and the strong transitions (Fig. 4.6). The data quality is too low to decide whether this is the cause for the shift.

The $z = 1.67$ system consists of two parts with at least three and five components, respectively. The first part, at $z_1 = 1.6717$, shows a position offset between the weak and the strong transitions, correlated with transition strength (Fig. 4.5). Fe II 2587 is not available. Using only the other two weak transitions gives $\Delta\alpha/\alpha = (-1.3 \pm 1.5) \cdot 10^{-5}$, while all transitions would result in $\Delta\alpha/\alpha = (2.1 \pm 1.3) \cdot 10^{-5}$. Assuming that the position shift between Fe II 2383 and Fe II 2600 comes from line decomposition problems alone, the line positions of all transitions can be corrected as shown in sect. 3.4.4. Doing a regression analysis with the corrected line positions gives $\Delta\alpha/\alpha = (-1.1 \pm 1.3) \cdot 10^{-5}$. Comparing the positions of the corrected Fe II 1608 and Fe II 2374 transitions gives the same result as with the uncorrected line positions.

The second part of this system, at $z_2 = 1.6723$, shows a shift of Fe II 2374 in comparison to the other lines. Although the stronger transitions are saturated, no obvious correlation between position shift and transition strength can be seen (Fig. 4.5). Since even the positions of Fe II 2587, the transition that is closest to Fe II 2374 in terms of strength and sensitivity, is incompatible with the position of Fe II 2374, the latter is not used for the analysis. Using all remaining transitions gives $\Delta\alpha/\alpha = (0.1 \pm 0.1) \cdot 10^{-5}$, while a comparison of line positions of Fe II 1608 and Fe II 2587 would give $\Delta\alpha/\alpha = (-0.2 \pm 0.1) \cdot 10^{-5}$.

4.2.6 PKS2126-158

The quasar PKS2126-158 ($z_{\mathrm{em}} = 3.28$) has a strong system at $z = 2.77$ composed of two separate parts at $z_1 = 2.7674$ and $z_2 = 2.7684$. Because of the high redshift of the system, Fe II 2587 and Fe II 2600 are not available. Fe II 1608 of the first subsystem is blended with a C IV 1551 feature at $z = 2.91$. To avoid shifts due to the blend and because of a strong noise peak in the same part of the absorber in Fe II 2374, only the second part of the system, which is apparently unaffected, is used. It consists of at least eight components. The line shift analysis shows a strong shift of Fe II 2374 (Fig. 4.5), which cannot be accounted for. Because its position is incompatible with the position of the other transitions with comparable sensitivities, it is not used in the analysis. Using the remaining three lines gives $\Delta\alpha/\alpha = (1.0 \pm 0.3) \cdot 10^{-5}$. To avoid effects by the heavy saturation of Fe II 2383, the best result is given by a comparison of Fe II 2344 with Fe II 1608, namely $\Delta\alpha/\alpha = (-0.2 \pm 0.3) \cdot 10^{-5}$.

4.2.7 Q0002-422

The quasar Q0002-422 ($z_{\mathrm{em}} = 2.77$) has two high redshift systems with visible Fe II 1608 absorption. The first system ($z = 2.17$) seems to be a simple blend of two lines. The $z - f\lambda_0$ diagram suggests a slight correlation of position and transition strength (Fig. 4.5). The bisector shows a difference in line shape that might be created by noise, since the general slope is similar for all lines (Fig. 4.6). Fe II 2587 and Fe II 2600 are not available. Comparing line positions of Fe II 1608 and Fe II 2374 gives $\Delta\alpha/\alpha = (0.1 \pm 1.4) \cdot 10^{-5}$, while all available transitions would give $\Delta\alpha/\alpha = (1.0 \pm 1.0) \cdot 10^{-5}$.

The second system, at $z = 2.30$, is divided into three subsystems at $z_1 = 2.3006$, $z_2 = 2.3008$, and $z_3 = 2.3015$. Because Fe II 2374 is blended with telluric lines, only three transitions (Fe II 1608, Fe II 2344, and Fe II 2383) are available in the whole system. The first part of the system, at $z_1 = 2.3006$, consists of a single weak line. The bisector of this feature shows no strong asymmetry for all three transitions (Fig. 4.6). The $z - f\lambda_0$ diagram shows a slight correlation of position and transition strength (Fig. 4.5). Because there are no transitions with equal sensitivity coefficients it is not possible to verify that the position shifts

Table 4.7: Results of the α variation analyses for Fe II systems in the data of the 2004 Large Program.

QSO	z	$\Delta\alpha/\alpha_{\rm all}$ $[10^{-5}]$	$\Delta\alpha/\alpha_{\rm weak}$ $[10^{-5}]$	Status
HE0001-2340	1.5864	3.8 ± 0.6	1.5 ± 0.8	bad
HE0001-2340	2.1853	1.8 ± 0.9	$-0.7 \pm 1.0_{2344}$	good
HE0001-2340	2.1871	1.8 ± 0.3	1.6 ± 0.4	good
HE1341-1020	1.9153	5.7 ± 1.2	$6.4 \pm 1.2_{2587}$	bad
HE1347-2457	1.4392	-1.7 ± 0.1	$-0.5 \pm 0.1_{2587}$	bad
HE2217-2812	1.6910	0.4 ± 0.4	0.6 ± 0.5	good
HE2217-2812	1.6925	1.9 ± 0.7	0.5 ± 0.7	good
PKS0237-23	1.6358	4.1 ± 2.0	$4.9 \pm 2.1_{2587}$	bad
PKS0237-23	1.6369	4.4 ± 1.0	$5.9 \pm 1.1_{2585}$	bad
PKS0237-23	1.6717	2.1 ± 1.3	-1.3 ± 1.5	good
PKS0237-23	1.6723	-0.1 ± 0.1	$-0.2 \pm 0.1_{2587}$	good
PKS2126-158	2.7684	1.0 ± 0.3	$-0.2 \pm 0.3_{2344}$	good
Q0002-422	2.1678	1.0 ± 1.0	0.1 ± 1.4	good
Q0002-422	2.3006	1.3 ± 1.2	$0.1 \pm 1.4_{2344}$	good
Q0002-422	2.3008	5.1 ± 1.9	$5.3 \pm 1.7_{2344}$	bad
Q0002-422	2.3015	0.5 ± 0.2	$0.5 \pm 0.2_{2344}$	good

The third column shows the apparent α variation when all available transitions were used in a regression analysis, the fourth column when a comparison of Fe II 1608 and Fe II 2374 was used. For the cases where Fe II 2374 was not available, the used transition is given in the subscript.

are created by decomposition problems. Using just Fe II 2344 in comparison with Fe II 1608 gives $\Delta\alpha/\alpha = (0.1 \pm 1.4) \cdot 10^{-5}$, while all available transitions in regression analysis would give $\Delta\alpha/\alpha = (1.3 \pm 1.2) \cdot 10^{-5}$.

The second part of the system, at $z_1 = 2.3008$, is a weak and close blend of at least two components. Fe II 1608 barely exceeds the noise, making the position estimation unreliable. The system has a nearly perfect correlation of position shift and sensitivity coefficient, suggesting a variation of $\Delta\alpha/\alpha = (5.0 \pm 1.9) \cdot 10^{-5}$ (Fig. 4.5) using positions of Fe II 2344 and Fe II 1608. Using all three transitions in a regression analysis gives $\Delta\alpha/\alpha = (5.3 \pm 1.7) \cdot 10^{-5}$.

The third part of the system, at $z_1 = 2.3015$, consists of a blend of at least ten components, some of which are saturated in Fe II 2383. As in the second part of the system, there is a strong correlation of line line positions and sensitivities, however with a lower magnitude. An α variation of $\Delta\alpha/\alpha = (0.5 \pm 0.2) \cdot 10^{-5}$ would be measured using all three available lines. The lack of available transitions makes a determination of possible systematic effects difficult. Because of the saturation of several components in the stronger transitions, some position shift would be expected and is supported by the $z - f\lambda_0$ correlation (Fig. 4.5). Using only Fe II 2344 in comparison with Fe II 1608 gives the same result of $\Delta\alpha/\alpha = (0.5 \pm 0.2) \cdot 10^{-5}$.

4.2.8 Summary of 2004 Large Program data

Table 4.7 shows the result of the α variation measurements of all systems studied in this section. For six of them, marked BAD, Fe II 1608 is not suitable, as shown above. For the remaining ten systems, five of which have a usable Fe II 2374, we find an average apparent variation of $\Delta\alpha/\alpha = (0.1 \pm 0.8) \cdot 10^{-5}$. The average is calculated without weights because the main errors are expected to be systematic with an unknown distribution. Using all available transitions in all systems, including

those labelled bad, with a regression analysis would result in an average α variation measurement of $\Delta\alpha/\alpha = (2.1 \pm 2.0) \cdot 10^{-5}$.

Table 4.6 shows the relative position shifts of each transition in comparison with Fe II 1608 with their respective statistical 1σ confidence level. Of the 61 values stated in the table, only 21% show a position shift that is smaller than 1σ while 38% of the positions shifts are within 2σ. Assuming that no α variation is present, as indicated by the above analyses, the statistical position fit errors are strongly underestimated. The error of each single position fit would have to be increased by a factor ~ 3.8 to fulfil the 67% statistics. For the subsample of systems labelled as GOOD in Table 4.7, 34% of position shifts are with 1σ. For the 67% statistics, the position fit errors would still need to be increased by a factor ~ 2.6. As the simulations in chap. 3 have shown, differences in transition strengths can be in part responsible for the shifts, which would not be reflected in the statistical position fit errors.

In nine systems the strong Fe II 2383 and Fe II 2600 transitions were present. Only in one case they were positioned within their respective statistical position fit error. An average distance of $\Delta v = 0.05 \pm 0.33\,\mathrm{km\,s^{-1}}$ between the two line position was measured. The spread of the values is about five times higher than the statistical error of the position distance of the two transitions. Taking this value as a measure of the uncertainty given by wavelength calibration or other sources of line position shifts, corresponds to an accuracy limit of $\sigma_{\Delta\alpha/\alpha} = 1.0{\cdot}10^{-5}$ for a single SIDAM measurement with this data set. Molaro et al. (2008b) estimated a wavelength calibration uncertainty of 1/10 pixel size for this data, giving nearly the same value of $\sigma_{wc} = 1.2 \cdot 10^{-5}$. A more detailed study of the position fit accuracy with a larger data sample is done in sect. 4.6.1 by comparing line position fits of Mg II 2796 and Mg II 2804.

4.3 HE0001-2340 2009 data

In September 2009 a new observation of the quasar HE0001-2340 with the UVES spectrograph at the VLT in Chile was made. The main purpose of the new observations was to achieve the best possible wavelength calibration with the instruments available. A small slit width of 0.7" and no pixel binning resulted in a high resolution spectrum ($R \approx 65000$) but with a cutback in the signal to noise ratio. Table 4.8 shows the wavelength ranges, number of individual exposures, and signal to noise ratios of the different observation settings. For further details of the data reduction process we refer to Agafonova et al. (2011).

Table 4.8: Wavelength ranges, number of exposures, and signal to noise ratios of a single exposure for different observation settings.

Setting	λ [Å]	$\#_{\mathrm{exp}}$	S/N
BLUE 390	3290 - 4519	8	8-24
BLUE 437	3759 - 4985	3	19-34
RED 580L	4788 - 5763	8	22-28
RED 580U	5836 - 6809	8	26-35
RED 760L	5694 - 7532	3	25-41
RED 760U	7660 - 9465	3	40-58

4.3.1 Position shifts between exposures

Wavelength shifts between different exposures can be responsible for distortions of line profiles. Because the different Fe II transitions are in located in parts of the spectrum that were taken with different observation settings, these distortions can mimic a variation of fundamental constants.

To check for wavelength shifts between different exposures, parts of each spectrum were cross correlated. As a first step, constant shifts between whole exposures were probed. The cross-correlation

$$(f \star g)[n] = \sum_{m=-\infty}^{\infty} f^*[m]g[n+m]$$

can be used to calculate an offset between two similar functions f and g. At the point $n_{\max}$ which is given by the maximum of the $f \star g$ distribution, the functions have the highest concordance. To achieve a sub-pixel accuracy, the spectra were expanded to ten times the original pixel resolution, using a cubic spline interpolation. Figure 4.7 shows an example of the cubic spline interpolation on an exposure of the blue part of the spectrum. The crosses show the original flux values and the solid line the interpolated spectrum. As a comparison a χ^2 method

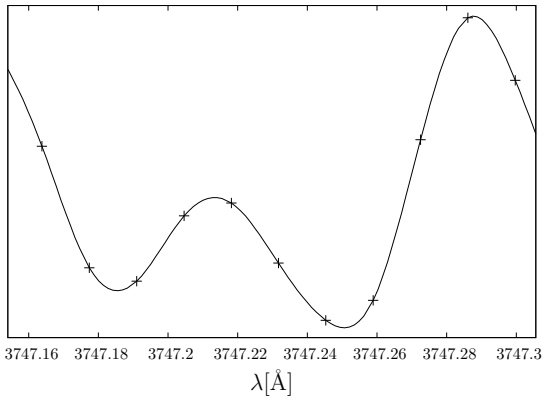

Figure 4.7: Example for the cubic spline interpolation on exposure 6 in BLUE 390. The crosses show the original flux values and the solid line the interpolated spectrum.

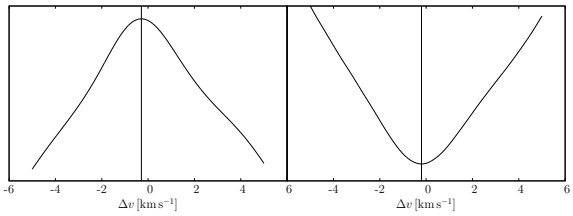

Figure 4.8: Cross correlation and χ^2 method for aligning exposures 1 and 2 of BLUE 390.

was used as well. The minimum of the function $\chi^2 = \sum_x (f(x) - g(x))^2$ gives the highest concordance between the two exposures. Figure 4.8 shows the result of a cross correlation and the χ^2 method for two exposures of BLUE 390.

There are eight exposures of the lower wavelength range, on the blue arm of the spectrograph ranging from $\lambda \sim 3300\,\text{Å} - 4500\,\text{Å}$ (BLUE 390), and on the red arm from $\lambda \sim 4800\,\text{Å} - 6800\,\text{Å}$ with a gap between 5760 Å and 5840 Å (RED 580L and RED 580U). The signal to noise ratio ranges from $S/N \sim 8 - 24$ in the blue arm to $S/N \sim 22 - 28$ and $S/N \sim 26 - 35$ in the lower and upper part of the red arm, respectively. The higher wavelength range consists of three exposures each. It ranges from $\lambda \sim 3760\,\text{Å} - 4980\,\text{Å}$ on the blue arm (BLUE 437) and $\lambda \sim 5700\,\text{Å} - 9460\,\text{Å}$ with a gap between 7530 Å and 7660 Å on the red arm of the spectrograph (RED 760L and RED 760U). The signal to noise ratio of these exposures range from $S/N \sim 19 - 34$ in the blue arm to $S/N \sim 25 - 41$ and $S/N \sim 40 - 58$ in the lower and upper part of the red arm, respectively.

Table 4.9: Shifts between different exposures of HE0001 2009 data in the low wavelength range

Exp	1	2	3	4	5	6	7	8
				BLUE 390				
1	0.00	-0.19	-0.29	0.23	-0.25	-0.51	-0.43	-1.35
2	0.19	0.00	0.09	0.07	-0.12	-0.08	-0.39	-1.54
3	0.28	-0.10	0.00	-0.39	-0.06	-0.00	0.14	-1.49
4	0.10	-0.01	0.42	0.00	-0.61	0.22	0.02	-1.47
5	0.24	0.13	0.03	0.77	0.00	-0.19	-0.19	-1.10
6	0.51	0.19	0.23	0.13	0.23	-0.00	0.13	-0.88
7	0.44	0.42	-0.19	0.08	0.20	-0.12	0.00	-0.08
8	1.33	1.55	1.44	1.51	1.08	0.84	0.09	0.00
				RED 580L				
1	0.00	-0.14	-0.79	-0.99	-0.99	-1.39	-1.55	-1.64
2	0.17	0.00	-0.69	-0.70	-0.87	-1.22	-1.27	-1.51
3	0.75	0.71	0.00	-0.18	-0.19	-0.58	-0.74	-0.95
4	0.92	0.73	0.12	0.00	-0.08	-0.39	-0.54	-0.73
5	0.99	0.90	0.15	0.03	0.00	-0.30	-0.46	-0.65
6	1.39	1.24	0.54	0.34	0.26	0.00	-0.15	-0.34
7	1.50	1.29	0.70	0.49	0.42	0.11	0.00	-0.18
8	1.63	1.53	0.91	0.69	0.62	0.31	0.15	0.00
				RED 580U				
1	0.00	-0.06	-0.73	-1.00	-0.87	-1.27	-1.43	-1.70
2	0.08	0.00	-0.65	-0.64	-0.90	-1.29	-1.41	-1.57
3	0.75	0.68	0.0	-0.17	-0.21	-0.51	-0.73	-0.99
4	1.00	0.68	0.17	0.00	-0.10	-0.38	-0.51	-0.74
5	0.89	0.94	0.23	0.12	0.00	-0.40	-0.71	-0.48
6	1.29	1.30	0.54	0.41	0.41	0.00	-0.15	-0.39
7	1.43	1.42	0.76	0.52	0.71	0.18	0.00	-0.23
8	1.70	1.58	1.01	0.75	0.48	0.41	0.24	0.00

Shifts given in km s^{-1}

The cross correlation was calculated over an interval of $\Delta v = 10\,\text{km s}^{-1}$. Because the slope of the continuum differs in different part of the spectrum, each exposure was normalised. Figure 4.9 shows the results for the different exposures of BLUE 390. $f \star g$ was calculated as well as $g \star f$. Calculating both correlations gives a measure of the uncertainty that is introduced by the interpolation process, because only one of the exposures is interpolated in each case. The velocity resolution was $\Delta v = 0.01\,\text{km s}^{-1}$. The self cross correlation always gives a peak at $\Delta v = 0\,\text{km s}^{-1}$.

The cross correlation results for the other instrument settings are shown in B.4. They are summarised in Table 4.9. Significant velocity shifts of up to $\Delta v = 1.5\,\text{km s}^{-1}$ between the exposures were measured. The difference between $f \star g$ and $g \star f$ is always at a range of several $10\,\text{m s}^{-1}$ and thus in

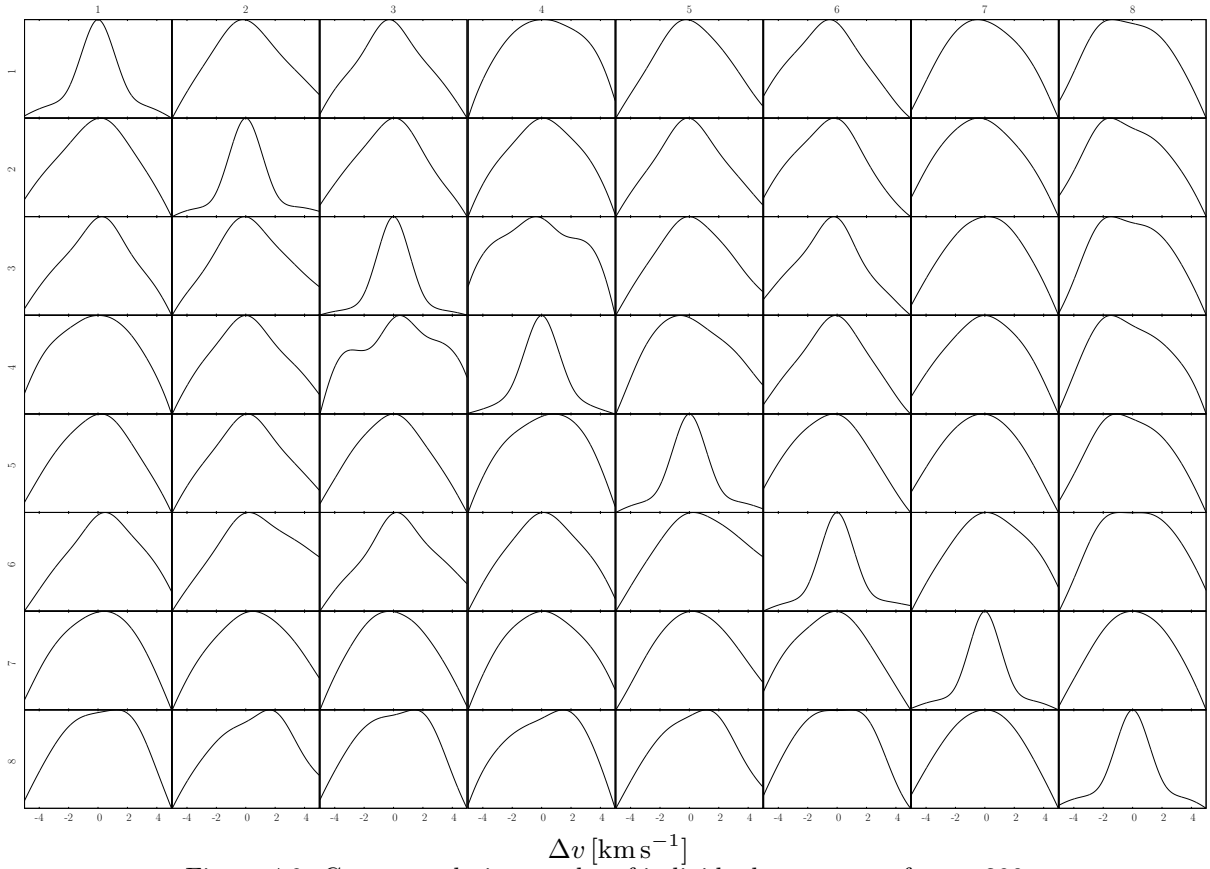

Figure 4.9: Cross correlation results of individual exposures of BLUE 390

most cases small compared to the shift itself.

Table 4.10 shows the results for the higher wavelength range. In the blue arm of the spectrograph shifts of up to $\Delta v = 0.2\,\mathrm{km\,s^{-1}}$, and in the red arm up to $\Delta v = 0.8\,\mathrm{km\,s^{-1}}$ were measured.

The asymmetric peaks of the cross correlation curves between exposures with a high velocity offset (Fig. 4.9) could indicate differential shifts within the exposures. To probe this possibility, the procedure was repeated for various wavelength ranges in RED 580L. Table 4.11 shows the position shifts between exposure 1 and the other exposures for several 200 Å intervals. Except the lower wavelength range (4800 Å - 5200 Å) the results are consistent. This indicates that differential shifts within the exposures only have a minor influence on the position offsets between individual exposures.

Agafonova et al. (2011) used a different method to align the exposures. They expected the position shifts to vary within each exposure and thus chose strong lines in the direct vicinity of absorption features, that are relevant to their analysis, to do a local correction. The signal to noise ratio of the single exposures is low, resulting also in a low precision of position estimations of single lines. Though local shifts can only be found with this method, the low precision makes it susceptible to misdetections.

To compare the two approaches, position shifts between the exposures of a complex absorption system, ranging from 5315 Å to 5328 Å, were measured with the cross correlation method. The system forms the most distinctive feature in the 5200 Å to 5400 Å, range in RED580L. The last row of table 4.11 shows the cross correlation results for this absorption system. For some exposures the resulting position shifts are in good agreement with each other, while for others there are differences of several hundred $\mathrm{m\,s^{-1}}$.

Though there are indications for differential position shifts within each exposure, the total shift be-

Table 4.10: Shifts between different exposures of HE0001 new data at the high wavelength range.

	1	2	3
	BLUE 437		
1	0.00	0.18	-0.06
2	-0.15	0.00	-0.14
3	0.10	0.18	0.00
	RED 760L		
1	0.00	0.04	-0.34
2	-0.36	0.00	-0.43
3	0.21	0.27	0.00
	RED 760U		
1	0.00	0.10	-0.78
2	-0.27	0.00	-0.54
3	0.71	0.47	0.00

Shifts given in $\mathrm{km\,s^{-1}}$

Table 4.11: Comparison of shifts between different exposures and exposure 1 of HE0001-2340 2009 data RED580L in various wavelength ranges. The last row shows the corresponding shifts for a single complex absorption system.

λ [Å]	2	3	4	5	6	7	8
4800-5000	-0.01	-0.44	-0.69	-0.95	-1.27	-1.46	-1.45
5000-5200	-0.36	-0.97	-1.39	-1.21	-1.85	-2.02	-2.04
5200-5400	-0.25	-0.75	-0.95	-1.05	-1.40	-1.29	-1.60
5400-5600	-0.28	-0.94	-1.17	-1.04	-1.38	-1.56	-1.78
5600-5760	-0.19	-0.77	-1.00	-0.91	-1.35	-1.53	-1.59
5310-5330	-0.32	-0.53	-0.90	-0.86	-1.26	-0.79	-1.19

Position shifts are given in $\mathrm{km\,s^{-1}}$

tween the exposures is the dominant factor. Since the low signal to noise ratio of single exposures makes a position estimation of isolated single absorption features unreliable, in the further analysis only shifts between whole exposures were corrected.

The exposures were aligned according to the calculated velocity shift. Exposure 4 was used as a reference for the lower wavelength range and exposure 2 for the higher wavelength range. To test the method for self consistency not just the direct cross correlation between the spectra was used but also indirect measurements using a third exposure. The difference between $f \star g$ and $f \star h$ is also a measure of the shift between g and h, using f as a probe. Taking each available exposure as a probe between two other exposures in addition to the direct measurement gives a sample of 16 values for the lower, and six values for the higher wavelength part.

Table 4.12: Shifts between coadded spectra of different observation settings.

Setting	$\Delta v\,[\mathrm{km\,s^{-1}}]$
BLUE 390 - BLUE 437	0.22
BLUE 437 - RED 580L	-0.05
RED 580U - RED 760L	0.84

After the coaddition of the different exposures the spectrum consists of six parts, some of which are overlapping. To create the highest signal to noise ratio, the procedure was repeated using the overlapping parts of the different settings. The two gaps between RED 580L and RED 580U and between RED 760L and RED 760U prevent the whole spectrum from being aligned with this method.

As a first step the shift between BLUE 390 and BLUE 437 was determined, using the cross correlation method. BLUE 437 was used as reference and BLUE 390 was accordingly shifted for coaddition. In the next step a cross correlation was calculated between the BLUE 437 and the RED 580L spectra. There was no measurable shift between these two parts of the spectrum. There is a small overlap between BLUE 437 and RED 580U so that the spectrum is without a real gap between RED 580L and RED 580U. However, the overlap has no visible lines, so a cross correlation is not possible. If there is a shift between RED 580L and RED 580U it is not possible to measure it directly.

As a final step a cross correlation between RED 580U and RED 760L was calculated and RED 760L accordingly shifted and coadded. There is another gap between RED 760L and RED 760U that cannot be measured directly. Table 4.12 shows the shifts between the coadded spectra of the different observation settings.

4.3.2 SIDAM

Fe II 1608 of the system at $z = 1.58$ is covered by BLUE 390 and BLUE 437. All other Fe II transitions are covered by RED 580U and RED 760L. Because of the gap between RED 580L and RED 580U the re-

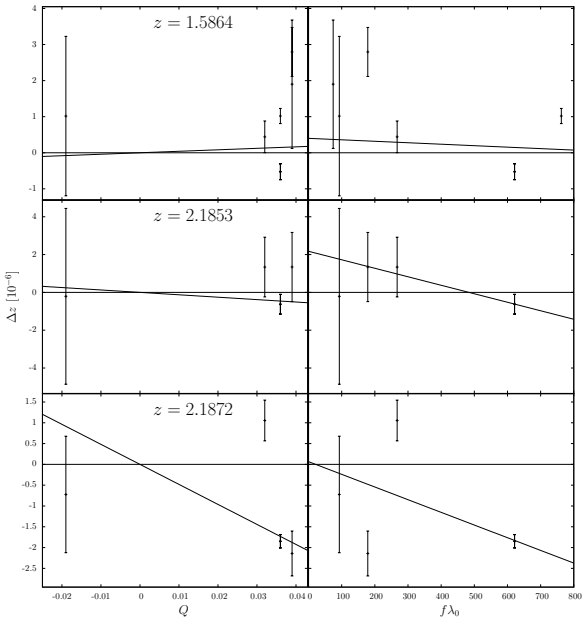

Figure 4.10: Line shift analysis of the 2011 data of HE0001-2340

sults are only valid if there is no shift between the upper and lower part of RED580.

As in sect. 4.2.1, the $z = 1.59$ system was fitted as a one component feature. The regression analysis with all six transitions gives $\Delta\alpha/\alpha = (-0.1 \pm 0.7) \cdot 10^{-5}$. Using just Fe II 2374 in comparison with Fe II 1608 gives $\Delta\alpha/\alpha = (-0.3 \pm 0.8) \cdot 10^{-5}$. Figure 4.10 shows the line shift analysis for this case. A 5σ offset between the strong transitions is present ($\Delta v = 0.18\,\mathrm{km\,s^{-1}}$), but no direct correlation of transition strength and position shift can be seen.

The system at $z = 2.18$ has a lower coverage as the $z = 1.59$ system. Fe II 1608 is covered by RED 580L, Fe II 2344 by RED 760L, Fe II 2374 and Fe II 2383 fall into a data gap, while Fe II 2587 and Fe II 2600 are covered by RED 760U. The data quality is lower than in the previous case. Furthermore the system stretches over two data gaps, between the two RED580 parts and the two RED760 parts. Again the results depend on no shift being present between the upper and lower part of the red arm of the spectrograph.

The first part of the system at $z = 2.1853$ gives $\Delta\alpha/\alpha = (0.2 \pm 1.3) \cdot 10^{-5}$ when using all four available transitions in a regression analysis. A comparison of only Fe II 1608 and Fe II 2587 gives $\Delta\alpha/\alpha = (-0.4 \pm 1.3) \cdot 10^{-5}$.

The second part of the system at $z = 2.1872$ gives an apparently positive result of $\Delta\alpha/\alpha = (0.8 \pm 0.4) \cdot 10^{-5}$ using all transitions. Figure 4.10 shows that the regression line is influenced by the strongly shifted Fe II 2344. Omitting this line would give $\Delta\alpha/\alpha = (0.3 \pm 0.4) \cdot 10^{-5}$. Using only Fe II 2587 in comparison with Fe II 1608 gives $\Delta\alpha/\alpha = (0.4 \pm 0.4) \cdot 10^{-5}$.

The importance of a stable wavelength calibration system is evident. The effort done here to correct the shifts between individual exposures by cross correlation, can just lessen this error to a certain degree. As a comparison the α variation analysis was also done using directly coadded spectra. The $z = 1.59$ system gives $\Delta\alpha/\alpha = (-0.8 \pm 0.6) \cdot 10^{-5}$ using all transitions in a regression analysis and $\Delta\alpha/\alpha = (0.4 \pm 0.8) \cdot 10^{-5}$ using only Fe II 1608 and Fe II 2374. The $z = 2.1853$ system gives $\Delta\alpha/\alpha = (2.6 \pm 1.1) \cdot 10^{-5}$ using all transitions in a regression analysis and $\Delta\alpha/\alpha = (1.3 \pm 1.2) \cdot 10^{-5}$ using only Fe II 1608 and Fe II 2587. The $z = 2.1872$ system gives $\Delta\alpha/\alpha = (2.9 \pm 0.3) \cdot 10^{-5}$ using all transitions in a regression analysis and $\Delta\alpha/\alpha = (1.9 \pm 0.3) \cdot 10^{-5}$ using only Fe II 1608 and Fe II 2587.

Table 4.13 shows the results of the α variation measurements for the 2004 data set, for both methods of co-added data of the 2009 data set, and the result by Agafonova et al. (2011). For the $z = 1.59$ system the values in the table are based on a comparison of Fe II 1608 and Fe II 2374, except the value by Agafonova et al. (2011), which is based on a comparison of Fe II 1608 and Fe II 2383. The values for the $z = 2.19$ system are based on a comparison of Fe II 1608 and Fe II 2587 in our analyses and on a comparison of Fe II 1608 and Fe II 2344 in the analysis by Agafonova et al. (2011).

Figure 4.11 shows a direct comparison between the 2004 and the 2009 data set. Fe II 2383 is shown for the $z = 1.59$ system and Fe II 2344 for the $z = 2.18$ system, either being the strongest transition that is available in both data sets. The plots show a slight difference in the positioning of the components of the two component feature at $z = 2.1871$.

The statistical error has not improved with the new data. The results of the α variation calculations, however, differ significantly. All three results

Table 4.13: Results of $\Delta\alpha/\alpha$ measurements for different data sets of HE0001-2340

redshift	$\Delta\alpha/\alpha$ $[10^{-5}]$			
	2004	2009_{cc}[1]	2009_{dc}[2]	2011_{Ag}[3]
1.5864	1.5 ± 0.8	-0.3 ± 0.8	0.4 ± 0.8	0.1 ± 1.1
2.1853	-0.7 ± 1.0	-0.4 ± 1.3	1.3 ± 1.2	
2.1872	1.6 ± 0.4	0.4 ± 0.4	1.9 ± 0.3	1.0 ± 0.5[4]

[1] Exposures co-added after cross correlation
[2] Exposures co-added directly
[3] Result by Agafonova et al. (2011)
[4] Combined value for the $z = 2.1853$ and the $z = 2.1872$ systems

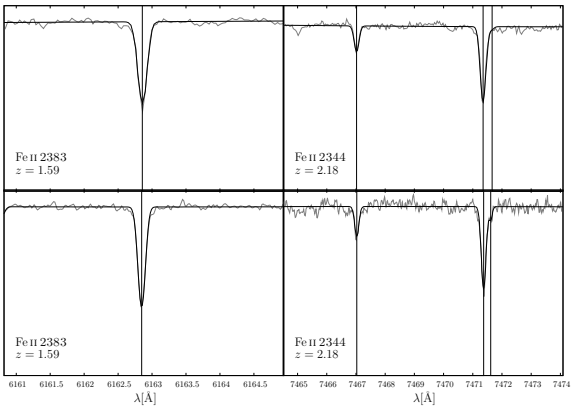

Figure 4.11: Comparison of 2004 and 2009 data of HE0001-2340 Fe II 2383 at $z = 1.59$ and Fe II 2344 at $z = 2.18$. The fitted line profile is plotted over the original spectrum. The best fit line positions are marked with vertical lines.

of the 2009 data set are in agreement with each other and with a no variation model. The 2004 data, however, gives a positive result of nearly 2σ significance. For the $z = 2.1853$ system, the result from the 2004 data set is in agreement with the result from our cross correlated data set. For the second part of the system however, the 2004 data show a result that is comparable to the directly co-added data set. The difference between the cross correlated data and the directly co-added data of the 2009 data set is similar for both subsystems at $z = 2.19$.

Because the second part of the $z = 2.19$ system is stronger, the result by Agafonova et al. (2011) is mainly influenced by this part. They just used Fe II 2344 in comparison with Fe II 1608. Though the result looks similar to ours, it is actually in strong contrast to our analysis, as can be seen in Fig. 4.10. Using just Fe II 2344 in comparison with Fe II 1608 would give $\Delta\alpha/\alpha = (-0.5 \pm 0.4) \cdot 10^{-5}$ with our data. The difference is equivalent to a differential position shift of Fe II 2344 in comparison with Fe II 1608 of $\Delta v \approx 0.4\,\mathrm{km\,s^{-1}}$. The difference is of the same order of magnitude as the amount the different parts of the spectrum were shifted according to the cross correlation calculations.

This analysis shows that with different data sets and with different methods of co-adding the data, significantly different results are found. A stable wavelength calibration system is a requirement to get consistent results.

4.4 HE2217-2818 2011 data

As part of the ESO Large Program for testing fundamental constants a new observation of the quasar HE2217-2818 was made. This gives another opportunity to study the improvements that can be made with better data quality compared to the 2004 data. The $z = 1.69$ system, as the only system in the quasar where a SIDAM method is applicable, was re-analysed.

As in the analysis of the Large Program 2004 data of this quasar, the system is separated into two distinct parts. The first part, at $z = 1.6910$, has at least six components. The second part, at $z = 1.6925$, has at least nine components. Figure 4.12 shows a comparison of the best fit of Fe II 2383 for the 2004 and the 2011 data set. Components 1, 8 and 18 are not used in the analysis because they are too weak to show in Fe II 1608 and separated enough not to influence the line positioning of the remaining system.

Figures 4.13 and 4.14 show the spectra and the corresponding fits for the first and the second system, respectively. It can be seen that Fe II 2344 is affected by blends with telluric lines in both parts of the system. It is thus excluded from the analysis.

The line shift analysis (Fig. 4.15) shows a shift of Fe II 2600 ($\Delta v = 0.2\,\mathrm{km\,s^{-1}}$) in comparison to the other transitions in the first part of the system. Figure 4.13 indicates that there might be a slight blend that could be responsible for this shift. Using just Fe II 2374 in comparison to Fe II 1608 would give $\Delta\alpha/\alpha = (-0.1 \pm 0.5) \cdot 10^{-5}$, while using all transi-

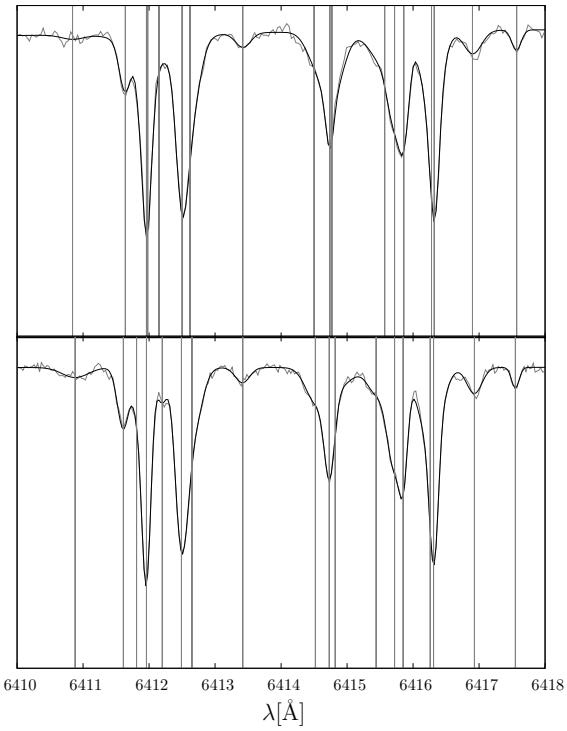

Figure 4.12: Comparison between the best fit of Fe II 2382 in the 2004 (top) and 2011 (bottom) data of the $z = 1.69$ system in HE2217-2818.

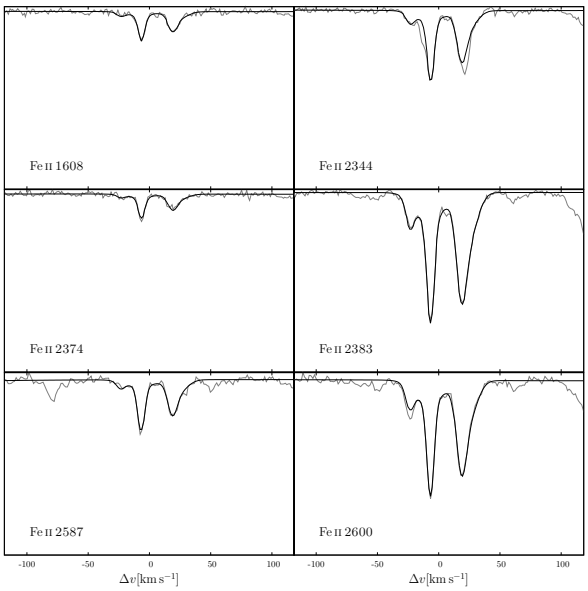

Figure 4.13: Original spectrum and best fit of Fe II at $z = 1.6910$ in the spectrum of HE2217-2818

tions, except the apparently blended Fe II 2344 and Fe II 2600 would give $\Delta\alpha/\alpha = (0.1 \pm 0.4) \cdot 10^{-5}$, while all transitions would give $\Delta\alpha/\alpha = (0.5 \pm 0.4) \cdot 10^{-5}$.

The second part of the system shows a position shift between the two weaker transitions on the one hand and the stronger transitions on the other hand. There is no strong correlation between line position and transition strength (Fig. 4.15). A slight blend of Fe II 2587 could explain the position offset between this transition and the other weak transitions. Using just Fe II 2374 in comparison to Fe II 1608 gives $\Delta\alpha/\alpha = (0.4 \pm 0.7) \cdot 10^{-5}$. Excluding the apparently blended Fe II 2344 and Fe II 2586 gives $\Delta\alpha/\alpha = (1.1 \pm 0.6) \cdot 10^{-5}$, while using all transitions would give $\Delta\alpha/\alpha = (1.0 \pm 0.5) \cdot 10^{-5}$.

The first two rows of Table 4.14 show the results of the α variation calculations for the 2004 and the 2011 data. A comparison of line positions of Fe II 1608 and Fe II 2344 gave the similar results in both data sets. Despite the higher resolution, the statistical error of the results has not increased significantly with the new data. Both data sets show a position offset between stronger and weaker transitions; in the new data fit it is reduced by about 50%. Though the main improvement is a higher security in wavelength calibration, the higher resolving power also decreases the danger of a wrong line decomposition.

Figure 4.12 shows that the best fit of the $z = 1.69$ system for the old and the new data gives different positions of the components in unresolved structures. Since there is no distinct strong one component feature, a direct comparison of single line positions is not possible.

To further evaluate the influence of wavelength calibration and line decomposition problems, a simultaneous fit of the 2004 and the 2011 data was made. While the column densities N, the Doppler parameters b, and the separations between the components were fitted simultaneously for all transitions, the positions of the systems in the old and new data sets were fitted individually. In this way position differences can be studied without the bias of a different line decomposition. Table 4.15 shows the best fit parameters for the 2004 data, the 2011 data and the simultaneous fit. Results of the corresponding α variation measurement are shown in the

Table 4.14: Comparison of results of the α variation analysis using all transitions in a regression analysis and comparing just Fe II 1608 with Fe II 2374 for the 2004 and the 2011 data of HE2217-2818.

	2004 Data		2011 Data	
z	$\Delta\alpha/\alpha_{reg}[10^{-5}]$	$\Delta\alpha/\alpha_{weak}[10^{-5}]$	$\Delta\alpha/\alpha_{reg}[10^{-5}]$	$\Delta\alpha/\alpha_{weak}[10^{-5}]$
1.6910	0.2 ± 0.4	0.4 ± 0.5	0.5 ± 0.4	-0.1 ± 0.5
1.6925	1.5 ± 0.6	0.0 ± 0.7	1.0 ± 0.5	0.4 ± 0.7
1.6910	-0.4 ± 0.4	-0.1 ± 0.5	0.5 ± 0.4	0.0 ± 0.5
1.6925	1.3 ± 0.3	-0.4 ± 0.5	1.0 ± 0.5	0.3 ± 0.7

The first two rows show the results for individual fits of each data set. The last two rows shows the results for a simultaneous fit of the two data sets.

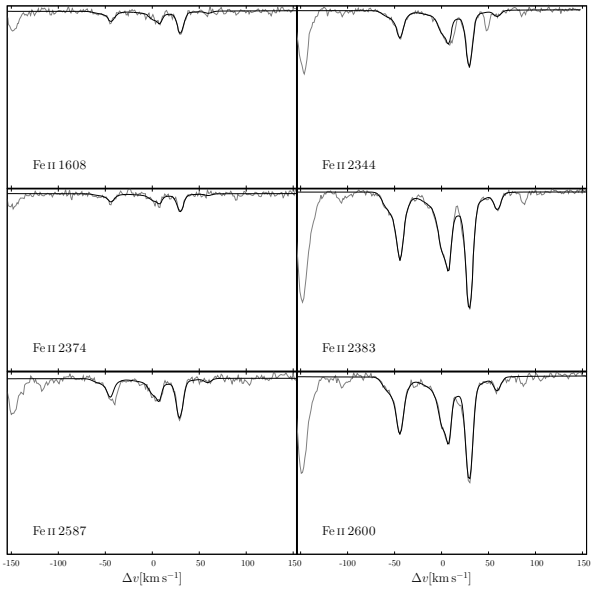

Figure 4.14: Original spectrum and best fit of Fe II at $z = 1.6925$ in the spectrum of HE2217-2818

two last rows of Table 4.14. Both fits give nearly the same result for the 2011 data set and only small differences for the 2004 data. This indicates that the line decomposition is mainly influenced by the higher resolution data. Nevertheless the best fit parameters for column densities N and Doppler parameters b of the simultaneous fit are similar to those of the 2004 data in the first part of the system (see Tab. 4.15). The resulting α variation calculations of the different fits of the 2004 data set are well within the 1σ confidence level of each other, indicating that in this case the line decomposition has only a small influence on the results.

Using a simultaneous fit of the two data sets allow a direct comparison of the line position placement. Table 4.16 shows corresponding position shifts of the two subsystems between the 2004 and the 2011 data set for each transition. There is not only a total shift between the data sets, but also a differential shift between different transitions of several hundred $\mathrm{m\,s^{-1}}$. It is noticeable that position differences between the two data are higher in the second subsystem. For the stronger transitions, Fe II 2382 and Fe II 2600, however, the shifts are similar in the two subsystems. This indicates that the apparent differences between the two subsystems are rather a result of line decomposition problems than small scale wavelength calibration errors. The line decomposition is mainly given by the stronger transitions. For these the fit gives the best approximation of the of the real line shape. Depending on the actual line profile this approximation can be inaccurate for the weaker transitions (compare sect. 3.4.2), resulting in different positions offsets between the two data sets for the two subsystems.

Molaro et al. (2013) have recently done an analysis of the same data. Their main focus lay on using the MM method, but they have also analysed the $z = 1.69$ system, using the SIDAM method. Using all six Fe II transitions, and including the α variation as fit parameter, they got a comparable result of $\Delta\alpha/\alpha = (0.1 \pm 0.3) \cdot 10^{-5}$. They excluded regions with possible blends with telluric features by masking them and just fitting the apparently unaffected parts of the transitions. They use a 32 component model to get an acceptable χ^2 value. We could not reproduce that effect. Adding further components

Table 4.15: Best fit parameters of the HE2217-2818 $z = 1.69$ Fe II system for the 2004 data, the 2011 data, and a simultaneous fit of both data sets.

2004 Data			2011 Data			Simultaneous Fit			
z	N	b^1	z	N	b^1	z_{2004}	z_{2011}	N	b^1
1.690839	11.93 ± 0.07	4.7 ± 0.7	1.690829	12.07 ± 0.02	5.0 ± 0.3	1.690834	1.690833	12.06 ± 0.04	5.0 ± 0.7
1.690974	12.54 ± 0.05	4.4 ± 0.5	1.690912	11.58 ± 0.10	2.4 ± 0.8	1.690909	1.690908	11.53 ± 0.19	1.5 ± 1.5
1.690982	12.38 ± 0.20	0.6 ± 0.1	1.690974	12.72 ± 0.01	3.0 ± 0.1	1.690976	1.690974	12.71 ± 0.01	3.2 ± 0.2
1.691057	12.33 ± 0.10	24.9 ± 5.0	1.691075	11.75 ± 0.03	4.3 ± 0.6	1.691079	1.691077	11.74 ± 0.12	4.5 ± 2.1
1.691203	12.51 ± 0.12	4.5 ± 0.5	1.691199	12.62 ± 0.04	4.8 ± 0.2	1.691202	1.691200	12.59 ± 0.12	4.9 ± 0.5
1.691254	12.32 ± 0.19	7.9 ± 1.6	1.691265	12.29 ± 0.09	8.3 ± 0.8	1.691259	1.691258	12.33 ± 0.24	8.6 ± 2.1
1.692043	11.77 ± 0.42	9.0 ± 2.9	1.692051	11.95 ± 0.62	9.4 ± 3.0	1.692015	1.692010	11.03 ± 13.57	0.1 ± 0.3
1.692141	11.92 ± 0.17	2.6 ± 1.5	1.692139	12.20 ± 0.06	4.0 ± 0.3	1.692123	1.692117	12.35 ± 0.70	13.2 ± 1.8
1.692155	12.34 ± 0.16	10.4 ± 1.8	1.692178	11.96 ± 0.69	14.5 ± 12.0	1.692143	1.692138	12.05 ± 0.11	3.2 ± 0.9
1.692491	12.15 ± 0.20	13.5 ± 2.4	1.692434	11.80 ± 0.21	8.0 ± 2.9	1.692468	1.692462	12.03 ± 1.03	12.2 ± 16.9
1.692553	12.17 ± 0.37	5.8 ± 2.9	1.692554	12.42 ± 0.02	6.6 ± 1.0	1.692552	1.692546	12.23 ± 0.70	5.5 ± 4.5
1.692614	12.19 ± 0.30	4.0 ± 1.1	1.692610	12.10 ± 0.10	2.8 ± 0.4	1.692613	1.692608	12.22 ± 0.25	3.6 ± 1.0
1.692789	12.41 ± 0.09	9.0 ± 1.3	1.692779	12.42 ± 0.02	10.3 ± 0.5	1.692786	1.692780	12.42 ± 1.03	9.8 ± 1.7
1.692807	12.42 ± 0.08	3.0 ± 0.5	1.692803	12.49 ± 0.01	2.8 ± 0.1	1.692808	1.692803	12.46 ± 0.06	2.8 ± 0.3
1.693051	11.78 ± 0.05	8.2 ± 1.1	1.693061	11.78 ± 0.03	6.9 ± 0.7	1.693058	1.693052	11.79 ± 0.09	7.7 ± 1.8

[1] $[\mathrm{km\,s^{-1}}]$

Table 4.16: Position shifts between the 2011 and the 2004 data of the first and the second subsystem at $z = 1.69$.

Transition	Δv_1 $[\mathrm{km\,s^{-1}}]^1$	Δv_2 $[\mathrm{km\,s^{-1}}]^2$
Fe II 1608	0.11 ± 0.19	0.55 ± 0.22
Fe II 2344	0.17 ± 0.08	0.65 ± 0.07
Fe II 2374	0.14 ± 0.21	0.80 ± 0.30
Fe II 2383	0.60 ± 0.04	0.52 ± 0.04
Fe II 2587	0.10 ± 0.11	0.67 ± 0.11
Fe II 2600	0.30 ± 0.04	0.31 ± 0.05

[1] $z = 1.6910$
[2] $z = 1.6925$

to our 18 component model did not decrease the χ^2 value significantly, neither did it change the value of the resulting α variation by a significant amount.

4.5 The Australian Dipole

Webb et al. (2010) reported a 4.2σ detection of a spatial variation of α along a dipole axis in the direction of (17.5 ± 0.9) h right ascension and $(-58 \pm 9)^\circ$ declination in equatorial coordinates. We used a χ^2 analysis to test how good our results fit the dipole model

$$\Delta\alpha/\alpha = A\, r \cos\theta,$$

where A is the Dipole amplitude, r the look back time and θ the angle between the line of sight towards the quasar and the dipole axis. For the systems in the spectra of HE0001-2340 and HE2217-2128 we used the results of the newer data sets. For a model with no variation we get $\chi^2 = 1.41$, while the Australian Dipole gives $\chi^2 = 1.49$. The data slightly favours a model with no spatial variation. The difference is, however, not statistically significant. For this calculation we just used the statistical errors of the α variation calculations. Since the main error source is expected to be systematic, the real significance is even lower.

Figure 4.16 shows our values of $\Delta\alpha/\alpha$ over the dipole axis. The straight lines show a model with no spatial variation and the model by Webb et al. (2010), respectively. The abscissa shows a combination of look-back time and the angle between the quasar sightline and the dipole axis. The look-back time was calculated using a ΛCDM cosmology[1]. The quasar coordinates were taken from the SIMBAD Astronomical Database[2]. For systems with different subsystems each subsystem was used individually for the χ^2 calculations and a weighted mean was used for the plot. Only the positive side of the abscissa could be traced because the data used in this work is restricted to the southern hemisphere.

[1] $H_0 = 71$, $\Omega_M = 0.27$, $\Omega_{VAC} = 0.73$
[2] http://simbad.u-strasbg.fr/simbad/

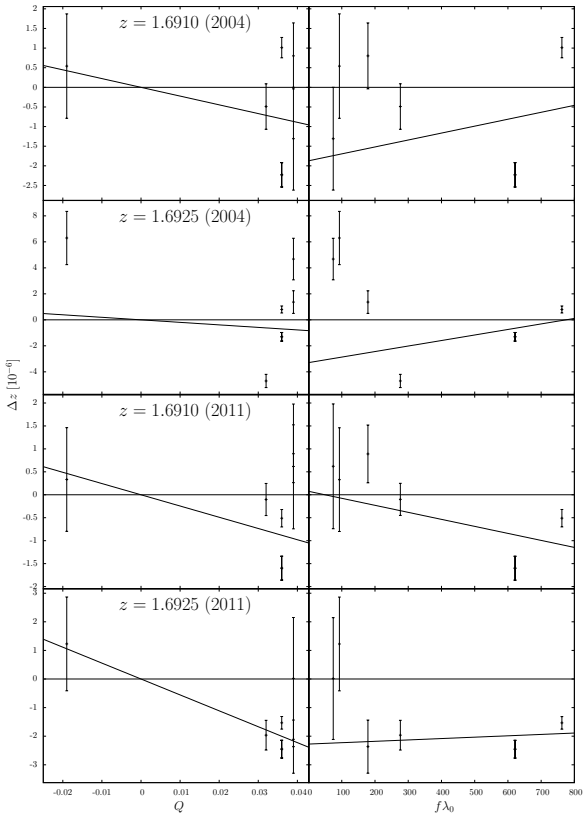

Figure 4.15: Line shift analysis of HE2217 for 2004 and 2011 data.

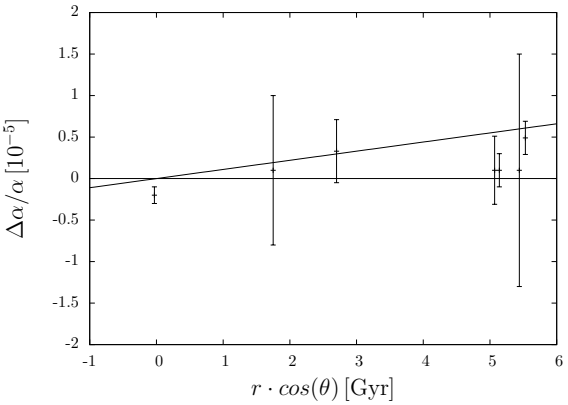

Figure 4.16: $\Delta\alpha/\alpha$ along the Australian Dipole. r is the look-back time and θ the angle between the line of sight towards the quasar and the dipole axis. The straight line shows the result by Webb et al. (2010).

4.6 Analysis of MgII systems

4.6.1 Precision of position measurements

A good test for the precision of line position measurements are ions with close lying transitions that have no differential sensitivities to fundamental constants. Valid candidates are Mg II and C IV because of their high abundance in quasar spectra. Since Mg II transitions are of importance for the still widely used Many Multiplet method, the precision of position measurements of this ion is of particular interest. The different strengths of Mg II 2796 ($f\lambda_0 = 1719.8$) and Mg II 2804 ($f\lambda_0 = 857.9$) (Tab. 2.1) could create position shifts due to line decomposition problems. Usually a simultaneous position fit would be used which is mainly influenced by the stronger Mg II 2804 transition. An independent position fit of Mg II 2796 can be used to detect problems with line position fits because of unresolved saturation, line decomposition problems or wavelength calibration.

98 Mg II systems were analysed in the spectra of HE0515-4410 and the 19 quasars of the ESO Large Program 'The cosmic evolution of the IGM' from 2004. The fitting was done with the same mechanism as in previous sections. Figure B.5 shows the fits and the original data. Table 4.17 shows the name of the quasar, the redshift z of the system, the velocity shift Δv between Mg II 2796 and Mg II 2804, and in the last column, the number of fitted components.

Several systems have position offsets of a few hundred meters per second with a significance of up to 10σ. 21 of the 98 analysed systems have position shifts between the two Mg II transitions that are within 1σ of the statistical error. The highest precision should be achievable with systems consisting of a single symmetric component. Of the 25 available one component systems, 32% have position offsets smaller than their 1σ confidence level. The average σ distance between the transitions

$$\bar{\sigma} = \frac{1}{n}\sum_{i=1}^{n}\frac{|\Delta v_i|}{\sigma_i},$$

where n is the number of systems, for the whole sample is $\bar{\sigma} = 3.3$. For the 25 one components systems the value decreases to $\bar{\sigma} = 2.3$.

Table 4.17: Velocity shifts between Mg II 2796 and Mg II 2804.

Quasar	z	$\Delta v\,[\mathrm{km\,s^{-1}}]$	#		Quasar	z	$\Delta v\,[\mathrm{km\,s^{-1}}]$	#	
HE0001-2340	0.2706	0.262 ± 0.052	7	s	HE2217-2818	1.2003	0.124 ± 0.090	3	
HE0001-2340	0.2729	0.043 ± 0.130	1		HE2217-2818	1.5558	0.116 ± 0.037	5	
HE0001-2340	0.4521	-0.315 ± 0.123	1		HE2217-2818	1.6277	0.166 ± 0.037	5	
HE0001-2340	0.4524	0.020 ± 0.061	2		HE2217-2818	1.6918	0.160 ± 0.025	16	s
HE0001-2340	0.9487	-0.499 ± 0.532	1		HE2347-4342	1.4054	-0.080 ± 0.086	2	
HE0001-2340	0.9493	-0.194 ± 0.046	10		HE2347-4342	1.7962	-0.036 ± 0.056	2	s
HE0001-2340	1.5860	0.368 ± 0.037	6	s	PKS0237-23	1.6358	-0.006 ± 0.042	4	
HE0001-2340	1.6515	0.234 ± 0.061	1		PKS0237-23	1.6373	0.123 ± 0.060	6	
HE0001-2340	2.1839	0.056 ± 0.058	9		PKS0237-23	1.6574	0.060 ± 0.026	9	s
HE0001-2340	2.1855	-0.110 ± 0.086	3		PKS0237-23	1.6717	-0.628 ± 0.022	11	s
HE0001-2340	2.1870	0.351 ± 0.067	3		PKS0329-255	0.4718	0.798 ± 0.356	1	
HE0141-3932	0.3401	0.733 ± 0.096	3		PKS0329-255	0.4724	0.260 ± 0.382	1	
HE0151-4326	0.6632	-0.171 ± 0.036	5	s	PKS0329-255	0.9929	0.122 ± 0.108	10	
HE0515-4414	0.2220	0.798 ± 1.144	1		PKS1448-232	1.5855	0.234 ± 0.075	1	
HE0515-4414	0.2222	0.194 ± 0.275	5		PKS2000-330	1.1764	0.209 ± 0.135	4	
HE0515-4414	0.4291	0.333 ± 0.076	1		PKS2000-330	1.2499	-0.284 ± 0.173	1	
HE0515-4414	1.1472	-0.164 ± 0.042	6		PKS2000-330	2.0330	-0.813 ± 0.094	3	s
HE0515-4414	1.1478	-0.025 ± 0.101	4		Q0002-422	1.4465	0.430 ± 0.172	2	
HE0515-4414	1.1485	-0.006 ± 0.200	6		Q0002-422	1.5415	-0.359 ± 0.057	5	s
HE0515-4414	1.1491	-0.203 ± 0.039	2	s	Q0002-422	2.1681	-0.339 ± 0.123	4	
HE0515-4414	1.1495	0.043 ± 0.123	2		Q0002-422	2.3017	-0.167 ± 0.080	6	s
HE0515-4414	1.1499	0.048 ± 0.072	2		Q0109-3518	0.3271	0.246 ± 0.103	2	
HE0515-4414	1.1510	0.326 ± 0.046	10	s	Q0109-3518	0.4142	-0.608 ± 0.325	1	
HE0940-1050	1.7890	0.398 ± 0.046	14	s	Q0109-3518	0.4144	0.266 ± 0.063	2	s
HE0940-1050	1.7907	0.518 ± 0.093	4		Q0109-3518	0.7696	0.176 ± 0.114	1	
HE1122-1649	0.6809	0.089 ± 0.085	2		Q0109-3518	1.1827	0.057 ± 0.083	2	s
HE1122-1649	0.6820	-0.232 ± 0.061	7	s	Q0109-3518	1.1830	0.344 ± 0.168	2	
HE1122-1649	0.8056	-0.135 ± 0.051	4		Q0109-3518	1.3497	0.073 ± 0.022	18	s
HE1122-1649	0.8065	-0.064 ± 0.150	1		Q0122-380	0.4434	0.346 ± 0.091	5	
HE1122-1649	1.2334	-0.024 ± 0.042	4		Q0122-380	0.8221	-0.084 ± 0.056	2	
HE1158-1843	0.5060	-0.677 ± 0.210	2		Q0122-380	0.8241	-0.582 ± 0.131	2	
HE1158-1843	0.8181	0.275 ± 0.162	3		Q0122-380	0.8245	0.324 ± 0.169	5	
HE1341-1020	0.8727	0.116 ± 0.040	7	s	Q0122-380	0.8578	0.115 ± 0.057	4	
HE1341-1020	1.2767	-0.072 ± 0.053	7	s	Q0122-380	0.8593	-0.567 ± 0.054	1	s
HE1341-1020	1.2778	-0.180 ± 0.051	1	s	Q0122-380	0.8603	0.274 ± 0.167	1	
HE1341-1020	1.2786	0.476 ± 0.216	2		Q0122-380	0.9096	-0.219 ± 0.131	1	
HE1341-1020	1.2791	0.486 ± 0.423	2		Q0122-380	1.2434	0.263 ± 0.054	3	s
HE1341-1020	1.9195	0.107 ± 0.061	2	s	Q0329-385	0.7631	0.301 ± 0.043	10	s
HE1341-1020	2.1474	0.343 ± 0.091	4		Q0329-385	0.9296	0.189 ± 0.145	2	
HE1347-2457	1.4397	0.312 ± 0.030	9	s	Q0329-385	0.9709	-0.103 ± 0.087	1	
HE1347-2457	1.5082	0.046 ± 0.042	3		Q0329-385	1.4373	0.009 ± 0.433	1	
HE1347-2457	1.7529	0.190 ± 0.070	1		Q0329-385	1.4379	-0.144 ± 0.075	3	
HE2217-2818	0.5995	-0.191 ± 0.111	2		Q0329-385	1.4386	-1.112 ± 0.125	3	
HE2217-2818	0.7865	0.064 ± 0.085	5		Q0453-423	0.9084	0.365 ± 0.037	9	s
HE2217-2818	0.9404	-0.061 ± 0.183	1		Q0453-423	1.0391	0.402 ± 0.185	1	
HE2217-2818	0.9408	-0.087 ± 0.082	2		Q0453-423	1.0396	0.246 ± 0.079	2	
HE2217-2818	0.9424	0.286 ± 0.039	7		Q0453-423	1.6301	0.180 ± 0.085	5	
HE2217-2818	1.1990	0.712 ± 0.979	1		Q0453-423	1.6308	-0.170 ± 0.198	2	
HE2217-2818	1.1999	0.313 ± 0.273	1		Q0453-423	1.8584	0.503 ± 0.061	1	

The number of components are stated in the last column. Systems that show signs of saturation are marked by s.

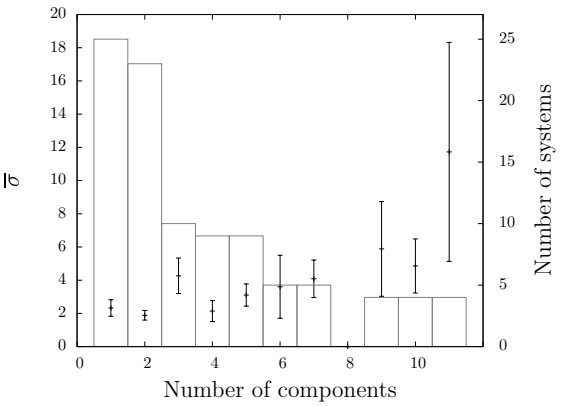

Figure 4.17: Average σ distance between Mg II 2796 and Mg II 2804 over number of components (left axis). In grey the number of available systems is indicated (right axis).

Of the 98 systems at least 26 have a saturated Mg II 2796 line, 12 of them show resolved saturation and 14 unresolved saturation, assuming that the line decomposition is correct. If any fitted feature is actually a close blend of two or more very narrow lines, the saturation would not be detected. The saturated systems are marked in Tab. 4.17 with the letter s in the last column. The average σ distance for the remaining 72 systems is $\bar{\sigma} = 2.2$. Using just the remaining 23 one component systems which do not show signs of saturation gives $\bar{\sigma} = 1.9$. Figure 4.17 shows $\bar{\sigma}$ for the number of fitted components, showing an increase with system complexity. The boxes (right axis) show the number of systems on which the value is based. The average position fit error for the whole sample would need to be increased by a factor 2.3 to have 67% of the system have their two Mg II transitions within 1σ of each other. For the not saturated one component sample the error seems to be underestimated by 50%. These systems can still have problems with line decomposition and unresolved saturation. Assuming that the underestimation of the error of the one component systems stems from wavelength calibration problems alone, this value can be used to correct the position fit errors of the full sample. After doing this, it is still necessary to increase the position fit error of each single measurement by another 50% for 67% of the position fit differences between Mg II 2796 and Mg II 2804 to be within their respective 1σ confidence levels. This underestimation of the position fit error can be associated with a wrong line decomposition due to system complexity. For the unsaturated sample this value decreases to 13%.

4.6.2 Isotope abundances

According to sect. 3.4.6 the data quality needed to detect a change of Mg II isotope abundances with the bisector method could be reached with the next generation of instruments. The analysis was, however, restricted to statistical errors. If unresolved line blends or a velocity substructure is present in a large fraction of systems, the prediction might not be valid. By averaging over a large sample, the spread created by noise will decrease. This is not the case for velocity substructure offsets if they are not Normal distributed. A comparison of a large data sample with the accuracy predictions from sect. 3.4.6 allows a quantification of this effect. Figure 4.18 shows bisectors of narrow separated Mg II lines from the spectra used in sect. 4.6.1. The bisector of Mg II 2796 and Mg II 2804 are plotted together. Several lines are present where the bisectors of the two transitions differ significantly. These are omitted from the analysis. From the bisector alone it is not possible to determine which of the lines, if any, is undistorted. Most of the bisectors show line asymmetries that are on a higher scale than the isotope structure could create. These are created by noise, unresolved line blends, or velocity substructure in the absorbing medium.

Figure 4.19 (l) shows the average bisector for a sample of 60 individual lines, in 30 systems at $0.3 < z < 2.2$. The grey lines show the standard deviation of the data. The dashed line indicates the best fit for isotope abundances (^{26}Mg II$\sim$ 60%, ^{25}Mg II$\sim$ 0%, ^{24}Mg II$\sim$ 40%). The spread of the bisectors at $0.7f$ is $\Delta v = 0.46\,\mathrm{km\,s^{-1}}$. The resolving powers of the data ranges between $45000 < R < 55000$ and the signal to noise ratio ranges between $40 < S/N < 140$ with an average at $\overline{S/N} \sim 80$. According to the simulations from sect. 3.4.6 the spread of the bisectors at $0.7f$ would be expected to be at $\Delta v = 0.08\,\mathrm{km\,s^{-1}}$for this data quality. Noise is only responsible for a small fraction of the line distortions. With a more careful line selection the result can be improved significantly. Figure 4.19 (r) shows the average bisector of 12 lines in the six most promising systems, three of which were

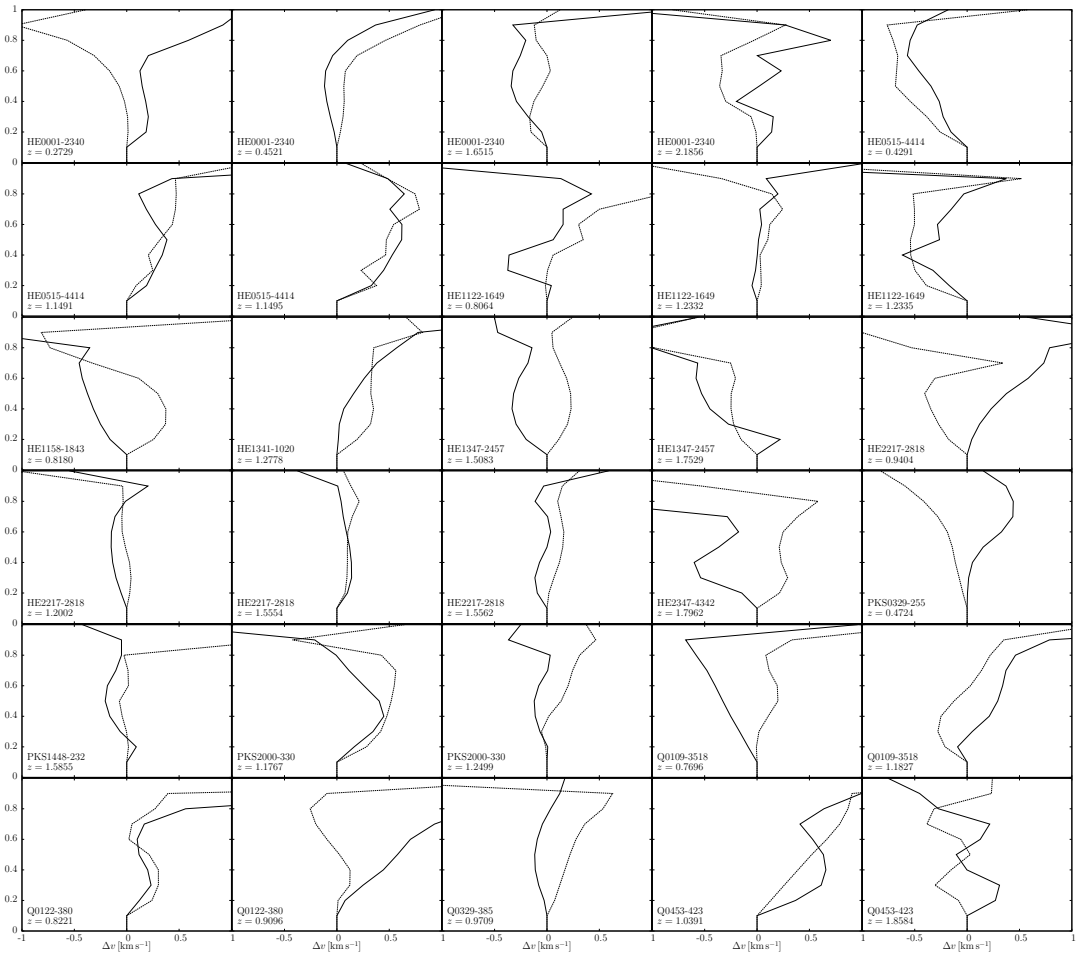

Figure 4.18: Bisectors of narrow Mg II lines. The solid curves represent Mg II 2796, the dashed curves Mg II 2804.

found in the spectrum of the quasar HE2217-2818. They are all located at a redshift of $1.2 < z < 1.7$. Again the grey lines show the standard deviation and the dashed line the best fit for isotope abundances (^{26}Mg II$\sim$ 60%, ^{25}Mg II$\sim$ 30%, ^{24}Mg II$\sim$ 10%). The spread of this data sample at $0.7f$ is $\Delta v = 0.13\,\mathrm{km\,s}$. When the errors created by noise σ_{stat} and by other sources of line distortion σ_{syst} are added quadratically $\sigma^2 = \sigma^2_{\mathrm{stat}} + \sigma^2_{\mathrm{syst}}$, the contribution of systematical sources is $\sigma_{\mathrm{syst}} = 0.1\,\mathrm{km\,s^{-1}}$. Assuming that line distortions by unresolved blends or velocity substructures are normally distributed, a statistical analysis would still be possible. The main difficulty would be to estimate an appropriate error for each measurement. Assuming a contribution of $\sigma_{\mathrm{syst}} = 0.1\,\mathrm{km\,s^{-1}}$ to the total error, the number of necessary systems (Table 3.5) would increase by $n_{\mathrm{total}} = n_{\mathrm{stat}} + \frac{\sigma^2_{\mathrm{syst}}}{\sigma^2}$, where σ is the required measurement accuracy.

The new data of the quasar HE2217-2818 has a higher resolution ($R \sim 65\,000$) than the 2004 data at a similar signal to noise ratio $S/N \sim 100$. Figure 4.20 shows a comparison of the bisectors of the three most symmetric Mg II features of the quasar HE2217-2818 for the 2004 and the 2011 data. The spread of the bisectors of all six lines at $0.7f$ is $\Delta v = 0.10\,\mathrm{km\,s^{-1}}$ in both data sets. In this small sample the spread of the bisectors did not decrease with the newer data. According to the simulations of sect. 3.4.6 the statistical spread of the bisec-

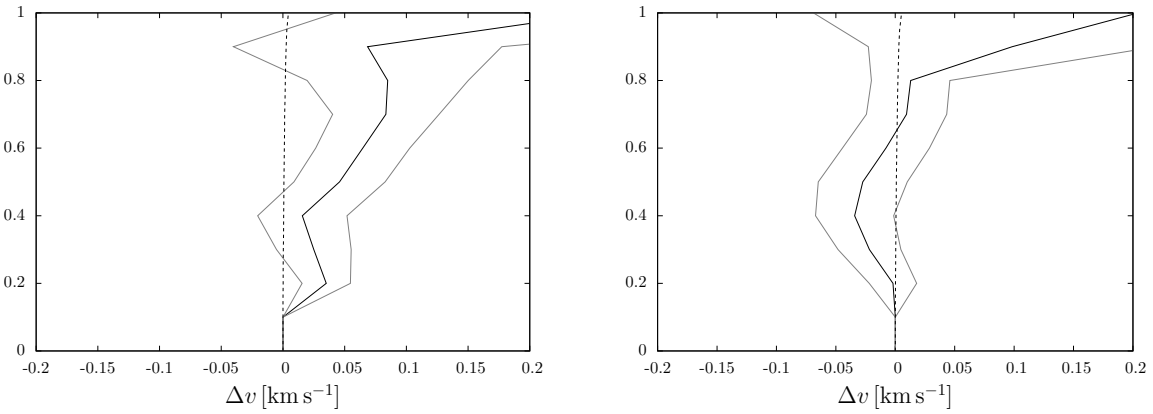

Figure 4.19: Average bisector of the sample of 60 lines (l) and the best sample of 12 lines (r). The grey lines indicate the standard deviation of the data. The dashed line shows the best fit for isotope abundances.

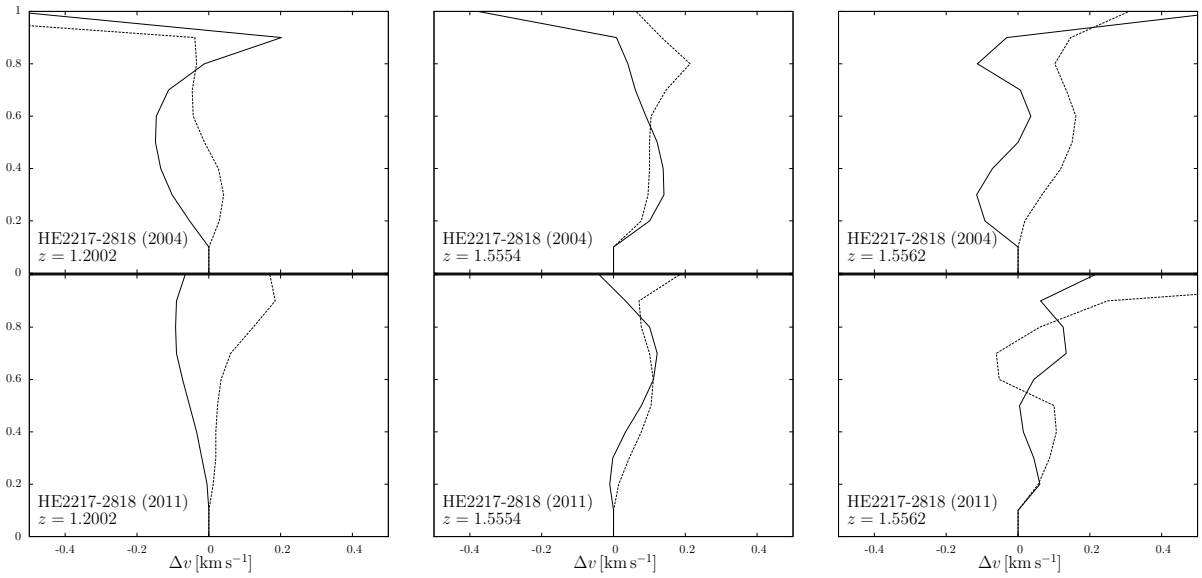

Figure 4.20: Comparison of best sample of Mg II bisectors in the new and old data set. The solid curves represent Mg II 2796, the dashed curves Mg II 2804.

tors at $0.7f$ should be at $\Delta v = 0.04\,\mathrm{km\,s^{-1}}$, leaving a fraction of $\Delta v = 0.09\,\mathrm{km\,s^{-1}}$ to systematical line distortions. Assuming that these systematical line distortions are normal distributed and thus can be handled as statistical in a large data set, the number of necessary systems for a data quality of $R = 100\,000$ and $S/N = 150$ would increase from $n_{\mathrm{stat}} = 5$ (Table 3.5) to $n_{\mathrm{total}} \approx 35$.

With the data quality achievable today, it is not possible to find changes in isotope abundances with the bisector method. The main problem is that every line has some intrinsic asymmetry that is possibly created by a velocity substructure of the absorbing medium or unresolved line blends. With the next generation of instruments, a large data set, and a careful line selection process, the accuracy of the method could become sufficient for the search for isotope abundance changes, assuming that the

systematical line distortion processes are approximately Normal distributed. Studying line shapes of absorption spectra of the interstellar medium over a longer time span would allow a more detailed analysis of a possible time variability of line shapes due to turbulent motion and give insight in the statistics of these processes.

Chapter 5

Discussion and outlook

The conflicting results about a variation of the fine-structure constant α have led to an active debate about systematic error sources. Though problems with wavelength calibration are a major concern (Molaro et al. 2008a; Griest et al. 2010; Wendt & Molaro 2011; Agafonova et al. 2011), it is not the only source of position shifts between different transitions. We could show in our simulations (chap. 3) that unresolved substructure, like very narrow line blends and unresolvable substructure like an underlying velocity field, can lead to errors in the α variation measurements that are on a similar scale as wavelength calibration errors. Though these effects lessen significantly when just using transitions of similar strength, a combination of unresolved blends and noise can still leave a bias of up to $\Delta v = 0.1\,\mathrm{km\,s^{-1}}$ (Fig. 3.13). The presence of continuous velocity fields in the absorbing medium can cause velocity shifts of comparable amounts. In the data analysed, about 50% of the observed systems showed signs of wavelength shifts possibly due to one of these mechanisms. While unresolved line blends could in principle be resolved with spectrographs of sufficiently high resolution, continuous velocity fields can create line shapes that are asymmetric even if fully resolved.

In the systems analysed here, there was no case where an increase of the number of fitted components would change the results significantly. In the few cases where differences did occur, there was no way of judging which value was to be preferred. Simulations have shown that an increase in the number of fitted components does not necessarily give better results (sect. 3.4). After a careful analysis of each system we found no significant evidence of a variation of α.

An analysis of Mg II systems, which are not sensitive to a variation of α, confirmed that discrepancies in line position fits occur regularly and that the fit errors are systematically underestimated. A differentiation between contributions of unresolved substructure and wavelength calibration or other error sources could be estimated by analysing systems of different complexity.

The line shift analysis (sect. 3.4.4) proved to be a useful tool to discern different sources of line position shifts and to create selection criteria for whole systems or single transitions. Position shifts due to line decomposition problems could clearly be recognised with this method. In some cases the bisector method (sect. 3.4.5) could be used to detect hidden line blends. The S/N of the available spectra was, however, too low for an efficient use of this method. With the next generation of instruments the bisector method can be put to better use to analyse line shapes and estimate their influence on line position fits.

The use of the bisector method to find changes in isotope abundances depends on the statistical distribution of line distortions due to unresolved blends or a velocity substructure. If these are approximately Normal distributed, a statistical analysis may be possible with the next generation of instruments (chs. 3.4.6, 4.6.2). A detailed analysis of the shapes of absorption lines in the interstellar medium could help to estimate the statistical distribution and spread of these processes.

A major progress in the field will be achieved with the next generation of instruments. The ESPRESSO spectrograph aims towards a wavelength accuracy of $10\,\mathrm{m\,s^{-1}}$ at a resolution of $R = 120\,000$ and will be linked to all four 8.4 m telescopes of the VLT (Mégevand et al. 2012). The use of a frequency comb will further improve the stability of

wavelength calibration. Using this technology, the CODEX spectrograph aims at a wavelength calibration stability on the level of cm^{-1} at a resolution of $R = 120\,000$ (Pasquini et al. 2010). It is designed to work on the upcoming 40 m telescope E-ELT (McPherson et al. 2012).

When the wavelength calibration uncertainty is reduced the main error source will be unresolved blends and velocity substructure, as shown in this work. The higher resolution of the upcoming spectrographs, combined with the possibility of getting a very good signal to noise ratio, using a combination of all four VLT telescopes or the E-ELT, will highly improve the possibility of resolving line blends and enable to further investigate the substructure of absorption lines. Since even with a resolution of $R = 120\,000$ the substructure of the absorption systems are not expected to be fully resolved and effects like a velocity substructure are unresolvable, the methods described in this work will be necessary in the next generation of data to reduce systematic effects.

Bibliography

Agafonova, I. I., Molaro, P., Levshakov, S. A., & Hou, J. L. 2011, A&A, 529, A28+

Aldenius, M. 2009, Physica Scripta Volume T, 134, 014008

Aller, L. H. 1963, Astrophysics. The atmospheres of the sun and stars

Aracil, B., Petitjean, P., Pichon, C., & Bergeron, J. 2004, A&A, 419, 811

Avelino, P. P., Esposito, S., Mangano, G., et al. 2001, Phys. Rev. D, 64, 103505

Avelino, P. P., Martins, C. J. A. P., Rocha, G., & Viana, P. 2000, Phys. Rev. D, 62, 123508

Bahcall, J. N., Sargent, W. L. W., & Schmidt, M. 1967, ApJ, 149, L11+

Bahcall, J. N. & Schmidt, M. 1967, Physical Review Letters, 19, 1294

Bahcall, J. N., Steinhardt, C. L., & Schlegel, D. 2004, ApJ, 600, 520

Battye, R. A., Crittenden, R., & Weller, J. 2001, Phys. Rev. D, 63, 043505

Bennett, C. L., Halpern, M., Hinshaw, G., et al. 1997, in Bulletin of the American Astronomical Society, Vol. 29, American Astronomical Society Meeting Abstracts, 1353

Berengut, J. C., Dzuba, V. A., Flambaum, V. V., & Marchenko, M. V. 2004, Phys. Rev. A, 70, 064101

Berengut, J. C., Flambaum, V. V., & Kozlov, M. G. 2005, Phys. Rev. A, 72, 044501

Bergström, L., Iguri, S., & Rubinstein, H. 1999, Phys. Rev. D, 60, 045005

Bize, S., Diddams, S. A., Tanaka, U., et al. 2003, Physical Review Letters, 90, 150802

Bize, S., Laurent, P., Abgrall, M., et al. 2005, Journal of Physics B Atomic Molecular Physics, 38, 449

Blatt, S., Ludlow, A. D., Campbell, G. K., et al. 2008, Physical Review Letters, 100, 140801

Chand, H., Srianand, R., Petitjean, P., & Aracil, B. 2004, A&A, 417, 853

Chand, H., Srianand, R., Petitjean, P., et al. 2006, A&A, 451, 45

Chengalur, J. N. & Kanekar, N. 2003, Physical Review Letters, 91, 241302

Coc, A., Nunes, N. J., Olive, K. A., Uzan, J.-P., & Vangioni, E. 2007, Phys. Rev. D, 76, 023511

Cowie, L. L. & Songaila, A. 1995, ApJ, 453, 596

Curran, S. J., Tanna, A., Koch, F. E., et al. 2011, A&A, 533, A55

Cyburt, R. H., Fields, B. D., Olive, K. A., & Skillman, E. 2005, Astroparticle Physics, 23, 313

Damour, T. & Dyson, F. 1996, Nuclear Physics B, 480, 37

Darling, J. 2003, Physical Review Letters, 91, 011301

Darling, J. 2004, ApJ, 612, 58

Dekker, H., D'Odorico, S., Kaufer, A., Delabre, B., & Kotzlowski, H. 2000, in Society of Photo-Optical Instrumentation Engineers (SPIE) Conference Series, Vol. 4008, Optical and IR Telescope Instrumentation and Detectors, ed. M. Iye & A. F. Moorwood, 534–545

Dirac, P. A. M. 1937, Nature, 139, 323

Dravins, D. 1982, ARA&A, 20, 61

Dyson, F. J. 1967, Physical Review Letters, 19, 1291

Dyson, F. J. 1972, in Aspects of Quantum Theory (Salem, A. and Wigner, E. P.)

Dzuba, V. A., Derevianko, A., & Flambaum, V. V. 2012, Phys. Rev. A, 86, 054502

Dzuba, V. A. & Flambaum, V. V. 2008, Phys. Rev. A, 77, 012514

Dzuba, V. A., Flambaum, V. V., Kozlov, M. G., & Marchenko, M. 2002, Phys. Rev. A, 66, 022501

Dzuba, V. A., Flambaum, V. V., & Marchenko, M. V. 2003, Phys. Rev. A, 68, 022506

Dzuba, V. A., Flambaum, V. V., & Webb, J. K. 1999, Phys. Rev. A, 59, 230

Ekström, S., Coc, A., Descouvemont, P., et al. 2010, A&A, 514, A62

Fischer, M., Kolachevsky, N., Zimmermann, M., et al. 2004, Physical Review Letters, 92, 230802

Fujii, Y., Iwamoto, A., Fukahori, T., et al. 2000, Nuclear Physics B, 573, 377

Gold, R. 1968, Phys. Rev. Lett., 20, 219

Gould, C. R., Sharapov, E. I., & Lamoreaux, S. K. 2006, Phys. Rev. C, 74, 024607

Green, M. B. & Schwarz, J. H. 1981, Nuclear Physics B, 181, 502

Griest, K., Whitmore, J. B., Wolfe, A. M., et al. 2010, ApJ, 708, 158

Hansen, N. & Ostermeier, A. 2001, Evolutionary Computation, 9, 159

Ichikawa, K., Kanzaki, T., & Kawasaki, M. 2006, Phys. Rev. D, 74, 023515

Ichikawa, K. & Kawasaki, M. 2002, Phys. Rev. D, 65, 123511

Ivanchik, A. V., Potekhin, A. Y., & Varshalovich, D. A. 1999, A&A, 343, 439

Kaluza, T. 1921, Sitzungsberichte der Königlich Preußischen Akademie der Wissenschaften (Berlin), Seite p. 966-972, 966

Kaplinghat, M., Scherrer, R. J., & Turner, M. S. 1999, Phys. Rev. D, 60, 023516

Klein, O. 1926, Zeitschrift fur Physik, 37, 895

Kolb, E. W., Perry, M. J., & Walker, T. P. 1986, Phys. Rev. D, 33, 869

Kothari, D. S. 1938, Nature, 142, 354

Landau, S. J., Harari, D. D., & Zaldarriaga, M. 2001, Phys. Rev. D, 63, 083505

Landau, S. J. & Scóccola, G. 2010, A&A, 517, A62+

Lange, A., de Bernardis, P., de Petris, M., et al. 1995, Space Sci. Rev., 74, 145

Lee, A. T., Ade, P., Balbi, A., et al. 1999, in American Institute of Physics Conference Series, Vol. 476, 3K cosmology, ed. L. Maiani, F. Melchiorri, & N. Vittorio, 224–236

Leefer, N., Weber, C. T. M., Cingöz, A., Torgerson, J. R., & Budker, D. 2013, Physical Review Letters, 111, 060801

Levshakov, S. A. 1992, in European Southern Observatory Conference and Workshop Proceedings, Vol. 40, European Southern Observatory Conference and Workshop Proceedings, ed. M.-H. Ulrich, 139–+

Levshakov, S. A. 1994, MNRAS, 269, 339

Levshakov, S. A. 2004, in Lecture Notes in Physics, Berlin Springer Verlag, Vol. 648, Astrophysics, Clocks and Fundamental Constants, ed. S. G. Karshenboim & E. Peik, 151–166

Levshakov, S. A., Centurión, M., Molaro, P., & D'Odorico, S. 2005, A&A, 434, 827

Levshakov, S. A., Molaro, P., Lopez, S., et al. 2007, A&A, 466, 1077

Lindner, M., Leich, D. A., Borg, R. J., et al. 1986, Nature, 320, 246

Marciano, W. J. 1984, Physical Review Letters, 52, 489

Marion, H., Pereira Dos Santos, F., Abgrall, M., et al. 2003, Physical Review Letters, 90, 150801

Martins, C. J. A. P., Melchiorri, A., Rocha, G., et al. 2004, Physics Letters B, 585, 29

Mather, J. C. 1993, in Society of Photo-Optical Instrumentation Engineers (SPIE) Conference Series, Vol. 2019, Infrared Spaceborne Remote Sensing, ed. M. S. Scholl, 146–157

McPherson, A., Gilmozzi, R., Spyromilio, J., Kissler-Patig, M., & Ramsay, S. 2012, The Messenger, 148, 2

Mégevand, D., Zerbi, F. M., Cabral, A., et al. 2012, in Society of Photo-Optical Instrumentation Engineers (SPIE) Conference Series, Vol. 8446, Society of Photo-Optical Instrumentation Engineers (SPIE) Conference Series

Molaro, P., Centurion, M., Whitmore, J. B., et al. 2013, ArXiv e-prints

Molaro, P., Levshakov, S. A., Monai, S., et al. 2008a, A&A, 481, 559

Molaro, P., Reimers, D., Agafonova, I. I., & Levshakov, S. A. 2008b, European Physical Journal Special Topics, 163, 173

Morton, D. C. 2003, ApJS, 149, 205

Murphy, M. T., Webb, J. K., & Flambaum, V. V. 2003, MNRAS, 345, 609

Murphy, M. T., Webb, J. K., & Flambaum, V. V. 2008, MNRAS, 384, 1053

Murphy, M. T., Webb, J. K., Flambaum, V. V., et al. 2001a, MNRAS, 327, 1244

Murphy, M. T., Webb, J. K., Flambaum, V. V., et al. 2001b, MNRAS, 327, 1208

Murphy, M. T., Webb, J. K., Flambaum, V. V., Prochaska, J. X., & Wolfe, A. M. 2001c, MNRAS, 327, 1237

Nambu, Y. 1970, in Symmetries and Quark Models, ed. R. Chand, 269

Nave, G. & Sansonetti, C. J. 2011, Journal of the Optical Society of America B Optical Physics, 28, 737

Nguyen, A. T., Budker, D., Lamoreaux, S. K., & Torgerson, J. R. 2004, Phys. Rev. A, 69, 022105

Nollett, K. M. & Lopez, R. E. 2002, Phys. Rev. D, 66, 063507

O'Bryan, J., Smidt, J., De Bernardis, F., & Cooray, A. 2013, ArXiv e-prints

Olive, K. A., Pospelov, M., Qian, Y.-Z., et al. 2002, Phys. Rev. D, 66, 045022

Olive, K. A., Pospelov, M., Qian, Y.-Z., et al. 2004, Phys. Rev. D, 69, 027701

Pasquini, L., Cristiani, S., García López, R., et al. 2010, in Society of Photo-Optical Instrumentation Engineers (SPIE) Conference Series, Vol. 7735, Society of Photo-Optical Instrumentation Engineers (SPIE) Conference Series

Peik, E., Lipphardt, B., Schnatz, H., et al. 2004, Physical Review Letters, 93, 170801

Peik, E., Lipphardt, B., Schnatz, H., et al. 2006, ArXiv Physics e-prints

Pepe, F., Mayor, M., Rupprecht, G., et al. 2002, The Messenger, 110, 9

Petrov, Y. V., Nazarov, A. I., Onegin, M. S., Petrov, V. Y., & Sakhnovsky, E. G. 2006, Phys. Rev. C, 74, 064610

Porsev, S. G., Koshelev, K. V., Tupitsyn, I. I., et al. 2007, Phys. Rev. A, 76, 052507

Potekhin, A. Y. & Varshalovich, D. A. 1994, A&AS, 104, 89

Prause, N. & Reimers, D. 2013, A&A, 555, A88

Quast, R., Baade, R., & Reimers, D. 2005, A&A, 431, 1167

Quast, R., Reimers, D., & Levshakov, S. A. 2004, A&A, 415, L7

Reeves, H. 1994, Reviews of Modern Physics, 66, 193

Rosenband, T., Hume, D. B., Schmidt, P. O., et al. 2008, Science, 319, 1808

Savedoff, M. P. 1956, Nature, 178, 688

Savukov, I. M. & Dzuba, V. A. 2008, Phys. Rev. A, 77, 042501

Scherk, J. & Schwarz, J. H. 1974, Nuclear Physics B, 81, 118

Scóccola, C. G., Landau, S. J., & Vucetich, H. 2008, Physics Letters B, 669, 212

Shlyakhter, A. I. 1976, Nature, 264, 340

Sortais, Y., Bize, S., & Abgrall, M. 2001, Physica Scripta Volume T, 95, 50

Srianand, R., Gupta, N., Petitjean, P., Noterdaeme, P., & Ledoux, C. 2010, MNRAS, 405, 1888

Tauber, J. A., Mandolesi, N., Puget, J.-L., et al. 2010, A&A, 520, A1

Turneaure, J. P. & Stein, S. R. 1976, in Atomic Masses and Fundamental Constants, ed. J. H. Sanders & A. H. Wapstra, Vol. 5

Tzanavaris, P., Murphy, M. T., Webb, J. K., Flambaum, V. V., & Curran, S. J. 2007, MNRAS, 374, 634

Varshalovich, D. A., Panchuk, V. E., & Ivanchik, A. V. 1996, Astronomy Letters, 22, 6

Veneziano, G. 1968, Nuovo Cimento A Serie, 57, 190

Vogt, S. S., Allen, S. L., Bigelow, B. C., et al. 1994, in Society of Photo-Optical Instrumentation Engineers (SPIE) Conference Series, Vol. 2198, Instrumentation in Astronomy VIII, ed. D. L. Crawford & E. R. Craine, 362

Webb, J. K., Flambaum, V. V., Churchill, C. W., Drinkwater, M. J., & Barrow, J. D. 1999, Physical Review Letters, 82, 884

Webb, J. K., King, J. A., Murphy, M. T., et al. 2010, ArXiv e-prints

Webb, J. K., Murphy, M. T., Flambaum, V. V., et al. 2001, Physical Review Letters, 87, 091301

Weinberg, S. 1983, Physics Letters B, 125, 265

Welty, D. 1998, in Lecture Notes in Physics, Berlin Springer Verlag, Vol. 506, IAU Colloq. 166: The Local Bubble and Beyond, ed. D. Breitschwerdt, M. J. Freyberg, & J. Truemper, 151–160

Welty, D. E., Hobbs, L. M., & Kulkarni, V. P. 1994, ApJ, 436, 152

Welty, D. E., Morton, D. C., & Hobbs, L. M. 1996, ApJS, 106, 533

Wendt, M. & Molaro, P. 2011, A&A, 526, A96+

Wilkinson, D. H. 1958, Philosophical Magazine, 3, 582

Wolfe, A. M. 1980, Phys. Scr, 21, 744

Wolfe, A. M., Brown, R. L., & Roberts, M. S. 1976, Physical Review Letters, 37, 179

Appendix A

Simulations

A.1 Symmetric line

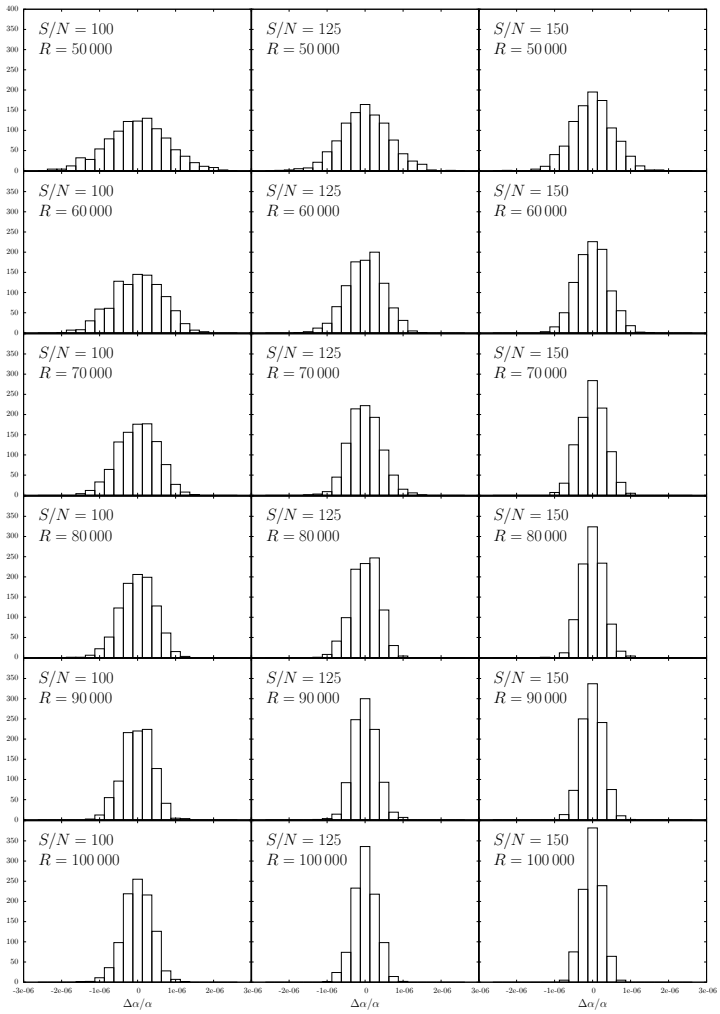

Figure A.1: Histograms of measured α variation for a single symmetric line profile.

A.2 Line blend histograms

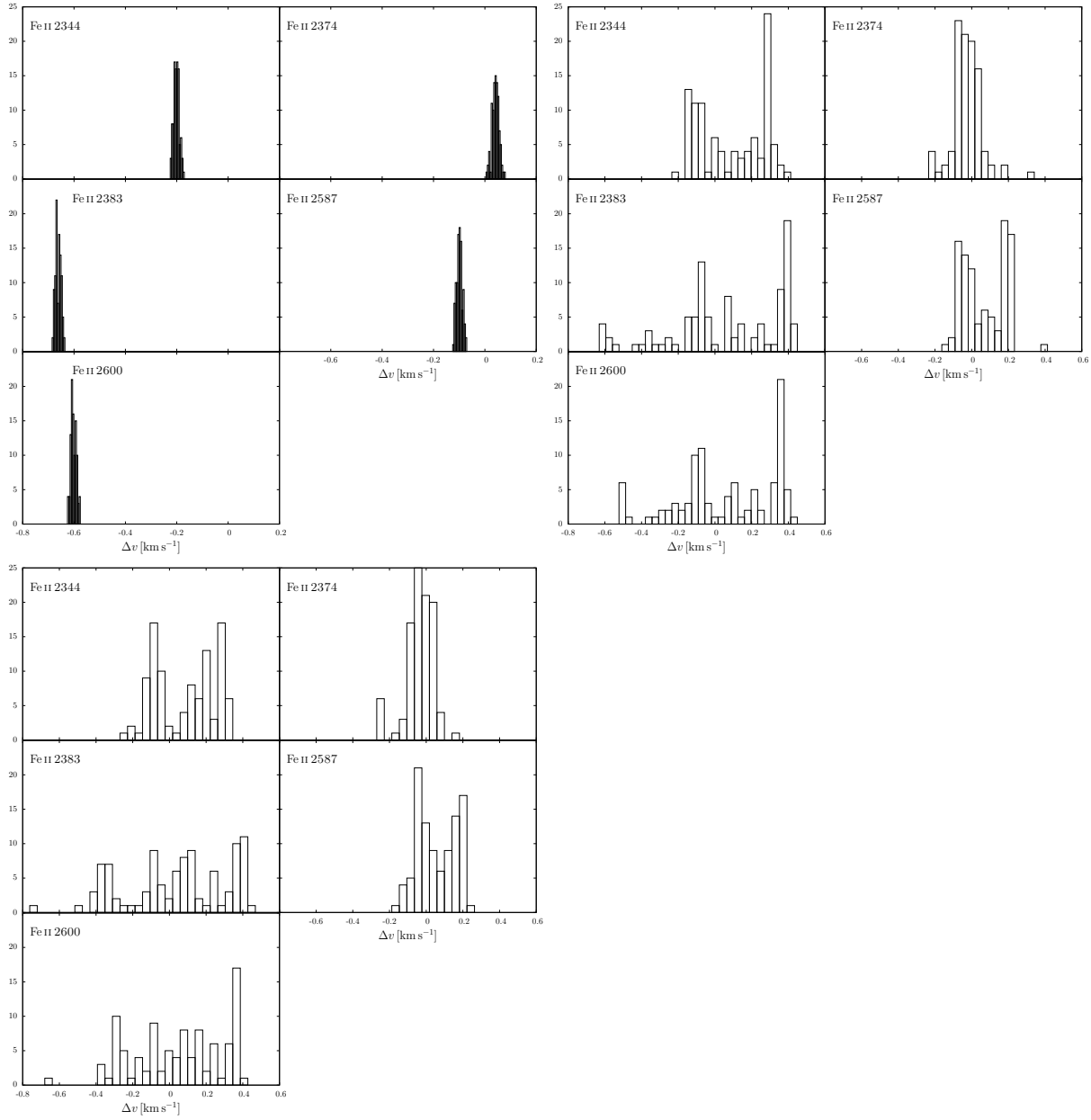

Figure A.2: Histograms of the apparent velocity shifts relative to Fe II 1608 of close line blends simulated as in Fig. 3.8. One-component fit, four-component fit, and five-component fit for 100 realisations with random noise.

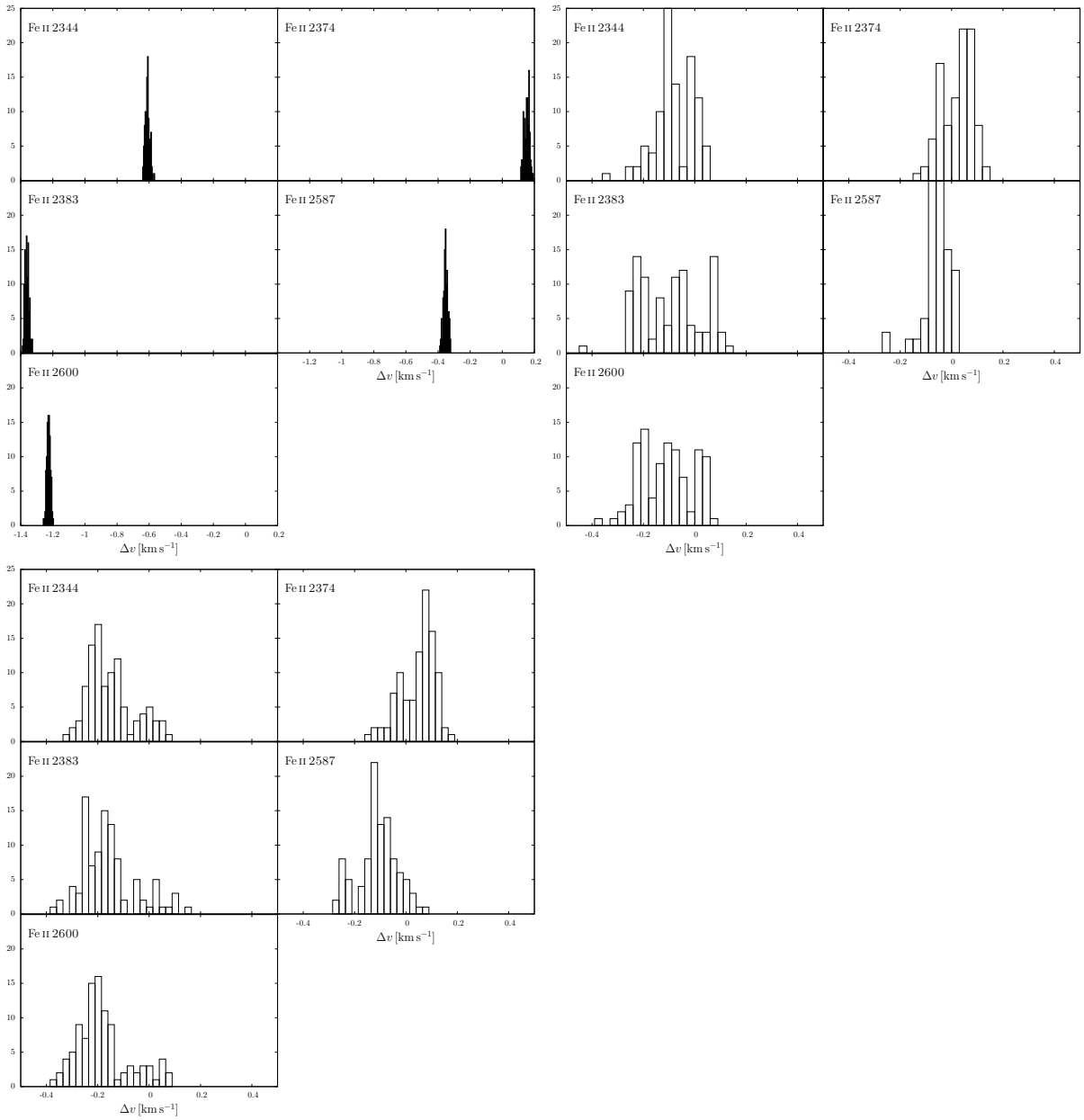

Figure A.3: Histograms of the apparent velocity shifts relative to Fe II 1608 of close line blends simulated as in Fig. 3.9. One-component fit, four-component fit, and five-component fit for 100 realisations with random noise.

A.3 Velocity field spectra

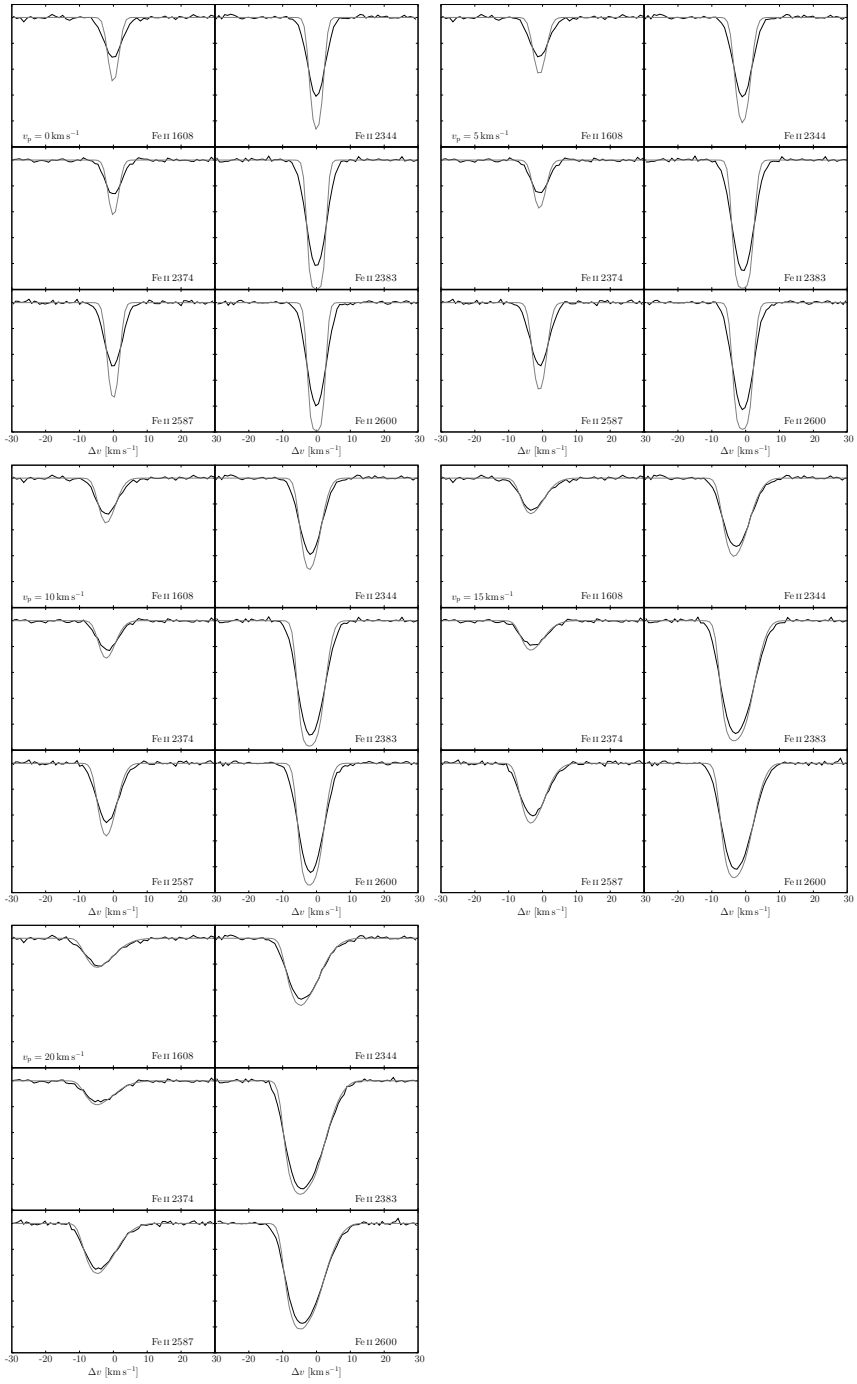

Figure A.4: Spectra of simulated lines with an underlying velocity field with peak velocity $v_\mathrm{p} = 0\mathrm{km\,s^{-1}}$ to $v_\mathrm{p} = 20\,\mathrm{km\,s^{-1}}$.

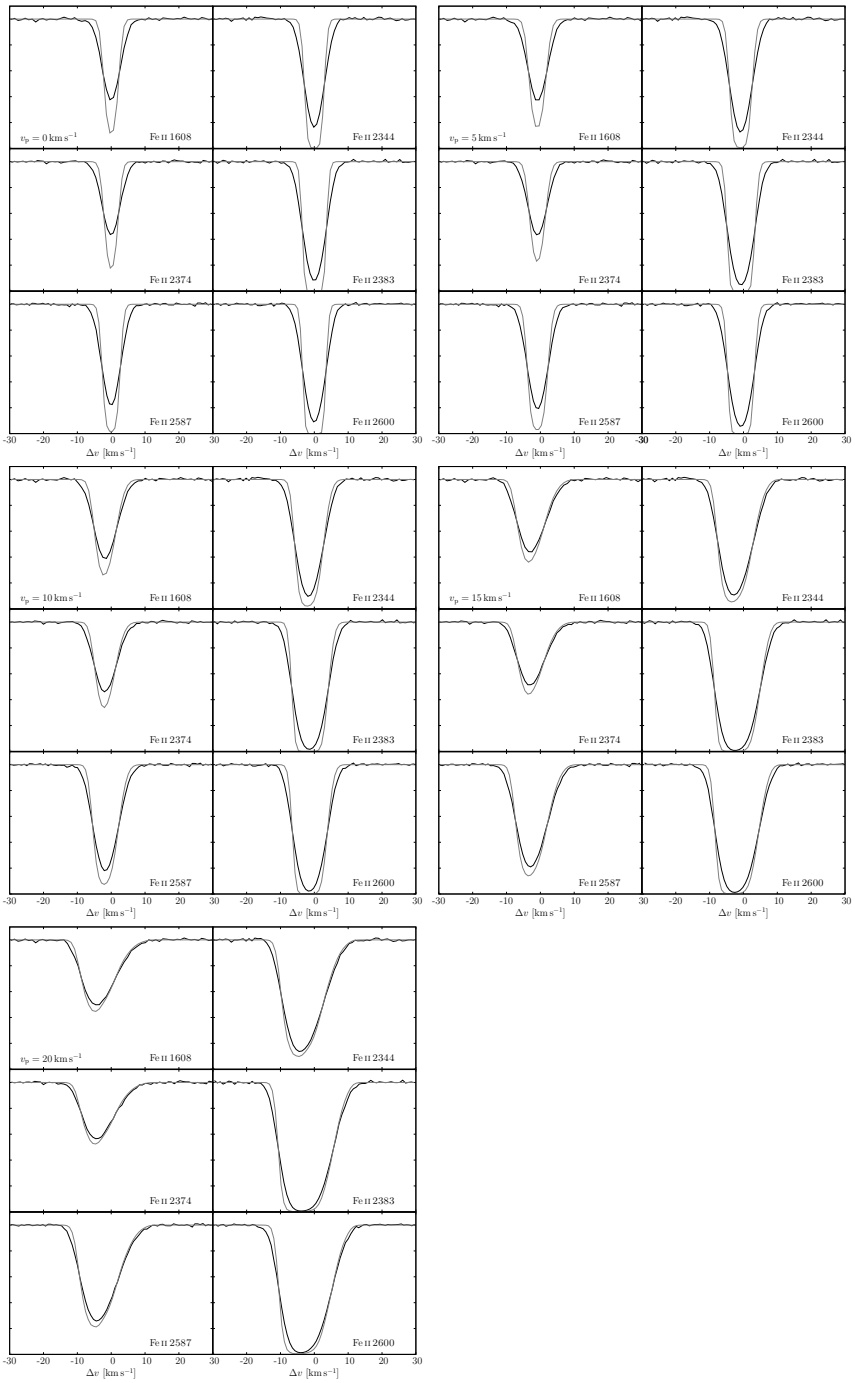

Figure A.5: Spectra of simulated lines with an underlying velocity field with peak velocity $v_\mathrm{p} = 0\mathrm{km\,s^{-1}}$ to $v_\mathrm{p} = 20\mathrm{km\,s^{-1}}$. Saturated version.

A.4 Velocity field histograms

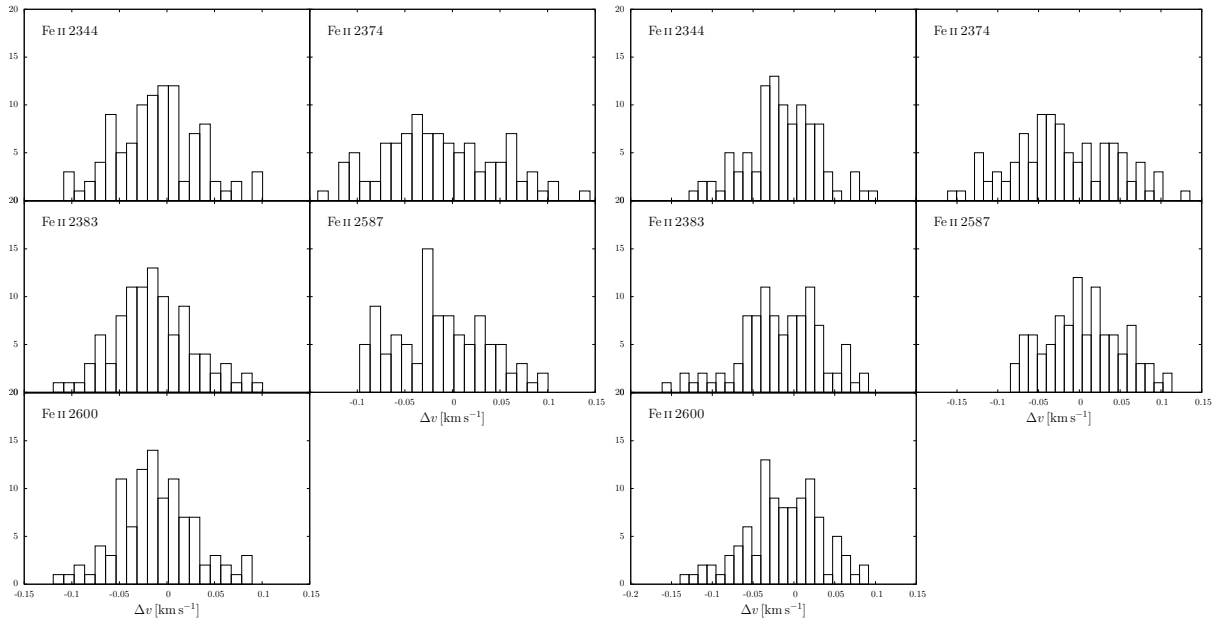

Figure A.6: Histograms of apparent velocity shifts relative to Fe II 1608 of simulated lines with an underlying velocity field with peak velocity $v_\mathrm{p} = 0\mathrm{km\,s^{-1}}$. One-component and two-component fits of 100 realisations with random noise each.

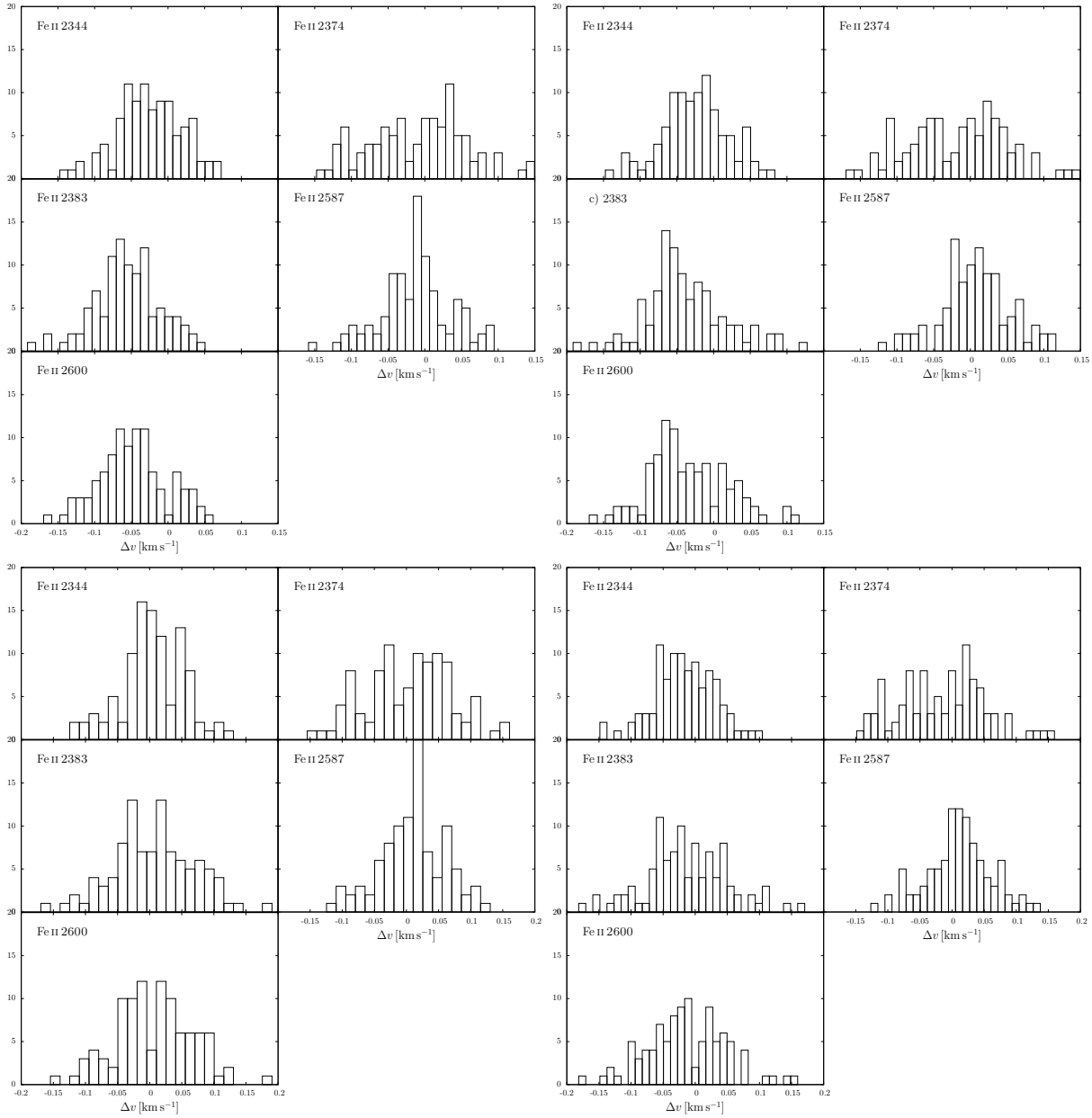

Figure A.7: Histograms of apparent velocity shifts relative to Fe II 1608 of simulated lines with an underlying velocity field with peak velocity $v_\mathrm{p} = 5\mathrm{km\,s^{-1}}$. One-component to four-component fits of 100 realisations with random noise each.

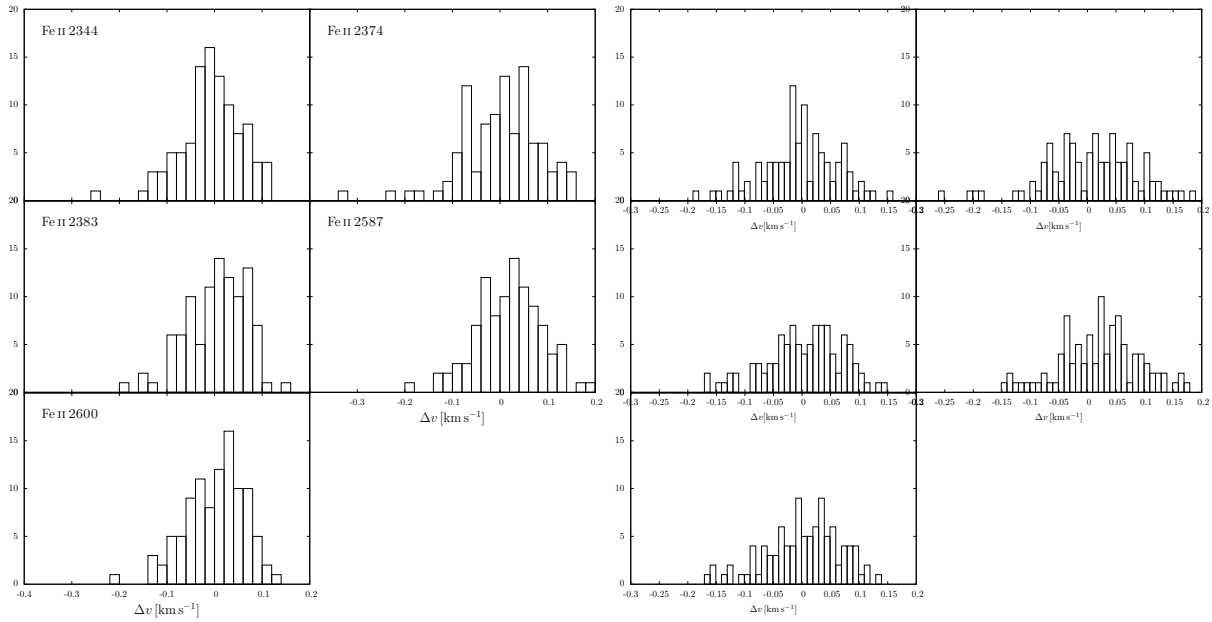

Figure A.8: Histograms of apparent velocity shifts relative to Fe II 1608 of simulated lines with an underlying velocity field with peak velocity $v_\mathrm{p} = 10\mathrm{km\,s^{-1}}$. Three-component and four-component fits of 100 realisations with random noise each.

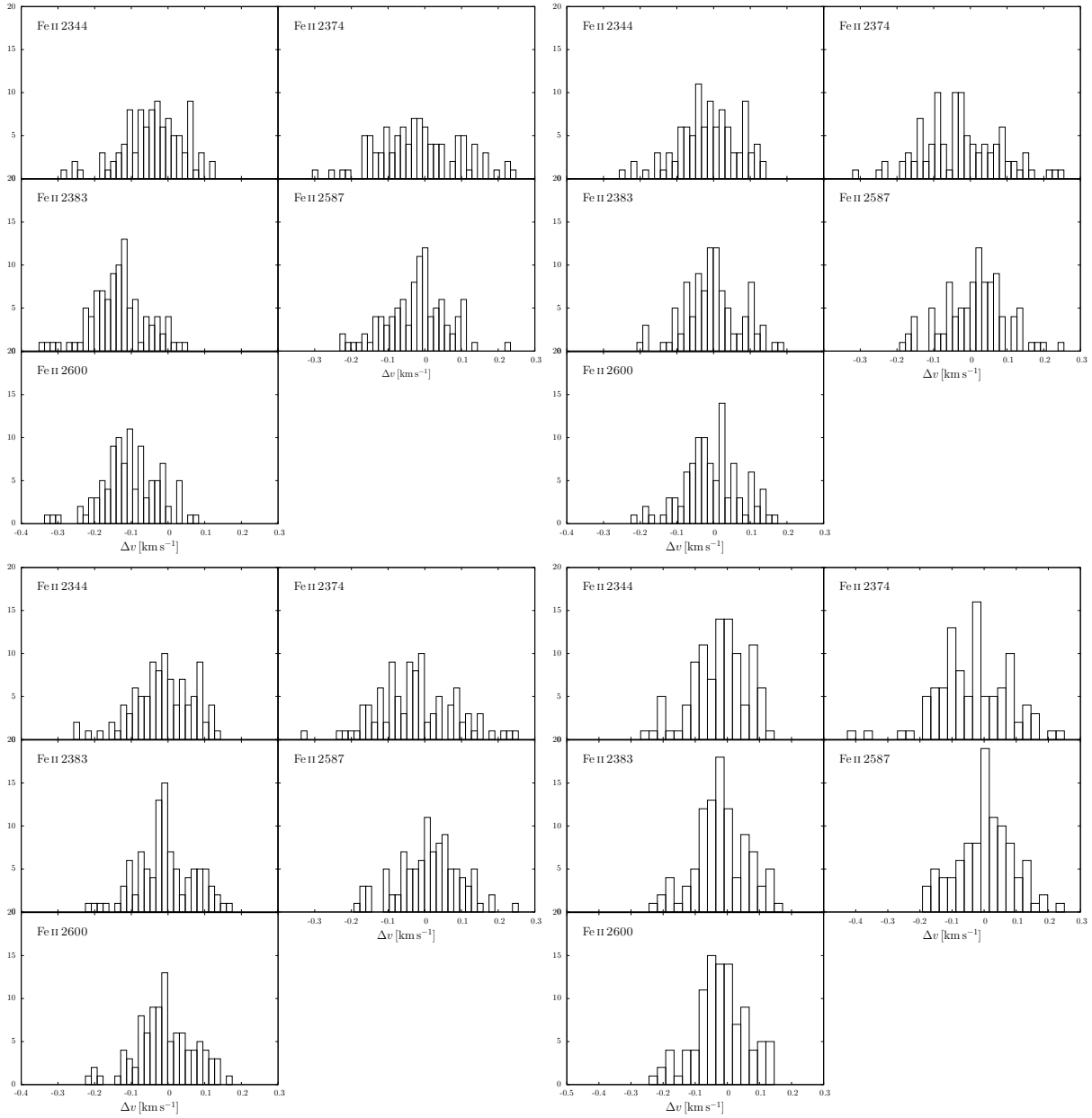

Figure A.9: Histograms of apparent velocity shifts relative to Fe II 1608 of simulated lines with an underlying velocity field with peak velocity $v_\mathrm{p} = 15\mathrm{km\,s^{-1}}$. One-component to four-component fits of 100 realisations with random noise each.

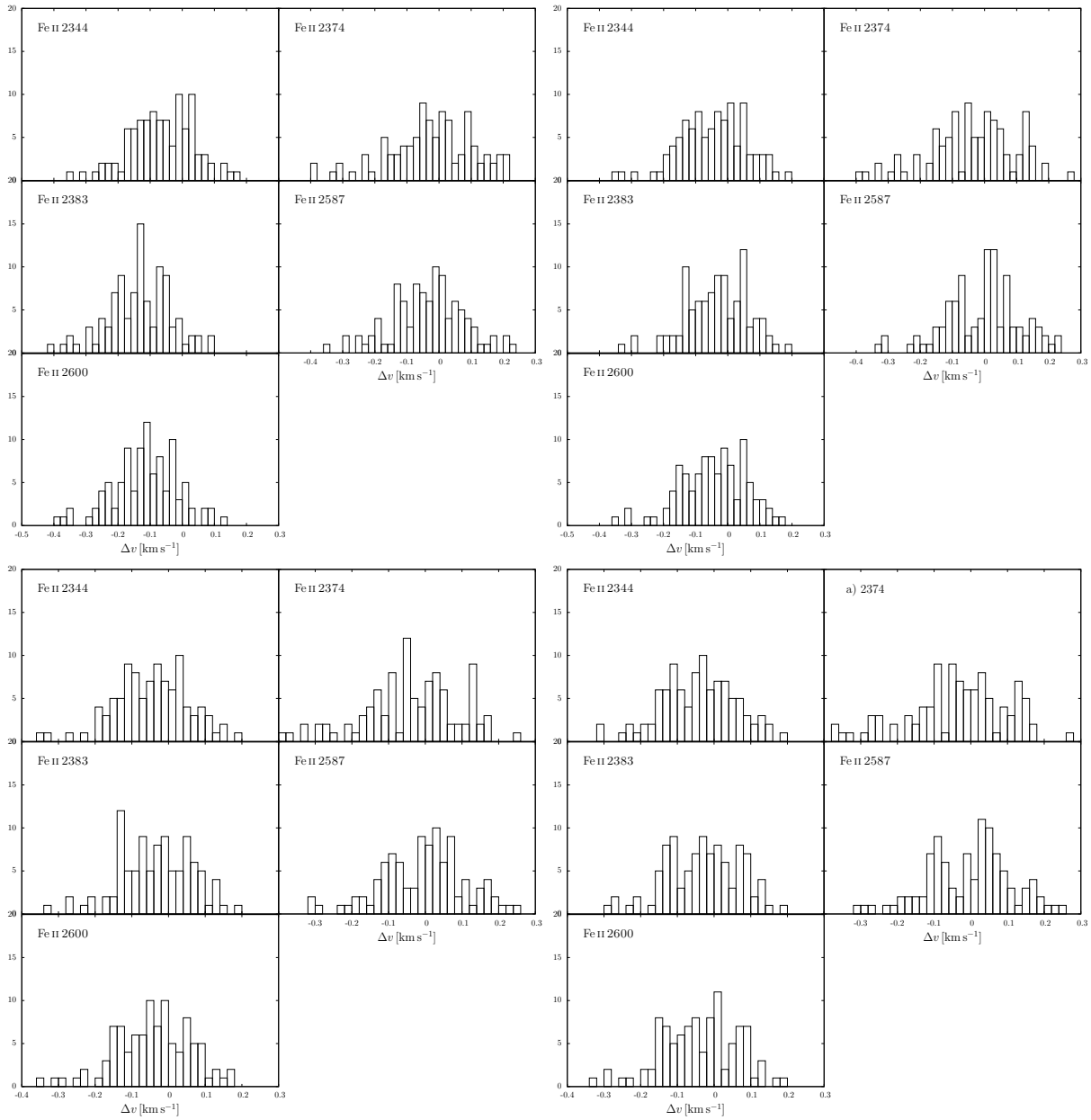

Figure A.10: Histograms of apparent velocity shifts relative to Fe II 1608 of simulated lines with an underlying velocity field with peak velocity $v_{\rm p} = 20 {\rm km\,s^{-1}}$. One-component to four-component fits of 100 realisations with random noise each.

A.5 Bisectors

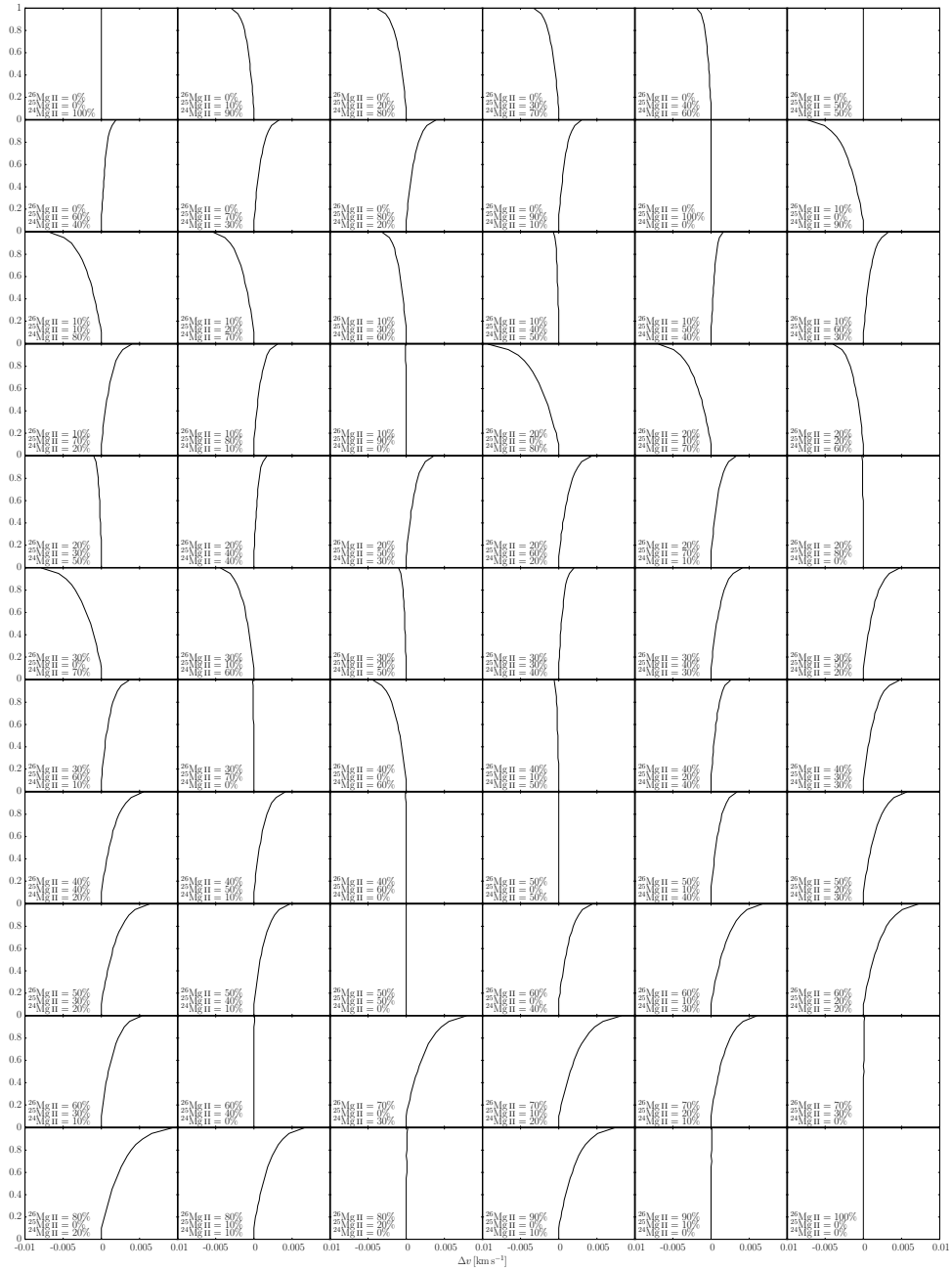

Figure A.11: Grid of bisectors of simulated Mg II 2796 lines with changing isotope abundances with $R = 45\,000$. The combined column density is $N = 12.5$. The Doppler parameter for each isotope is $b = 2\,\mathrm{km\,s^{-1}}$.

Appendix B

Data

B.1 HE0515

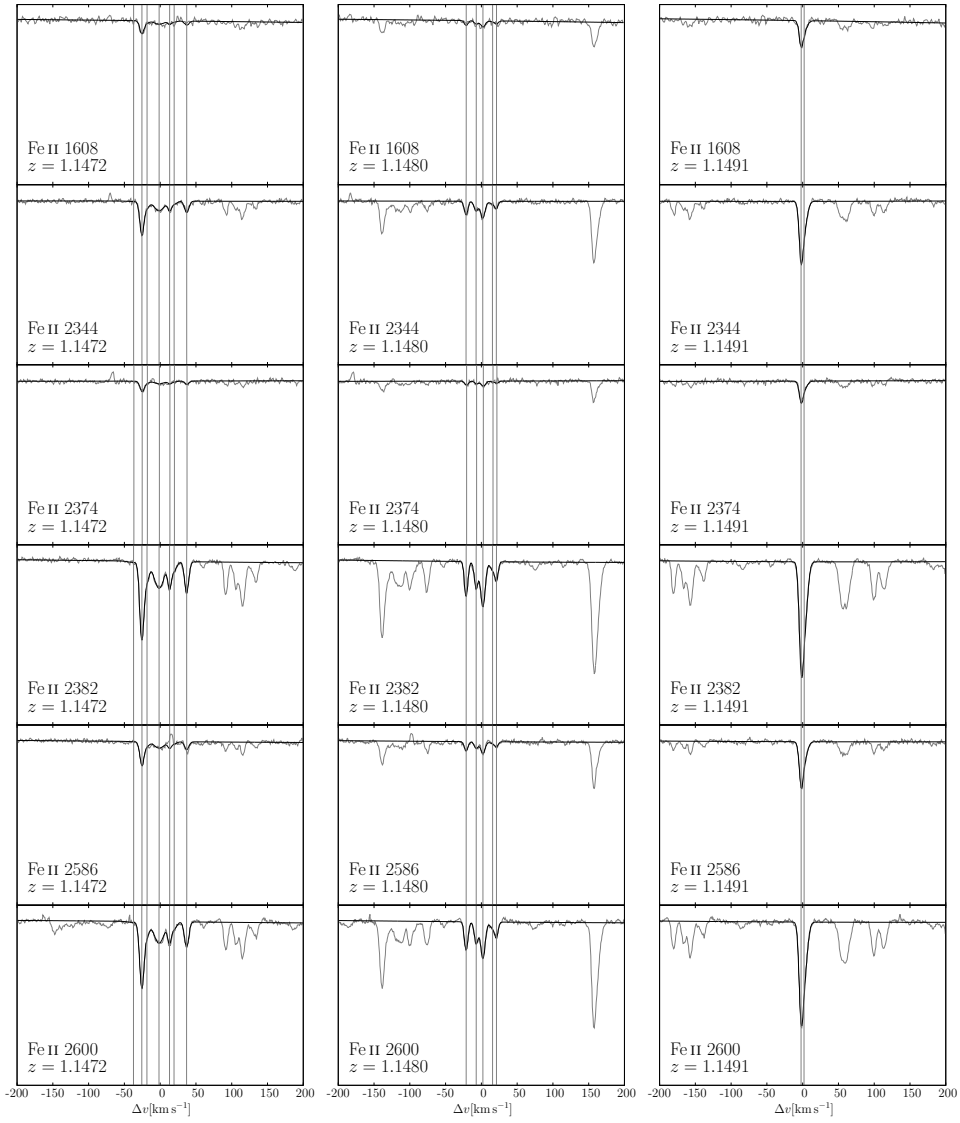

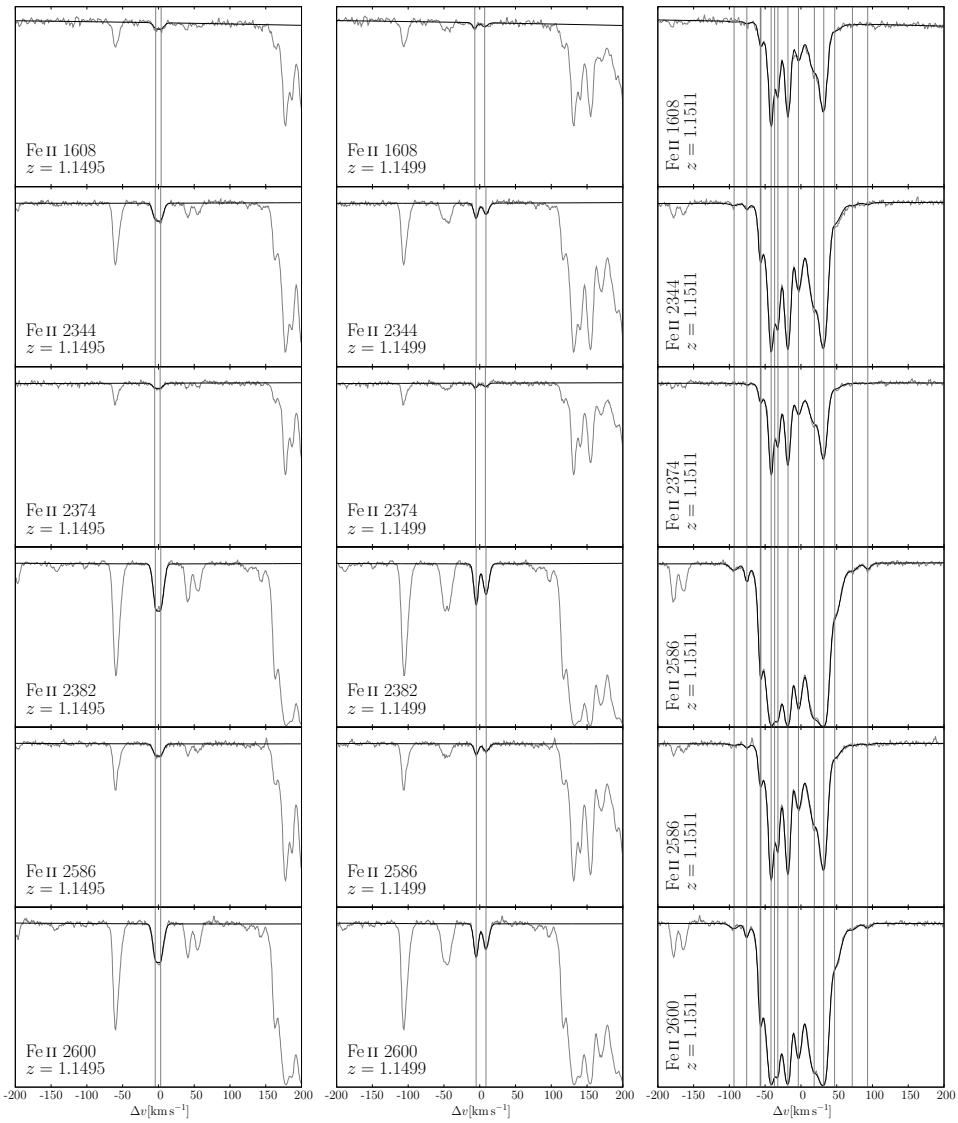

Figure B.1: Spectra and best fit of the Fe II system at $z = 1.15$ in HE0515. Best fit positions are indicated by vertical lines.

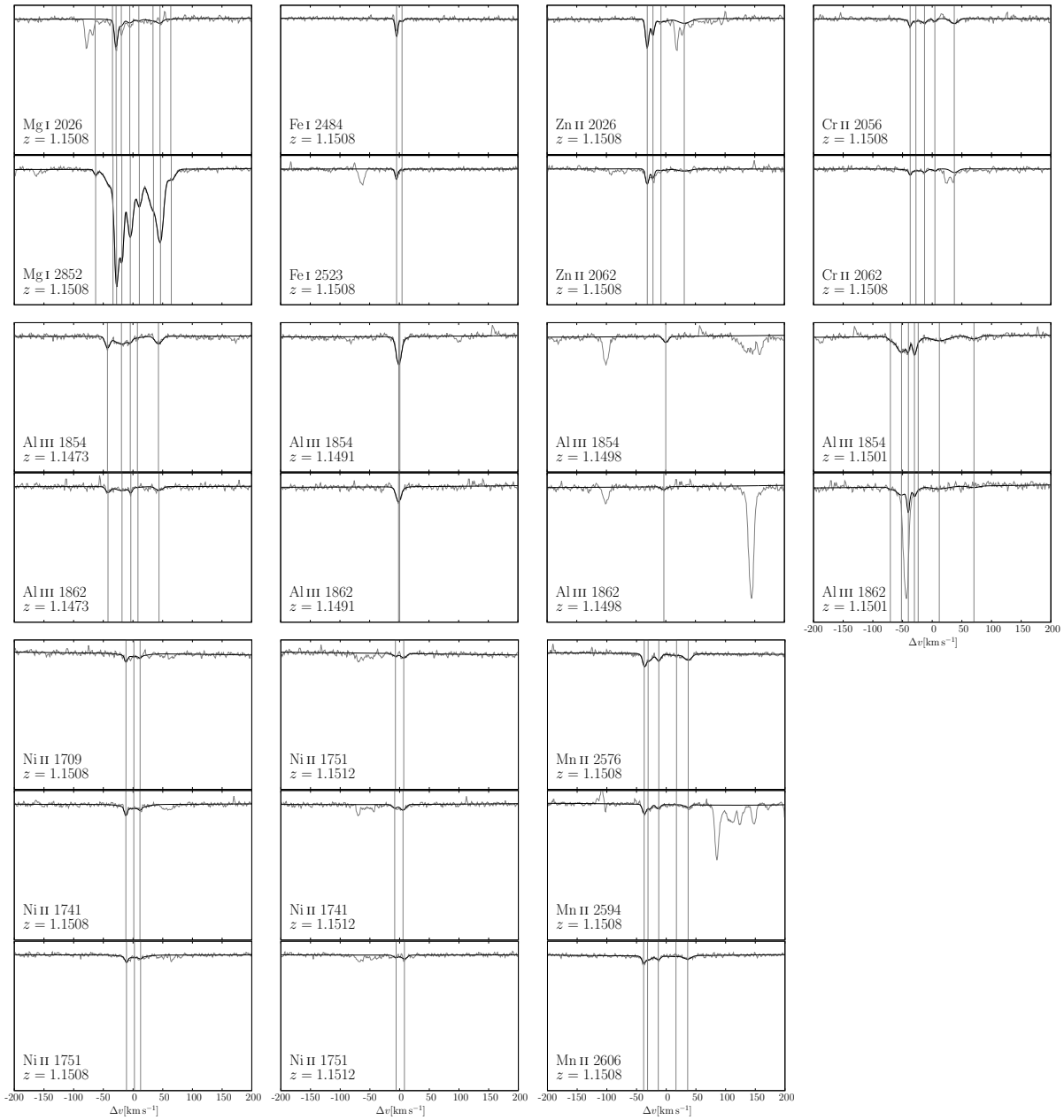

Figure B.2: Spectra and best fit of the metal lines of $z = 1.15$ system in HE0515. Best fit positions are indicated by vertical lines.

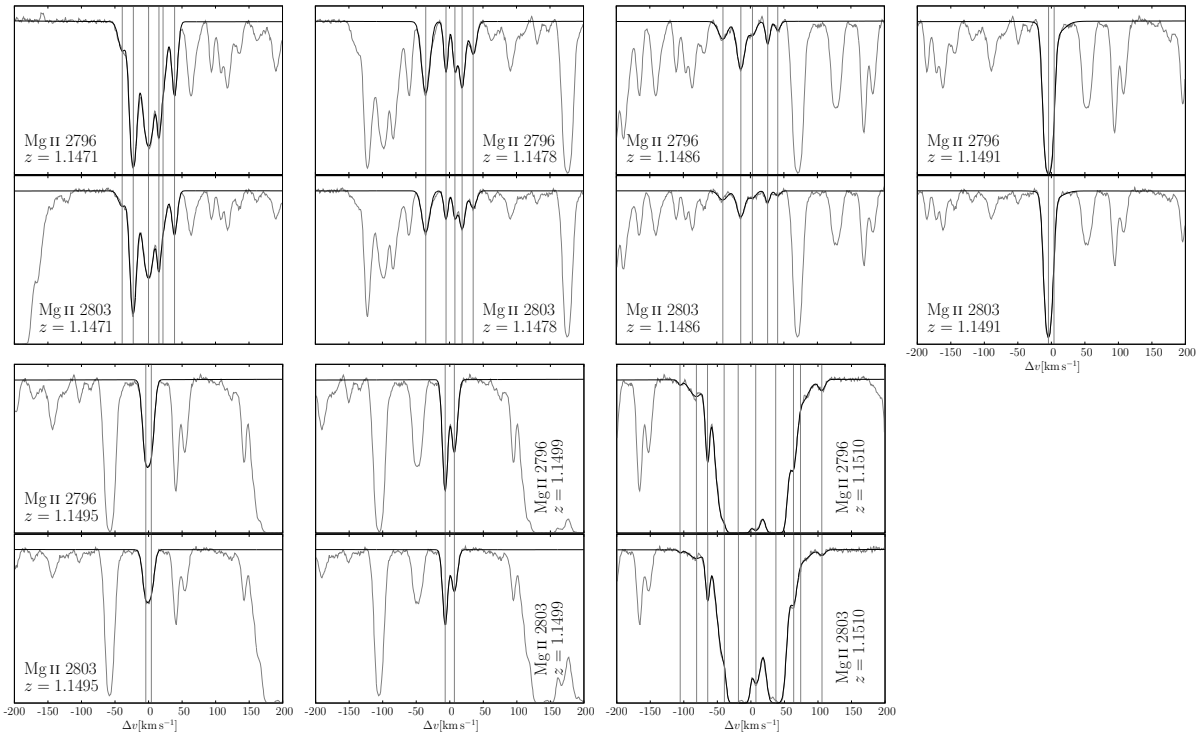

Figure B.3: Spectra and best fit of the Mg II system at $z = 1.15$ in HE0515. Best fit positions are indicated by vertical lines.

B.2 2004 Large Program

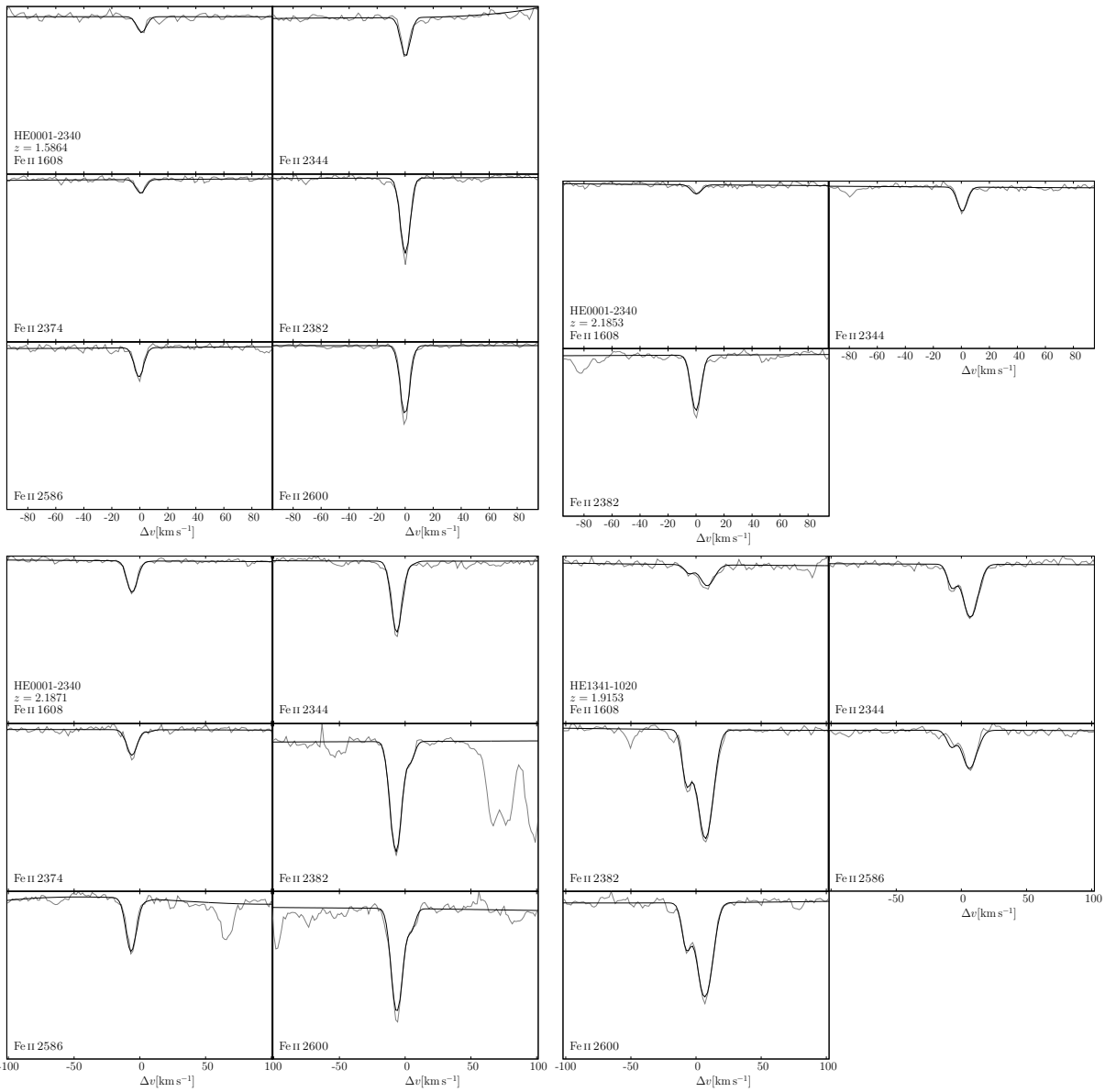

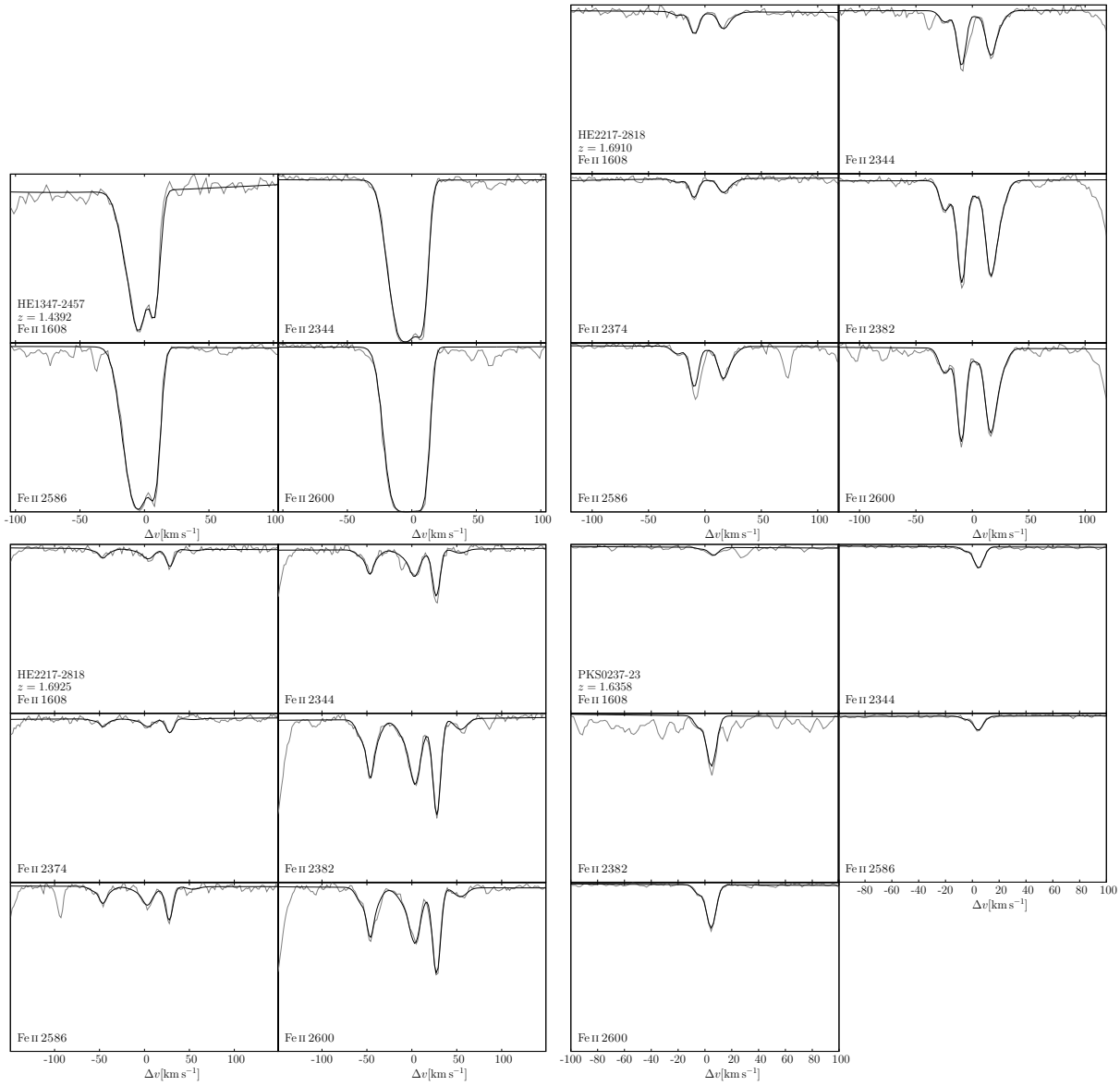
HE1347-2457
$z = 1.4392$
Fe II 1608
Fe II 2344
Fe II 2586
Fe II 2600
HE2217-2818
$z = 1.6910$
Fe II 1608
Fe II 2344
Fe II 2374
Fe II 2382
Fe II 2586
Fe II 2600
HE2217-2818
$z = 1.6925$
Fe II 1608
Fe II 2344
Fe II 2374
Fe II 2382
Fe II 2586
Fe II 2600
PKS0237-23
$z = 1.6358$
Fe II 1608
Fe II 2344
Fe II 2382
Fe II 2586
Fe II 2600
Δv[km s^{-1}]

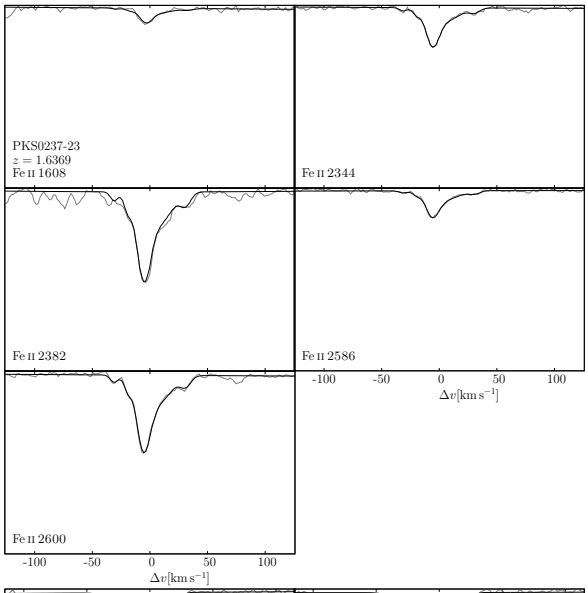
PKS0237-23
$z = 1.6369$
Fe II 1608
Fe II 2344
Fe II 2382
Fe II 2586
Fe II 2600
-100 -50 0 50 100
Δv[km s^{-1}]

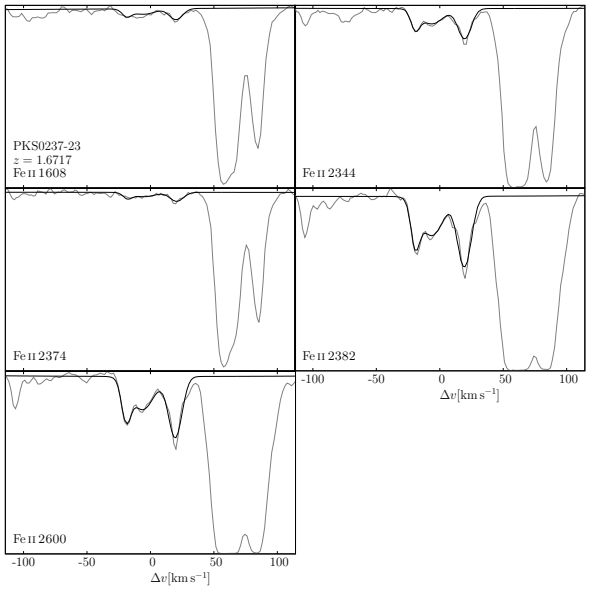
PKS0237-23
$z = 1.6717$
Fe II 1608
Fe II 2344
Fe II 2374
Fe II 2382
Fe II 2600
-100 -50 0 50 100
Δv[km s^{-1}]

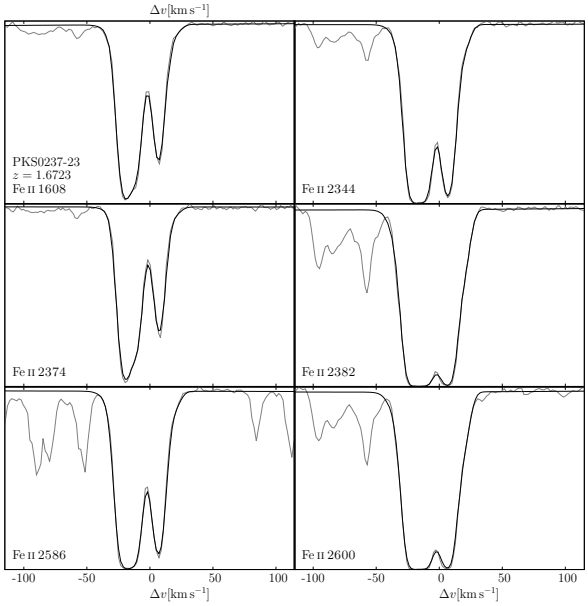
PKS0237-23
$z = 1.6723$
Fe II 1608
Fe II 2344
Fe II 2374
Fe II 2382
Fe II 2586
Fe II 2600
-100 -50 0 50 100
Δv[km s^{-1}]

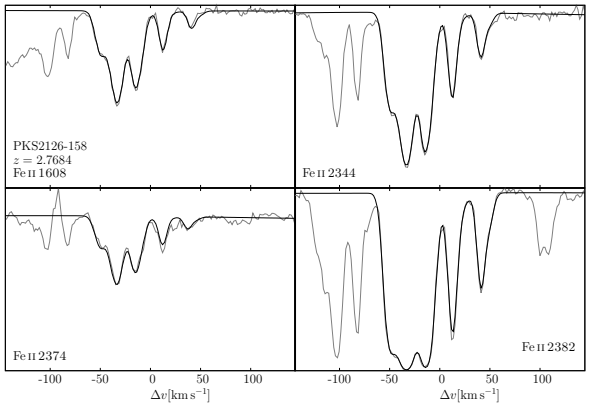
PKS2126-158
$z = 2.7684$
Fe II 1608
Fe II 2344
Fe II 2374
Fe II 2382
-100 -50 0 50 100
Δv[km s^{-1}]

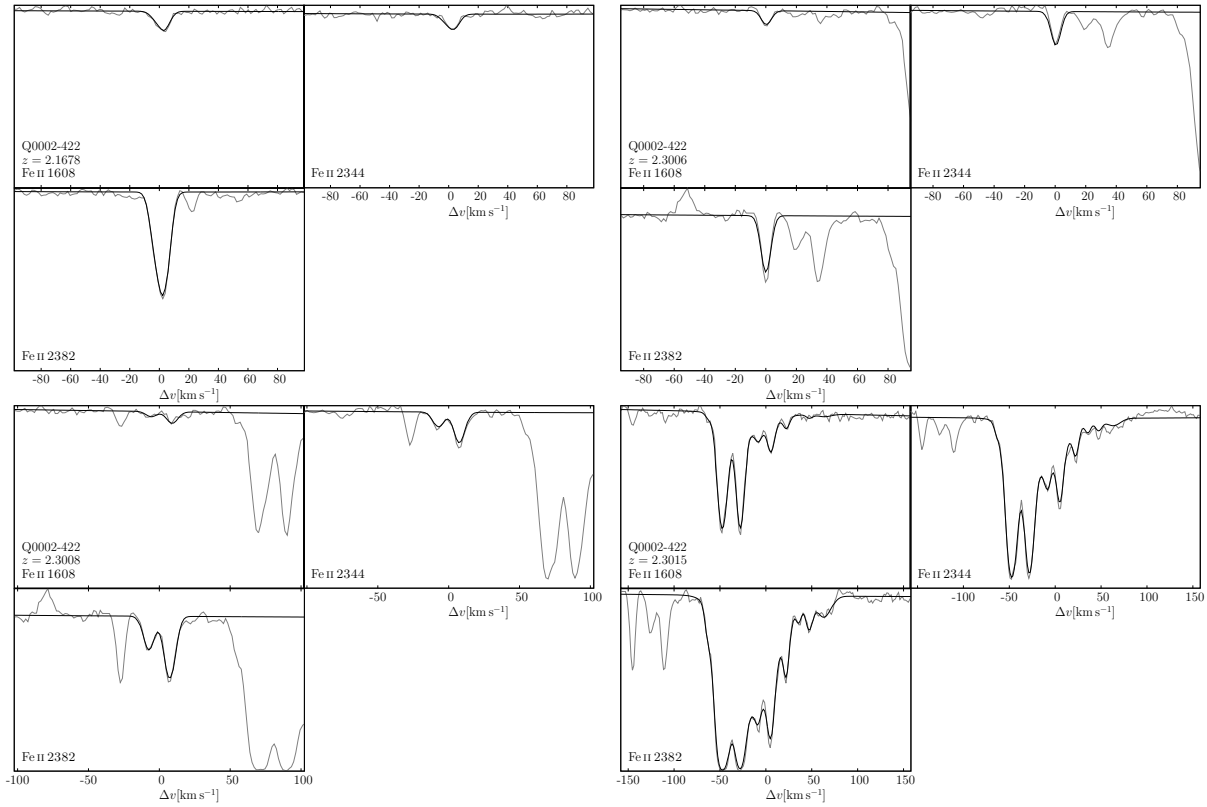

Figure B.4: Spectra and best fit of the 2004 Large Program data sample.

B.3 MgII

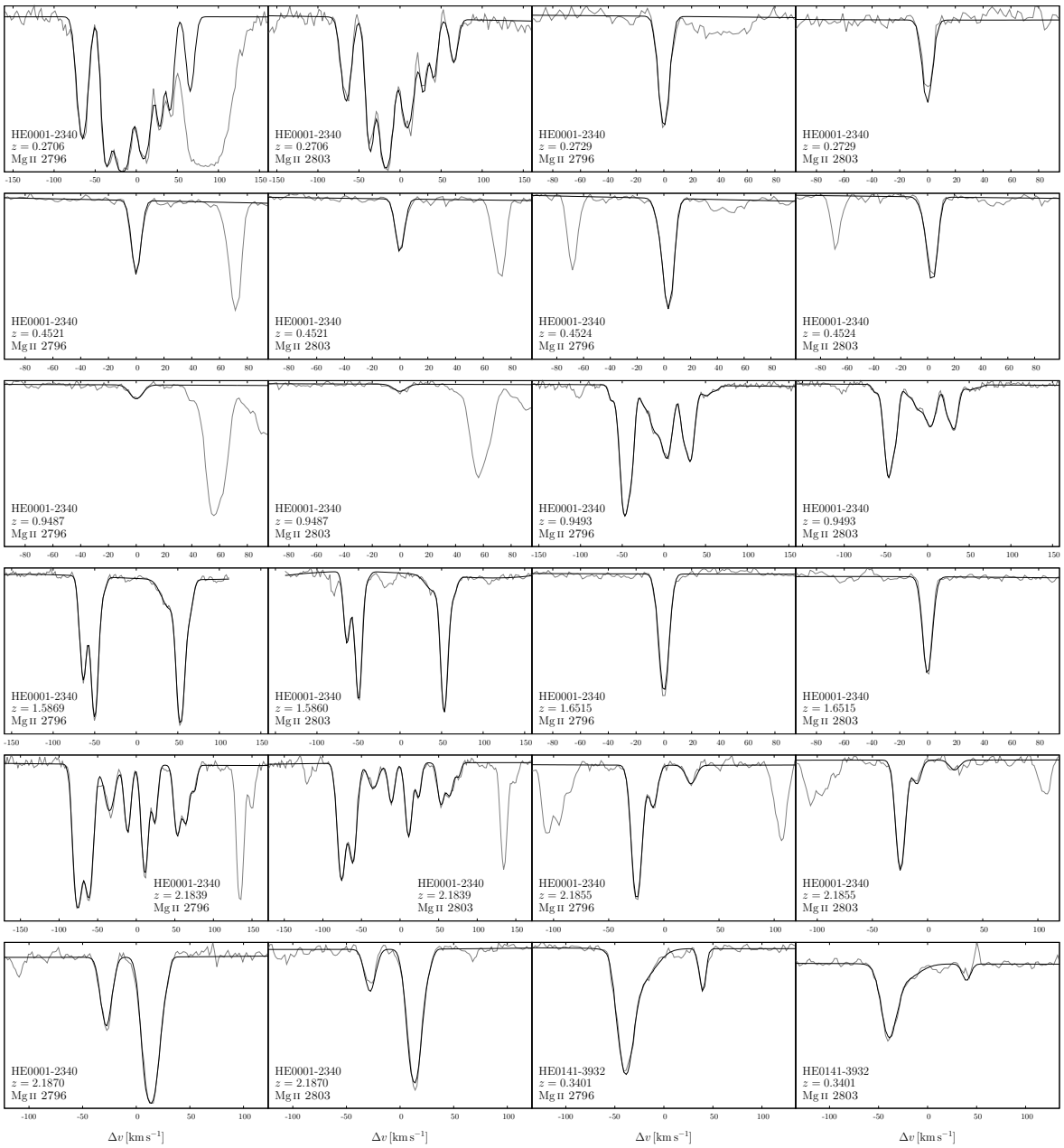
HE0001-2340
z = 0.2706
Mg II 2796
HE0001-2340
z = 0.2706
Mg II 2803
HE0001-2340
z = 0.2729
Mg II 2796
HE0001-2340
z = 0.2729
Mg II 2803
HE0001-2340
z = 0.4521
Mg II 2796
HE0001-2340
z = 0.4521
Mg II 2803
HE0001-2340
z = 0.4524
Mg II 2796
HE0001-2340
z = 0.4524
Mg II 2803
HE0001-2340
z = 0.9487
Mg II 2796
HE0001-2340
z = 0.9487
Mg II 2803
HE0001-2340
z = 0.9493
Mg II 2796
HE0001-2340
z = 0.9493
Mg II 2803
HE0001-2340
z = 1.5869
Mg II 2796
HE0001-2340
z = 1.5860
Mg II 2803
HE0001-2340
z = 1.6515
Mg II 2796
HE0001-2340
z = 1.6515
Mg II 2803
HE0001-2340
z = 2.1839
Mg II 2796
HE0001-2340
z = 2.1839
Mg II 2803
HE0001-2340
z = 2.1855
Mg II 2796
HE0001-2340
z = 2.1855
Mg II 2803
HE0001-2340
z = 2.1870
Mg II 2796
HE0001-2340
z = 2.1870
Mg II 2803
HE0141-3932
z = 0.3401
Mg II 2796
HE0141-3932
z = 0.3401
Mg II 2803
Δv [km s−1]
Δv [km s−1]
Δv [km s−1]
Δv [km s−1]

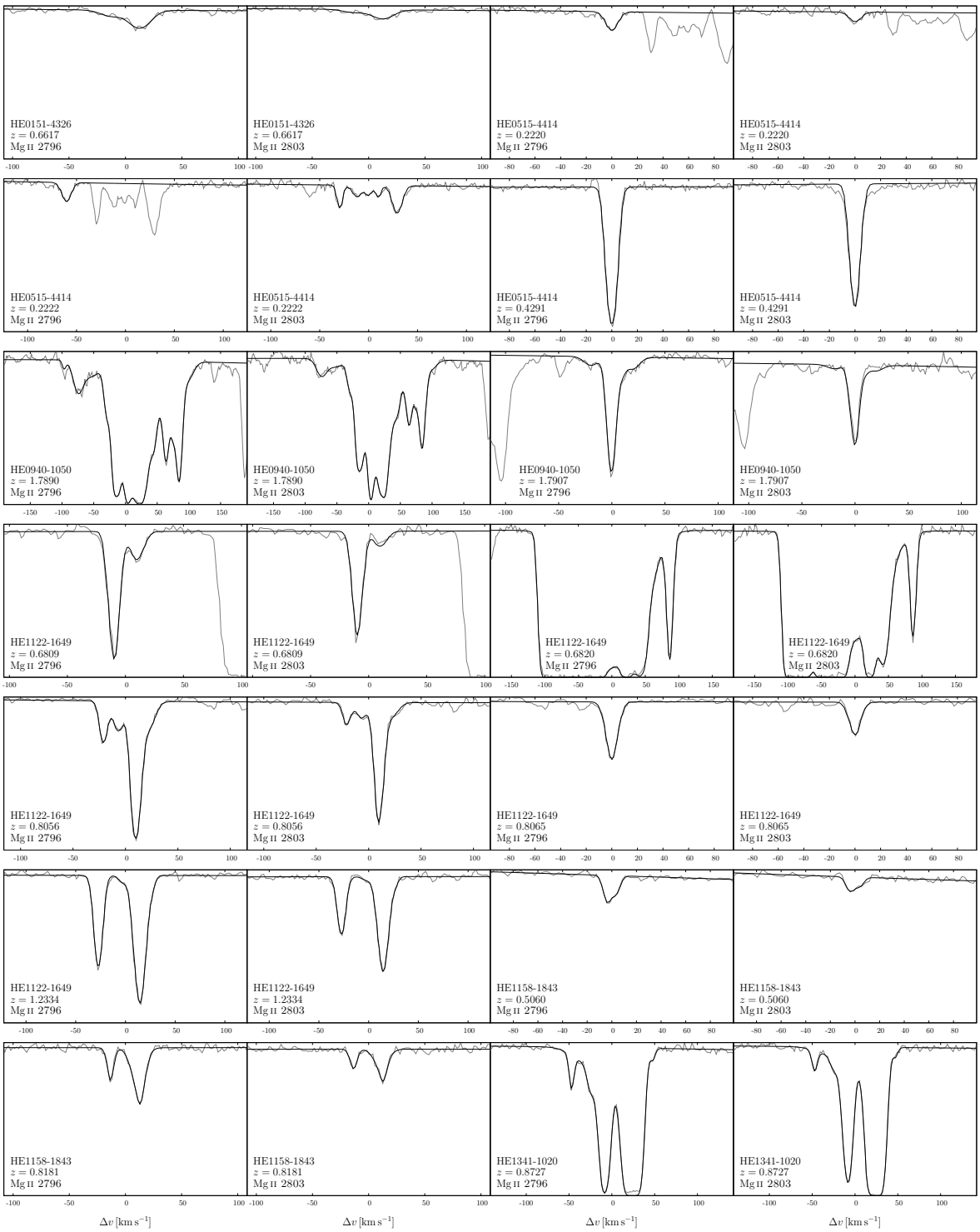
HE0151-4326
z = 0.6617
Mg II 2796
HE0151-4326
z = 0.6617
Mg II 2803
HE0515-4414
z = 0.2220
Mg II 2796
HE0515-4414
z = 0.2220
Mg II 2803
HE0515-4414
z = 0.2222
Mg II 2796
HE0515-4414
z = 0.2222
Mg II 2803
HE0515-4414
z = 0.4291
Mg II 2796
HE0515-4414
z = 0.4291
Mg II 2803
HE0940-1050
z = 1.7890
Mg II 2796
HE0940-1050
z = 1.7890
Mg II 2803
HE0940-1050
z = 1.7907
Mg II 2796
HE0940-1050
z = 1.7907
Mg II 2803
HE1122-1649
z = 0.6809
Mg II 2796
HE1122-1649
z = 0.6809
Mg II 2803
HE1122-1649
z = 0.6820
Mg II 2796
HE1122-1649
z = 0.6820
Mg II 2803
HE1122-1649
z = 0.8056
Mg II 2796
HE1122-1649
z = 0.8056
Mg II 2803
HE1122-1649
z = 0.8065
Mg II 2796
HE1122-1649
z = 0.8065
Mg II 2803
HE1122-1649
z = 1.2334
Mg II 2796
HE1122-1649
z = 1.2334
Mg II 2803
HE1158-1843
z = 0.5060
Mg II 2796
HE1158-1843
z = 0.5060
Mg II 2803
HE1158-1843
z = 0.8181
Mg II 2796
HE1158-1843
z = 0.8181
Mg II 2803
HE1341-1020
z = 0.8727
Mg II 2796
HE1341-1020
z = 0.8727
Mg II 2803
Δv [km s−1]
Δv [km s−1]
Δv [km s−1]
Δv [km s−1]

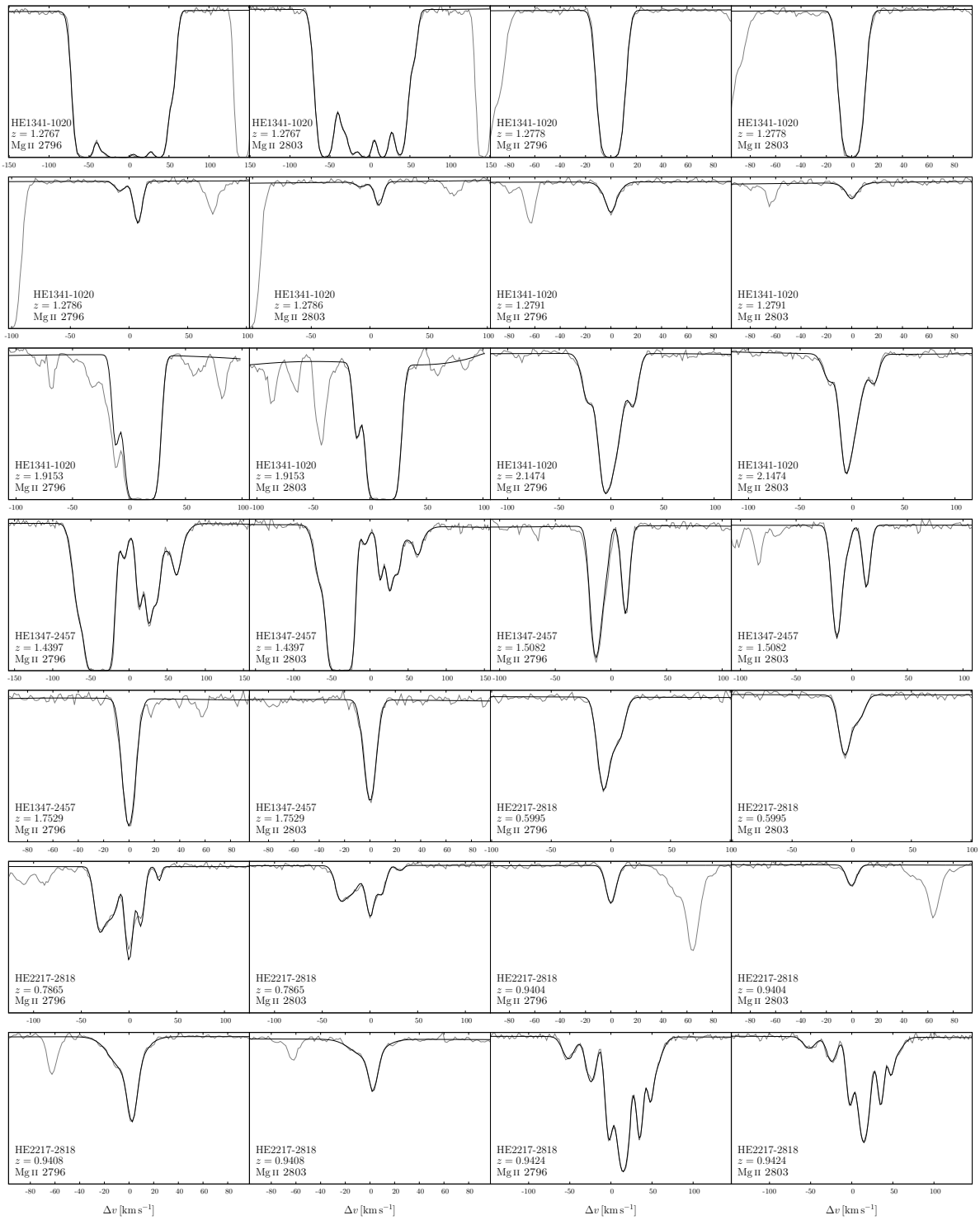
HE1341-1020
z = 1.2767
Mg II 2796
HE1341-1020
z = 1.2767
Mg II 2803
HE1341-1020
z = 1.2778
Mg II 2796
HE1341-1020
z = 1.2778
Mg II 2803
HE1341-1020
z = 1.2786
Mg II 2796
HE1341-1020
z = 1.2786
Mg II 2803
HE1341-1020
z = 1.2791
Mg II 2796
HE1341-1020
z = 1.2791
Mg II 2803
HE1341-1020
z = 1.9153
Mg II 2796
HE1341-1020
z = 1.9153
Mg II 2803
HE1341-1020
z = 2.1474
Mg II 2796
HE1341-1020
z = 2.1474
Mg II 2803
HE1347-2457
z = 1.4397
Mg II 2796
HE1347-2457
z = 1.4397
Mg II 2803
HE1347-2457
z = 1.5082
Mg II 2796
HE1347-2457
z = 1.5082
Mg II 2803
HE1347-2457
z = 1.7529
Mg II 2796
HE1347-2457
z = 1.7529
Mg II 2803
HE2217-2818
z = 0.5995
Mg II 2796
HE2217-2818
z = 0.5995
Mg II 2803
HE2217-2818
z = 0.7865
Mg II 2796
HE2217-2818
z = 0.7865
Mg II 2803
HE2217-2818
z = 0.9404
Mg II 2796
HE2217-2818
z = 0.9404
Mg II 2803
HE2217-2818
z = 0.9408
Mg II 2796
HE2217-2818
z = 0.9408
Mg II 2803
HE2217-2818
z = 0.9424
Mg II 2796
HE2217-2818
z = 0.9424
Mg II 2803
Δv [km s−1]
Δv [km s−1]
Δv [km s−1]
Δv [km s−1]

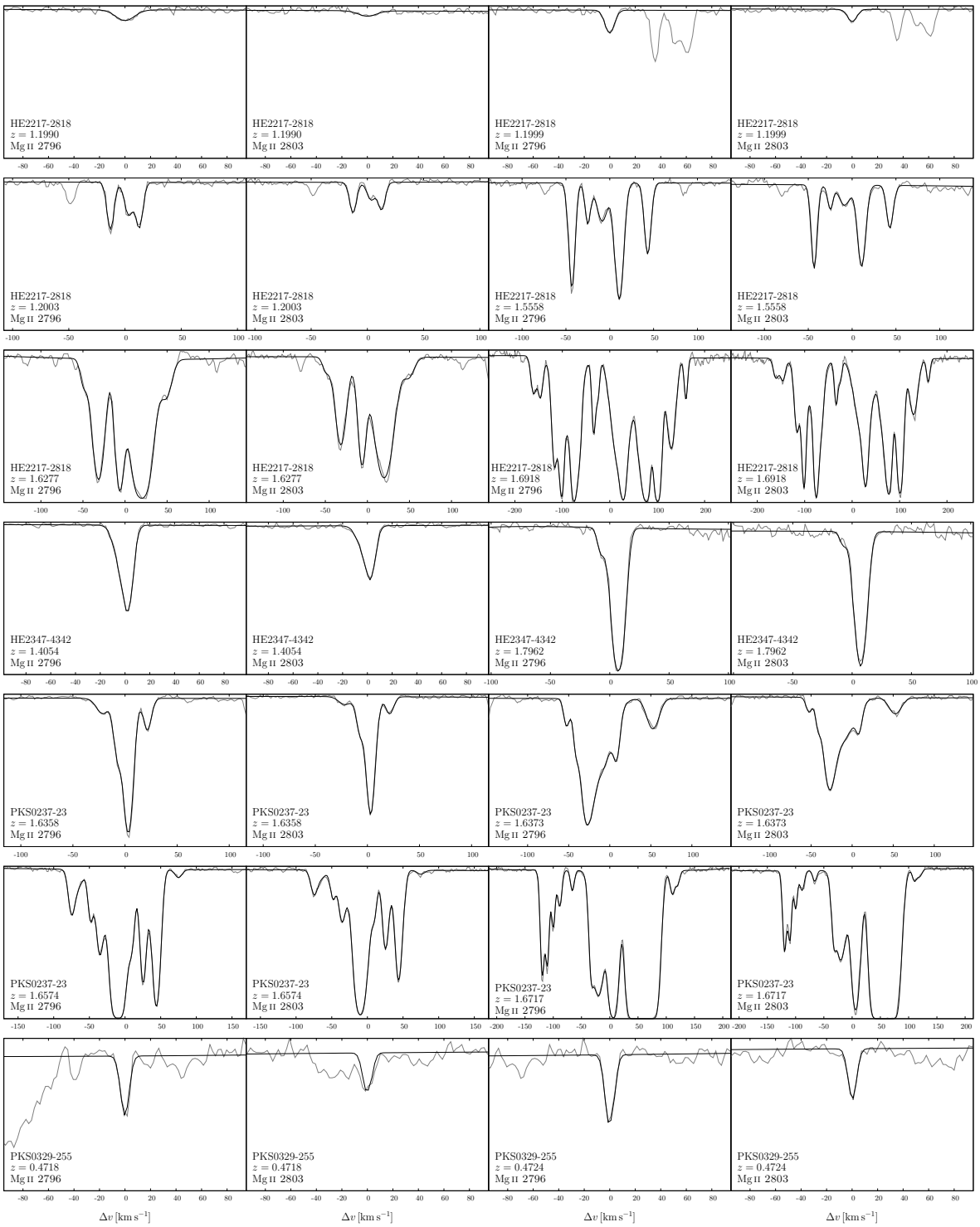
HE2217-2818
z = 1.1990
Mg II 2796
HE2217-2818
z = 1.1990
Mg II 2803
HE2217-2818
z = 1.1999
Mg II 2796
HE2217-2818
z = 1.1999
Mg II 2803
HE2217-2818
z = 1.2003
Mg II 2796
HE2217-2818
z = 1.2003
Mg II 2803
HE2217-2818
z = 1.5558
Mg II 2796
HE2217-2818
z = 1.5558
Mg II 2803
HE2217-2818
z = 1.6277
Mg II 2796
HE2217-2818
z = 1.6277
Mg II 2803
HE2217-2818
z = 1.6918
Mg II 2796
HE2217-2818
z = 1.6918
Mg II 2803
HE2347-4342
z = 1.4054
Mg II 2796
HE2347-4342
z = 1.4054
Mg II 2803
HE2347-4342
z = 1.7962
Mg II 2796
HE2347-4342
z = 1.7962
Mg II 2803
PKS0237-23
z = 1.6358
Mg II 2796
PKS0237-23
z = 1.6358
Mg II 2803
PKS0237-23
z = 1.6373
Mg II 2796
PKS0237-23
z = 1.6373
Mg II 2803
PKS0237-23
z = 1.6574
Mg II 2796
PKS0237-23
z = 1.6574
Mg II 2803
PKS0237-23
z = 1.6717
Mg II 2796
PKS0237-23
z = 1.6717
Mg II 2803
PKS0329-255
z = 0.4718
Mg II 2796
PKS0329-255
z = 0.4718
Mg II 2803
PKS0329-255
z = 0.4724
Mg II 2796
PKS0329-255
z = 0.4724
Mg II 2803
Δv [km s−1]
Δv [km s−1]
Δv [km s−1]
Δv [km s−1]

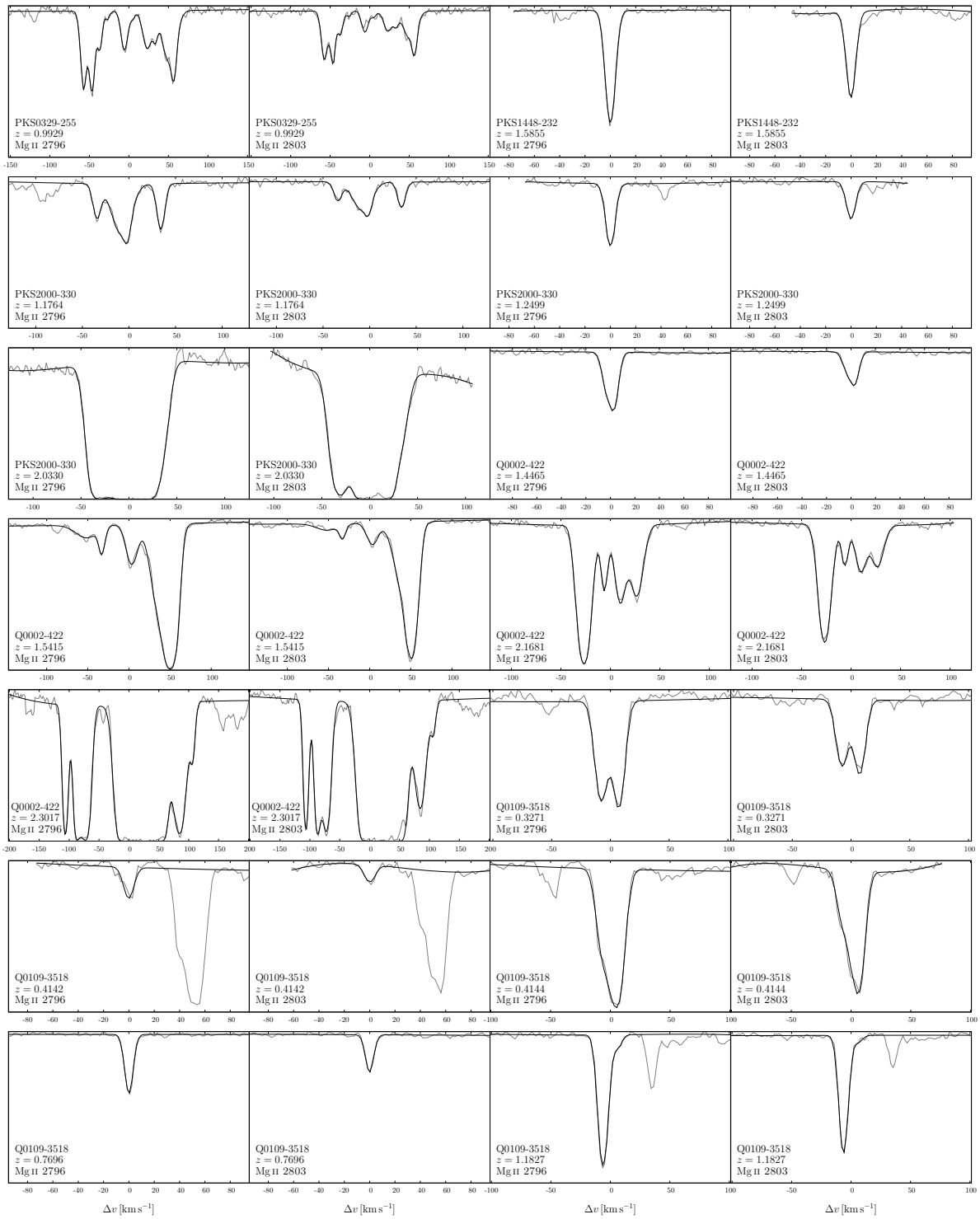
PKS0329-255
$z = 0.9929$
Mg II 2796
PKS0329-255
$z = 0.9929$
Mg II 2803
PKS1448-232
$z = 1.5855$
Mg II 2796
PKS1448-232
$z = 1.5855$
Mg II 2803
PKS2000-330
$z = 1.1764$
Mg II 2796
PKS2000-330
$z = 1.1764$
Mg II 2803
PKS2000-330
$z = 1.2499$
Mg II 2796
PKS2000-330
$z = 1.2499$
Mg II 2803
PKS2000-330
$z = 2.0330$
Mg II 2796
PKS2000-330
$z = 2.0330$
Mg II 2803
Q0002-422
$z = 1.4465$
Mg II 2796
Q0002-422
$z = 1.4465$
Mg II 2803
Q0002-422
$z = 1.5415$
Mg II 2796
Q0002-422
$z = 1.5415$
Mg II 2803
Q0002-422
$z = 2.1681$
Mg II 2796
Q0002-422
$z = 2.1681$
Mg II 2803
Q0002-422
$z = 2.3017$
Mg II 2796
Q0002-422
$z = 2.3017$
Mg II 2803
Q0109-3518
$z = 0.3271$
Mg II 2796
Q0109-3518
$z = 0.3271$
Mg II 2803
Q0109-3518
$z = 0.4142$
Mg II 2796
Q0109-3518
$z = 0.4142$
Mg II 2803
Q0109-3518
$z = 0.4144$
Mg II 2796
Q0109-3518
$z = 0.4144$
Mg II 2803
Q0109-3518
$z = 0.7696$
Mg II 2796
Q0109-3518
$z = 0.7696$
Mg II 2803
Q0109-3518
$z = 1.1827$
Mg II 2796
Q0109-3518
$z = 1.1827$
Mg II 2803
$\Delta v\,[\mathrm{km\,s^{-1}}]$
$\Delta v\,[\mathrm{km\,s^{-1}}]$
$\Delta v\,[\mathrm{km\,s^{-1}}]$
$\Delta v\,[\mathrm{km\,s^{-1}}]$

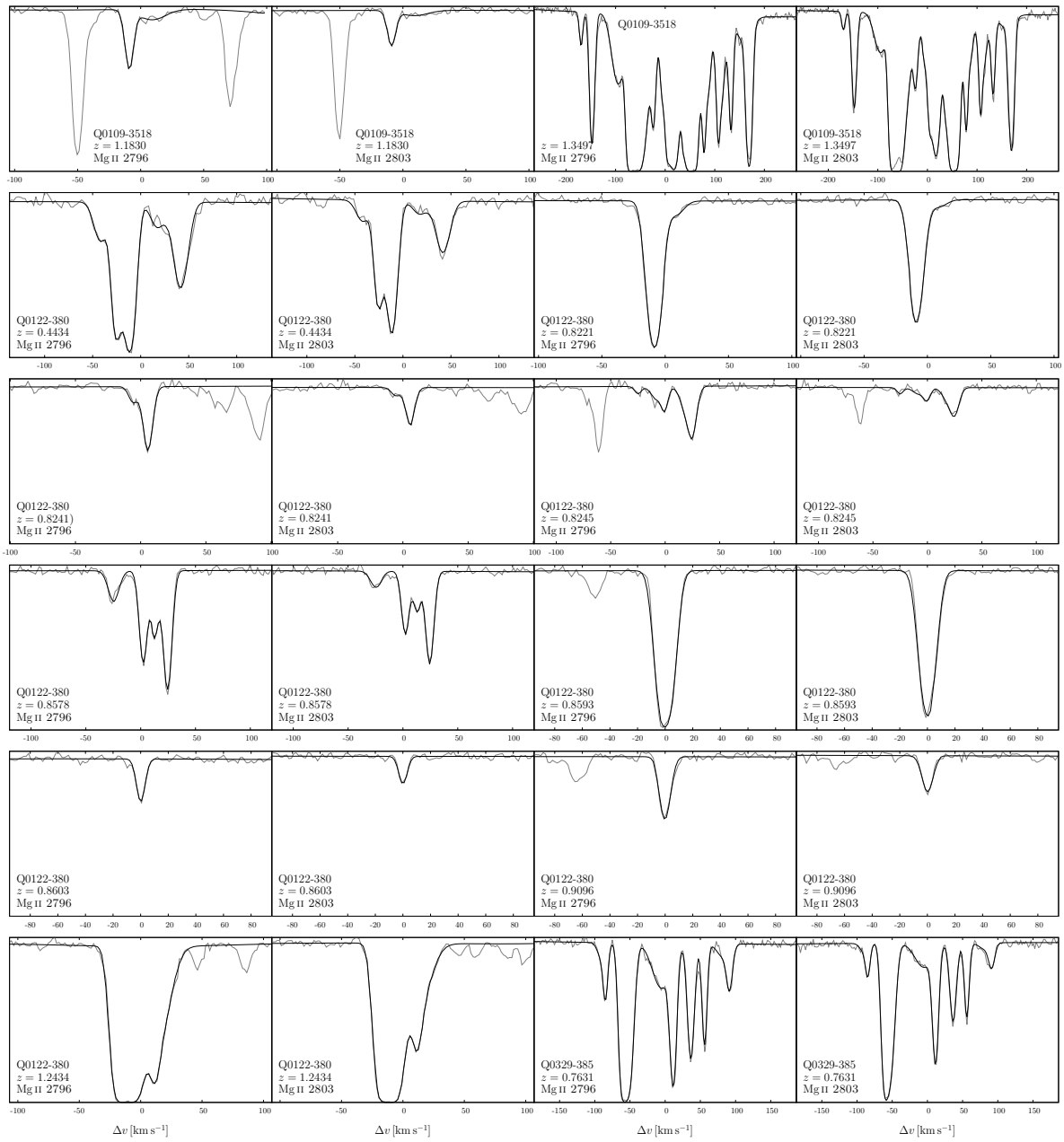
Q0109-3518
z = 1.1830
Mg II 2796
Q0109-3518
z = 1.1830
Mg II 2803
Q0109-3518
z = 1.3497
Mg II 2796
Q0109-3518
z = 1.3497
Mg II 2803
Q0122-380
z = 0.4434
Mg II 2796
Q0122-380
z = 0.4434
Mg II 2803
Q0122-380
z = 0.8221
Mg II 2796
Q0122-380
z = 0.8221
Mg II 2803
Q0122-380
z = 0.8241)
Mg II 2796
Q0122-380
z = 0.8241
Mg II 2803
Q0122-380
z = 0.8245
Mg II 2796
Q0122-380
z = 0.8245
Mg II 2803
Q0122-380
z = 0.8578
Mg II 2796
Q0122-380
z = 0.8578
Mg II 2803
Q0122-380
z = 0.8593
Mg II 2796
Q0122-380
z = 0.8593
Mg II 2803
Q0122-380
z = 0.8603
Mg II 2796
Q0122-380
z = 0.8603
Mg II 2803
Q0122-380
z = 0.9096
Mg II 2796
Q0122-380
z = 0.9096
Mg II 2803
Q0122-380
z = 1.2434
Mg II 2796
Q0122-380
z = 1.2434
Mg II 2803
Q0329-385
z = 0.7631
Mg II 2796
Q0329-385
z = 0.7631
Mg II 2803
Δv [km s−1]
Δv [km s−1]
Δv [km s−1]
Δv [km s−1]

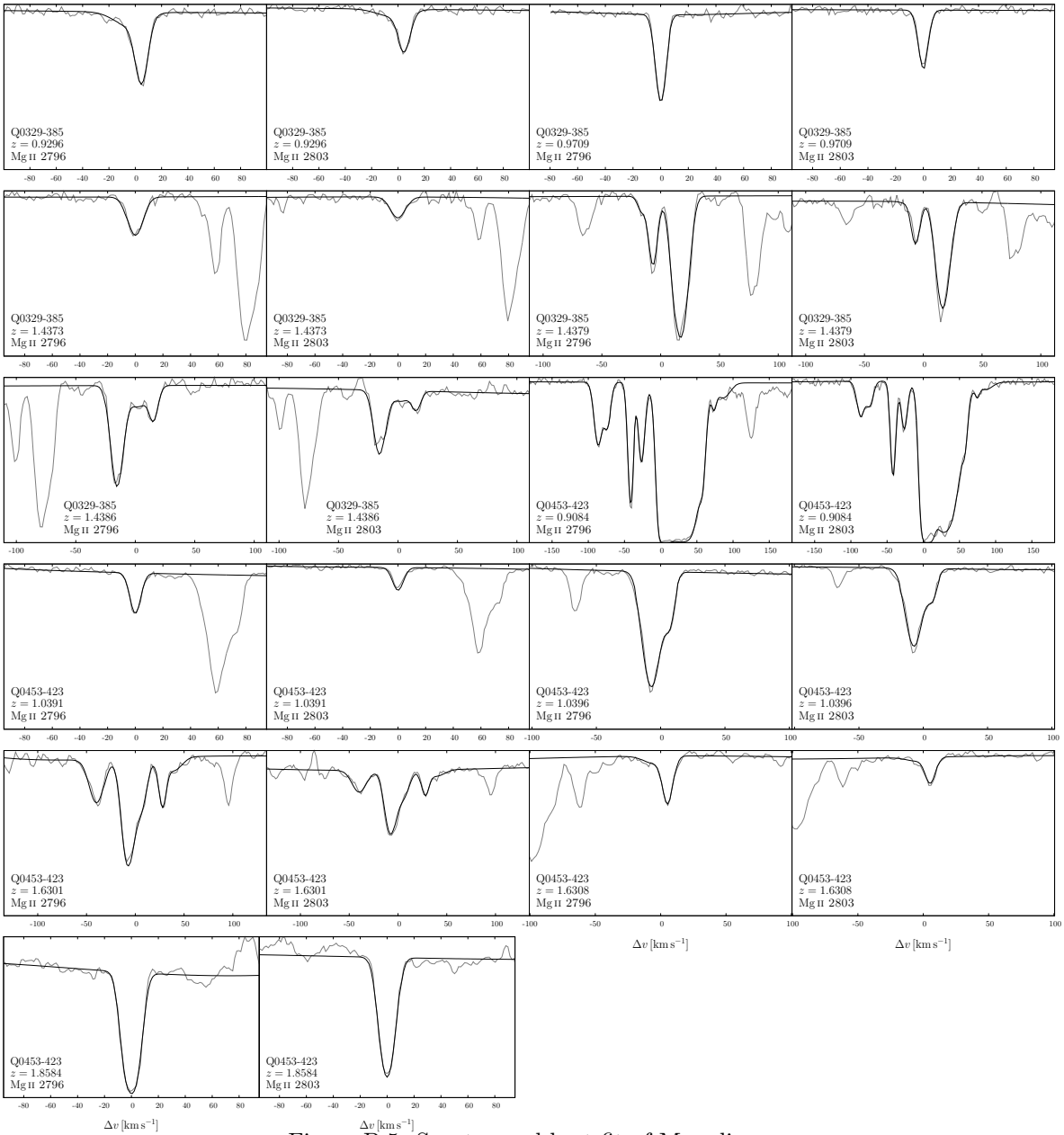

Figure B.5: Spectra and best fit of Mg II lines.

B.4 Cross correlation plots

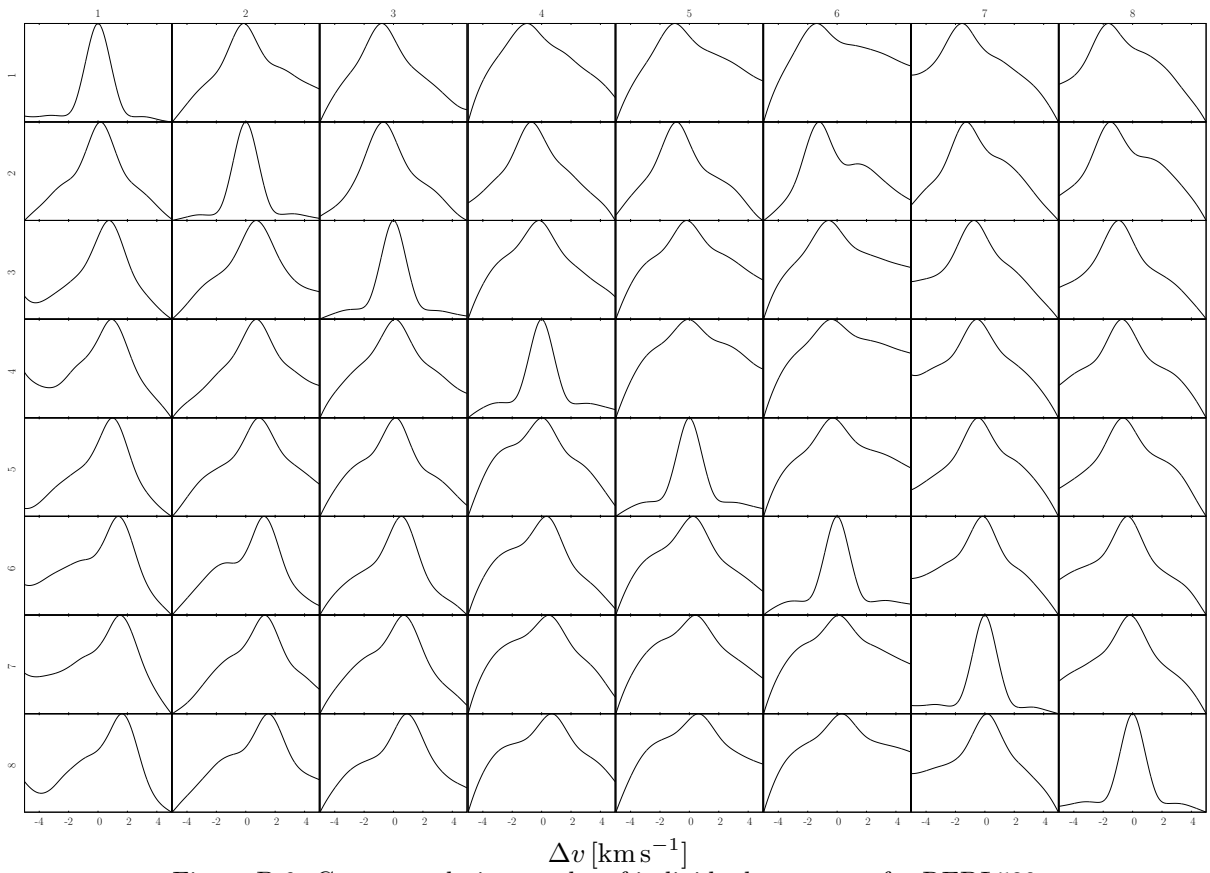

Figure B.6: Cross correlation results of individual exposures for REDL580

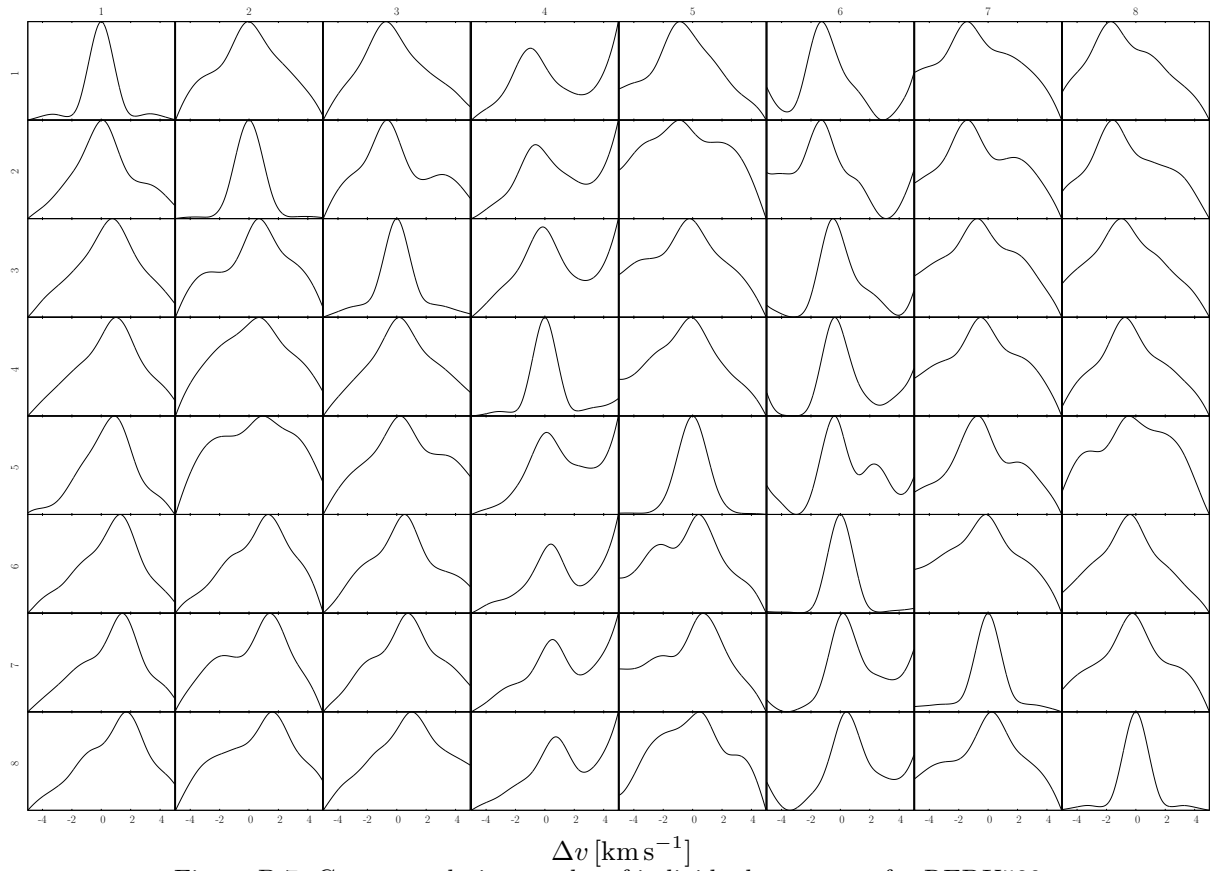

Figure B.7: Cross correlation results of individual exposures for REDU580

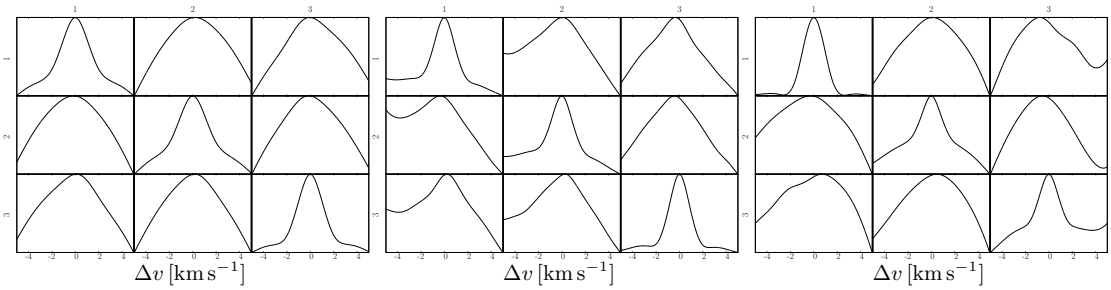

Figure B.8: Cross correlation results of individual exposures for BLUE437, REDL760, and REDU760

Appendix C

Line parameters

C.1 HE0515-4410

Table C.1: Fit parameters of all metal systems in HE0515-4410 at $z = 1.15$

Ion	#	z	N	b[km s^{-1}]
C IV	1	1.1469206 ± 0.0000088	13.16 ± 0.03	20.1 ± 1.2
	4	1.1471649 ± 0.0000025	13.52 ± 0.02	15.6 ± 0.6
		1.1473593 ± 0.0000086	12.20 ± 0.10	6.7 ± 1.6
	8	1.1475721 ± 0.0000009	13.61 ± 0.01	12.6 ± 0.2
	9	1.1478097 ± 0.0000076	12.41 ± 0.07	10.1 ± 1.8
		1.1480238 ± 0.0000012	13.57 ± 0.01	13.0 ± 0.3
		1.1482648 ± 0.0000012	13.66 ± 0.02	9.5 ± 0.2
	15	1.1484753 ± 0.0000132	13.41 ± 0.10	21.2 ± 4.1
	17	1.1487018 ± 0.0000175	12.99 ± 0.21	15.9 ± 4.4
	19	1.1488999 ± 0.0000156	12.62 ± 0.15	12.4 ± 3.0
	21	1.1491185 ± 0.0000037	13.10 ± 0.03	15.7 ± 1.1
		1.1501989 ± 0.0000406	11.35 ± 0.41	5.2 ± 6.2
	28	1.1505383 ± 0.0000234	12.55 ± 0.09	22.5 ± 4.6
	33	1.1508237 ± 0.0000088	13.05 ± 0.06	16.1 ± 1.8
	36	1.1510288 ± 0.0000163	12.79 ± 0.09	15.7 ± 2.6
		1.1513902 ± 0.0000299	12.45 ± 0.10	25.6 ± 5.7
Mg I	1	1.1468847 ± 0.0000784	10.41 ± 0.53	14.9 ± 19.3
	2	1.1469661 ± 0.0000018	10.97 ± 0.08	3.0 ± 0.7
	3	1.1470220 ± 0.0000067	10.28 ± 0.17	0.5 ± 0.9
	4	1.1471367 ± 0.0000068	10.94 ± 0.07	9.4 ± 1.8
	5	1.1472616 ± 0.0000064	10.71 ± 0.09	6.2 ± 1.4
	7	1.1474110 ± 0.0000055	10.60 ± 0.07	6.8 ± 1.6
	8	1.1475918 ± 0.0000062	10.47 ± 0.08	6.2 ± 1.5
	9	1.1478090 ± 0.0000068	10.47 ± 0.08	5.7 ± 1.4
	11	1.1479601 ± 0.0000047	10.68 ± 0.05	6.8 ± 1.0
	13	1.1481300 ± 0.0000062	10.13 ± 0.13	2.0 ± 1.8
	20	1.1490920 ± 0.0000065	11.03 ± 0.11	3.7 ± 1.0
	21	1.1491387 ± 0.0000088	10.67 ± 0.23	2.3 ± 1.6
	23	1.1494975 ± 0.0000063	10.50 ± 0.09	3.6 ± 1.5
	24	1.1495494 ± 0.0000011	11.00 ± 1.60	0.3 ± 0.2
	25	1.1498196 ± 0.0000041	10.43 ± 0.07	2.6 ± 1.2
	26	1.1499055 ± 0.0000098	10.12 ± 0.18	3.7 ± 3.2
	29	1.1505367 ± 0.0000042	10.31 ± 0.10	1.9 ± 1.9
	31	1.1507565 ± 0.0000247	11.54 ± 0.12	15.5 ± 2.7
	32	1.1507888 ± 0.0000006	12.39 ± 0.03	1.9 ± 0.1
	34	1.1508517 ± 0.0000007	11.86 ± 0.03	3.8 ± 0.3
	35	1.1509556 ± 0.0000009	11.79 ± 0.02	6.1 ± 0.3
	37	1.1510646 ± 0.0000016	11.41 ± 0.03	5.7 ± 0.4
	38	1.1512353 ± 0.0000089	11.77 ± 0.06	13.0 ± 1.5
	40	1.1513211 ± 0.0000010	11.73 ± 0.05	6.0 ± 0.3
	41	1.1514504 ± 0.0000061	11.00 ± 0.06	8.8 ± 1.4
Mg II	1	1.1468548 ± 0.0000010	11.81 ± 0.01	7.0 ± 0.1
	2	1.1469732 ± 0.0000001	12.90 ± 0.00	5.0 ± 0.0
	4	1.1471365 ± 0.0000003	12.86 ± 0.00	10.5 ± 0.1
	5	1.1472908 ± 0.0000015	12.17 ± 0.02	6.1 ± 0.2
	6	1.1472471 ± 0.0000005	12.25 ± 0.01	2.4 ± 0.1
	7	1.1474146 ± 0.0000004	12.17 ± 0.01	4.5 ± 0.1
	8	1.1475934 ± 0.0000004	12.29 ± 0.00	7.3 ± 0.1
	9	1.1478100 ± 0.0000004	11.86 ± 0.01	3.0 ± 0.1
	10	1.1479049 ± 0.0000008	11.82 ± 0.01	3.0 ± 0.2
	11	1.1479821 ± 0.0000006	12.14 ± 0.01	5.2 ± 0.2
	13	1.1481001 ± 0.0000010	11.79 ± 0.01	5.7 ± 0.2
	14	1.1483084 ± 0.0000019	11.63 ± 0.02	8.5 ± 0.4
	15	1.1484998 ± 0.0000009	12.07 ± 0.01	7.4 ± 0.2
	16	1.1486239 ± 0.0000030	11.43 ± 0.03	6.4 ± 0.6
	18	1.1487875 ± 0.0000010	11.46 ± 0.02	3.1 ± 0.3
	19	1.1488951 ± 0.0000028	11.09 ± 0.04	4.0 ± 0.7
	21	1.1491086 ± 0.0000002	13.25 ± 0.00	5.8 ± 0.0
	22	1.1491609 ± 0.0000102	11.87 ± 0.06	15.7 ± 1.3
	23	1.1494952 ± 0.0000029	12.26 ± 0.04	5.5 ± 0.3
	24	1.1495545 ± 0.0000031	12.12 ± 0.05	4.9 ± 0.3
	25	1.1498151 ± 0.0000002	12.44 ± 0.00	3.8 ± 0.1
	26	1.1499133 ± 0.0000004	12.18 ± 0.01	4.9 ± 0.1
	27	1.1502491 ± 0.0000055	10.69 ± 0.09	2.1 ± 1.8
	28	1.1504242 ± 0.0000041	11.79 ± 0.03	13.3 ± 0.9
	29	1.1505428 ± 0.0000004	12.11 ± 0.01	2.7 ± 0.1
	31	1.1507237 ± 0.0000020	13.11 ± 0.01	12.3 ± 0.2
	34	1.1508729 ± 0.0000005	18.85 ± 0.07	4.7 ± 0.0
	37	1.1510598 ± 0.0000007	13.24 ± 0.01	10.2 ± 0.2
	39	1.1512739 ± 0.0000004	13.90 ± 0.01	10.6 ± 0.1
	41	1.1514625 ± 0.0000007	12.27 ± 0.02	5.7 ± 0.2
		1.1515368 ± 0.0000097	12.01 ± 0.05	15.1 ± 1.1
	42	1.1517651 ± 0.0000026	11.27 ± 0.03	5.6 ± 0.5
Al II	1	1.1468586 ± 0.0000053	11.15 ± 0.07	6.7 ± 1.5
	2	1.1469722 ± 0.0000008	12.00 ± 0.01	4.7 ± 0.2
	3	1.1471358 ± 0.0000018	12.09 ± 0.01	10.4 ± 0.5
	4	1.1472471 ± 0.0000029	11.48 ± 0.13	2.5 ± 0.8
	6	1.1472931 ± 0.0000159	11.34 ± 0.19	5.8 ± 1.8
	7	1.1474286 ± 0.0000025	11.24 ± 0.04	3.6 ± 0.8
	8	1.1475833 ± 0.0000031	11.57 ± 0.34	0.4 ± 0.2
		1.1476240 ± 0.0000055	11.24 ± 0.06	5.2 ± 0.9
	9	1.1478089 ± 0.0000035	10.89 ± 0.08	2.3 ± 1.3
	10	1.1478994 ± 0.0000069	10.71 ± 0.14	1.3 ± 3.1

Ion	#	z	N	b[km s^{-1}]
Al II	11	1.1479680 ± 0.0000049	11.11 ± 0.08	4.2 ± 1.4
	12	1.1480911 ± 0.0000062	10.87 ± 0.10	5.5 ± 1.5
	14	1.1483109 ± 0.0000102	10.86 ± 0.12	7.2 ± 2.1
	15	1.1484928 ± 0.0000046	11.39 ± 0.05	6.9 ± 1.0
	16	1.1486172 ± 0.0000089	11.19 ± 0.10	8.9 ± 2.5
	18	1.1487805 ± 0.0000080	10.74 ± 0.13	4.0 ± 2.3
	20	1.1490828 ± 0.0000022	11.82 ± 0.09	1.6 ± 0.9
	21	1.1491052 ± 0.0000025	12.07 ± 0.04	5.9 ± 0.3
	23	1.1494938 ± 0.0000149	11.46 ± 0.24	4.7 ± 1.9
	24	1.1495526 ± 0.0000175	11.38 ± 0.28	4.7 ± 1.9
	25	1.1498160 ± 0.0000014	11.74 ± 0.02	3.8 ± 0.4
	26	1.1499132 ± 0.0000023	11.41 ± 0.04	3.2 ± 0.6
	27	1.1505457 ± 0.0000031	11.02 ± 0.07	1.2 ± 1.5
	34	1.1508485 ± 0.0000037	13.03 ± 0.01	19.3 ± 0.5
	35	1.1509653 ± 0.0000013	12.45 ± 0.09	3.0 ± 0.4
	37	1.1510690 ± 0.0000019	12.06 ± 0.05	5.4 ± 0.6
		1.1511405 ± 0.0000026	15.36 ± 4.06	1.0 ± 0.6
	38	1.1512232 ± 0.0000044	12.34 ± 0.06	6.8 ± 1.1
	40	1.1513167 ± 0.0000027	12.60 ± 0.05	6.1 ± 0.5
	41	1.1514169 ± 0.0000337	11.82 ± 0.18	14.6 ± 4.6
Al III	2	1.1469649 ± 0.0000053	11.36 ± 0.11	2.2 ± 2.3
	3	1.1470063 ± 0.0000002	11.44 ± 30.03	0.2 ± 4.6
		1.1470747 ± 0.0000263	11.23 ± 0.38	4.4 ± 6.0
	4	1.1471474 ± 0.0000200	11.29 ± 0.42	3.7 ± 4.6
	5	1.1472390 ± 0.0000166	11.48 ± 0.18	7.8 ± 4.8
	8	1.1475872 ± 0.0000086	11.46 ± 0.07	7.1 ± 1.4
	20	1.1490969 ± 0.0000035	11.85 ± 0.15	4.4 ± 0.9
	21	1.1491110 ± 0.0000246	11.41 ± 0.44	10.1 ± 5.2
	25	1.1498181 ± 0.0000091	11.23 ± 0.12	5.2 ± 2.1
	30	1.1506638 ± 0.0000560	10.88 ± 0.91	4.4 ± 10.1
	32	1.1507986 ± 0.0000079	11.97 ± 0.12	11.5 ± 4.6
	34	1.1508824 ± 0.0000009	12.85 ± 8.35	0.2 ± 0.5
	35	1.1509550 ± 0.0000071	11.56 ± 0.26	3.1 ± 1.8
	36	1.1510007 ± 0.0000545	11.20 ± 0.60	6.7 ± 5.8
	38	1.1512566 ± 0.0000271	11.65 ± 0.07	20.3 ± 1.2
Si II	1	1.1468860 ± 0.0000014	13.41 ± 2.17	0.1 ± 0.1
	2	1.1469700 ± 0.0000024	12.89 ± 0.14	3.5 ± 1.1
	3	1.1470324 ± 0.0000493	12.55 ± 0.37	10.3 ± 7.4
		1.1471033 ± 0.0000019	12.64 ± 0.57	0.2 ± 0.2
	4	1.1471518 ± 0.0000075	12.45 ± 0.22	3.8 ± 2.7
		1.1472624 ± 0.0000097	12.88 ± 0.10	11.0 ± 3.1
	7	1.1474150 ± 0.0000064	12.50 ± 0.10	4.3 ± 1.5
	10	1.1479326 ± 0.0000079	12.48 ± 0.08	8.2 ± 1.9
	13	1.1481094 ± 0.0000077	12.29 ± 0.08	5.4 ± 1.4
	14	1.1483046 ± 0.0000134	12.17 ± 0.14	7.5 ± 2.5
	15	1.1485006 ± 0.0000124	12.52 ± 0.10	12.1 ± 2.9
	17	1.1486655 ± 0.0000415	12.06 ± 0.49	6.3 ± 6.7
	18	1.1487699 ± 0.0000481	12.07 ± 0.46	7.0 ± 8.8
	20	1.1489355 ± 0.0000241	11.95 ± 0.24	8.6 ± 5.0
	21	1.1490998 ± 0.0000032	13.28 ± 0.12	5.0 ± 0.5
	22	1.1491521 ± 0.0000611	12.55 ± 0.65	7.6 ± 5.3
	24	1.1495185 ± 0.0000064	12.79 ± 0.06	8.5 ± 1.4
		1.1495886 ± 0.0000217	11.57 ± 0.72	1.8 ± 6.6
	25	1.1498156 ± 0.0000026	12.63 ± 0.04	3.0 ± 0.8
	26	1.1499122 ± 0.0000057	12.55 ± 0.07	6.5 ± 1.3
	28	1.1505466 ± 0.0000022	12.56 ± 0.05	2.7 ± 0.8
	30	1.1506917 ± 0.0000046	13.27 ± 0.04	8.9 ± 0.8
	33	1.1508209 ± 0.0000022	14.45 ± 0.02	6.3 ± 0.3
	35	1.1509502 ± 0.0000024	13.94 ± 0.02	6.7 ± 0.7
	37	1.1510664 ± 0.0000029	13.36 ± 0.05	6.0 ± 0.7
	38	1.1512430 ± 0.0000101	13.91 ± 0.06	13.7 ± 1.5

Ion	#	z	N	b[km s^{-1}]
Si II	40	1.1513231 ± 0.0000021	13.60 ± 0.09	5.7 ± 0.7
	41	1.1514579 ± 0.0000203	12.81 ± 0.19	11.1 ± 3.0
Cr II	25	1.1507897 ± 0.0000221	11.51 ± 3.09	0.2 ± 6.6
	34	1.1508626 ± 0.0000333	12.24 ± 0.13	22.5 ± 6.3
	35	1.1509655 ± 0.0000077	11.51 ± 0.22	1.1 ± 4.6
	37	1.1510911 ± 0.0000100	11.47 ± 0.24	2.5 ± 2.9
	40	1.1513221 ± 0.0000066	12.10 ± 0.07	7.7 ± 1.5
Mn II	25	1.1507833 ± 0.0000029	11.25 ± 0.14	1.6 ± 1.6
	33	1.1508306 ± 0.0000112	11.61 ± 0.09	9.2 ± 1.6
	35	1.1509600 ± 0.0000042	11.28 ± 0.08	4.1 ± 1.0
		1.1511677 ± 0.0000724	11.28 ± 0.21	21.9 ± 8.7
	40	1.1513153 ± 0.0000073	11.41 ± 0.13	7.7 ± 1.8
Ni II	25	1.1507923 ± 0.0000027	12.31 ± 0.07	1.3 ± 1.7
	34	1.1508844 ± 0.0001579	12.65 ± 1.34	26.3 ± 15.4
	36	1.1509210 ± 0.0000896	12.48 ± 1.91	18.9 ± 18.7
	38	1.1512370 ± 0.0000102	12.21 ± 0.17	5.2 ± 2.9
	40	1.1513403 ± 0.0000069	12.41 ± 0.10	6.1 ± 2.5
Fe I	32	1.1507895 ± 0.0000018	11.49 ± 0.16	0.2 ± 0.1
	34	1.1508557 ± 0.0000112	10.62 ± 0.22	2.6 ± 4.9
Fe II	1	1.1468933 ± 0.0000841	11.06 ± 0.45	11.9 ± 10.3
	2	1.1469678 ± 0.0000014	12.40 ± 0.03	2.4 ± 0.3
	3	1.1470196 ± 0.0000080	11.62 ± 0.15	2.8 ± 1.8
	4	1.1471398 ± 0.0000020	12.17 ± 0.02	9.1 ± 0.7
	5	1.1472449 ± 0.0000020	11.69 ± 0.07	1.4 ± 0.5
	6	1.1472901 ± 0.0000095	11.45 ± 0.13	4.7 ± 1.6
	7	1.1474162 ± 0.0000011	11.90 ± 0.02	2.7 ± 0.3
	8	1.1475807 ± 0.0000016	11.16 ± 0.15	0.4 ± 0.2
	9	1.1478093 ± 0.0000008	11.91 ± 0.02	1.4 ± 0.3
	10	1.1479097 ± 0.0000017	11.79 ± 0.03	2.1 ± 0.7
	11	1.1479769 ± 0.0000010	12.10 ± 0.02	2.9 ± 0.3
	12	1.1480780 ± 0.0000152	11.43 ± 0.23	4.7 ± 3.0
	13	1.1481135 ± 0.0000022	11.53 ± 0.15	0.8 ± 1.1
	15	1.1484958 ± 0.0000036	11.45 ± 0.06	5.9 ± 1.3
	20	1.1490856 ± 0.0000007	12.60 ± 0.03	1.7 ± 0.2
	21	1.1491151 ± 0.0000030	12.45 ± 0.04	4.8 ± 0.3
	23	1.1494888 ± 0.0000046	12.05 ± 0.09	3.8 ± 0.6
	24	1.1495434 ± 0.0000047	12.18 ± 0.07	4.8 ± 0.6
	25	1.1498155 ± 0.0000009	12.04 ± 0.01	2.9 ± 0.3
	26	1.1499143 ± 0.0000014	11.99 ± 0.02	4.3 ± 0.3
	28	1.1504207 ± 0.0000069	11.46 ± 0.08	7.6 ± 1.9
	29	1.1505485 ± 0.0000021	11.62 ± 0.04	3.0 ± 0.8
	30	1.1506849 ± 0.0000006	12.50 ± 0.02	2.0 ± 0.2
	31	1.1507424 ± 0.0000038	11.68 ± 0.12	1.1 ± 0.6
	32	1.1507933 ± 0.0000004	13.43 ± 0.01	2.8 ± 0.1
	33	1.1508344 ± 0.0000027	13.50 ± 0.01	15.7 ± 0.4
	34	1.1508605 ± 0.0000006	13.03 ± 0.02	1.5 ± 0.0
	35	1.1509617 ± 0.0000002	13.47 ± 0.01	3.7 ± 0.1
	37	1.1510669 ± 0.0000005	13.11 ± 0.01	6.2 ± 0.1
	38	1.1512278 ± 0.0000020	13.47 ± 0.01	11.2 ± 0.3
	40	1.1513211 ± 0.0000005	13.50 ± 0.01	5.6 ± 0.1
	41	1.1514308 ± 0.0000037	12.58 ± 0.03	10.8 ± 0.8
		1.1516067 ± 0.0000101	11.58 ± 0.09	8.9 ± 2.3
	42	1.1517615 ± 0.0000069	11.25 ± 0.10	4.9 ± 1.9
Zn II	25	1.1507896 ± 0.0000014	11.82 ± 0.02	2.4 ± 0.5
	34	1.1508586 ± 0.0000024	11.51 ± 0.04	1.7 ± 1.1
	35	1.1509471 ± 0.0000071	10.80 ± 0.16	0.8 ± 1.8
	38	1.1511958 ± 0.0000243	11.76 ± 0.07	32.0 ± 6.2

C.2 2004 large program data

Table C.2: Fit parameters of Fe II systems in the 2004 Large Program data. The redshift represents Fe II 1608.

#	z	N	b[km s^{-1}]
		HE0001-2340	
1	1.5864418	12.59 ± 0.01	1.8 ± 0.0
1	2.1852978	12.33 ± 0.01	2.4 ± 0.2
1	2.1871543	12.95 ± 0.01	3.4 ± 0.1
2	2.1872861	11.70 ± 0.09	0.4 ± 0.1
		HE1341-1020	
1	1.9153435	12.30 ± 0.01	2.2 ± 0.2
2	1.9154818	12.89 ± 0.00	6.2 ± 0.1
		HE1347-2457	
1	1.4391987	13.73 ± 0.01	9.1 ± 0.1
2	1.4392459	14.05 ± 0.01	5.0 ± 0.1
3	1.4393429	14.84 ± 0.07	1.9 ± 0.0
		HE2217-2818	
1	1.6908445	12.09 ± 0.01	5.2 ± 0.3
2	1.6909757	12.77 ± 0.01	3.1 ± 0.1
3	1.6910873	11.59 ± 0.03	1.3 ± 0.5
4	1.6912037	12.66 ± 0.07	4.6 ± 0.4
5	1.6912731	12.19 ± 0.21	6.7 ± 1.6
1	1.6920753	12.02 ± 0.28	8.0 ± 2.3
2	1.6921454	12.11 ± 0.06	1.2 ± 0.2
3	1.6921869	12.14 ± 0.24	7.7 ± 2.3
4	1.6925954	12.29 ± 0.05	5.4 ± 0.5
5	1.6925694	12.46 ± 0.03	15.7 ± 1.2
6	1.6928112	12.68 ± 0.01	4.0 ± 0.1
7	1.6930485	11.78 ± 0.03	9.0 ± 0.7
		PKS0237-23	
1	1.6358132	11.46 ± 0.03	1.1 ± 0.3
2	1.6359004	12.25 ± 0.01	2.4 ± 0.2
1	1.6369228	11.33 ± 0.03	1.3 ± 0.4
2	1.6370247	11.63 ± 0.03	1.5 ± 0.3
3	1.6371472	12.61 ± 0.03	6.6 ± 0.2
4	1.6372529	12.45 ± 0.04	15.2 ± 1.1
5	1.6374670	11.60 ± 0.04	4.6 ± 0.6
1	1.6716637	12.13 ± 0.02	2.2 ± 0.3
2	1.6717792	12.44 ± 0.02	11.6 ± 0.5
3	1.6720084	12.53 ± 0.01	5.9 ± 0.2
1	1.6723380	14.40 ± 0.01	4.6 ± 0.1
2	1.6724295	13.78 ± 0.03	3.2 ± 0.3
3	1.6724018	13.51 ± 0.04	14.5 ± 1.0
4	1.6725813	13.86 ± 0.01	4.7 ± 0.1
5	1.6726957	12.33 ± 0.04	4.5 ± 0.5
		PKS0237-23	
1	1.6723380	14.40 ± 0.01	4.6 ± 0.1
2	1.6724295	13.78 ± 0.03	3.2 ± 0.3
3	1.6724018	13.51 ± 0.04	14.5 ± 1.0
4	1.6725813	13.86 ± 0.01	4.7 ± 0.1
5	1.6726957	12.33 ± 0.04	4.5 ± 0.5
		PKS2126-158	
1	1.6716637	12.13 ± 0.02	2.2 ± 0.3
2	1.6717792	12.44 ± 0.02	11.6 ± 0.5
3	1.6720084	12.53 ± 0.01	5.9 ± 0.2
4	1.6723380	14.40 ± 0.01	4.6 ± 0.1
5	1.6724295	13.78 ± 0.03	3.2 ± 0.3
6	1.6724018	13.51 ± 0.04	14.5 ± 1.0
7	1.6725813	13.86 ± 0.01	4.7 ± 0.1
8	1.6726957	12.33 ± 0.04	4.5 ± 0.5
		Q0002-422	
1	2.1677868	12.12 ± 0.23	2.4 ± 1.5
2	2.1678544	12.63 ± 0.07	3.1 ± 0.6
1	2.3006189	12.46 ± 0.05	1.4 ± 0.2
2	2.3008534	12.09 ± 0.05	3.3 ± 1.1
3	2.3010160	12.43 ± 0.03	3.3 ± 0.6
4	2.3015203	11.96 ± 0.12	1.0 ± 0.0
5	2.3016927	13.75 ± 0.01	5.7 ± 0.1
6	2.3019042	13.67 ± 0.01	4.1 ± 0.2
7	2.3020496	13.46 ± 0.03	29.5 ± 1.6
8	2.3021211	12.46 ± 0.14	0.7 ± 0.2
9	2.3022755	12.81 ± 0.04	2.6 ± 0.4
10	2.3024626	12.36 ± 0.07	1.5 ± 0.5
11	2.3026093	11.34 ± 0.49	0.2 ± 0.3
12	2.3027347	11.96 ± 0.15	3.1 ± 3.1
13	2.3029102	12.09 ± 0.13	10.0 ± 3.6

Acknowledgements

Part of this work has been supported by the DFG Sonderforschungsbereich 676 Teilprojekt C4.

I wish to thank Prof. Dr. Dieter Reimers for his support.

Furthermore I would like to thank Dr. Robert Baade for his helpful comments.

Eidesstattliche Versicherung
Declaration on oath

Hiermit erkläre ich an Eides statt, dass ich die vorliegende Dissertation selbst verfasst und keine anderen als die angegebenen Quellen und Hilfsmittel benutzt habe.
I hereby declare, on oath, that I have written the present dissertation by my own and have not used other than the acknowledged resources and aids.

Hamburg, den 28.04.2014

Nils Prause